

Abstract

Going to make LIGO the best possible ever.

Adaptive Mode Matching in Advanced LIGO

Thomas Vo

Spring 2017

Preface

The era of gravitational waves astronomy was ushered in by the LIGO (Laser Interferometer Gravitational-Wave Observatory) collaboration with the detection of a binary black hole collision (Detection paper). The event that shook the foundation of space-time allowed mankind to view the cosmos in a way that had never been done previously.

Contents

Preface	1
1 Introduction	5
1.1 Gravitational Waves	5
1.2 Measuring Gravitational Waves with Light	7
1.3 Detection of Gravitational Waves	11
2 The LIGO Instrument	14
2.0.1 Simple Michelson	14
2.0.2 Fabry-Perot Cavities	18
2.0.3 Fabry-Perot Michelson	23
2.0.4 Power-Recycled Fabry-Perot Interferometers	26
2.0.5 Dual-Recycled Fabry-Perot Interferometers	27
2.0.6 Fundamental Noise Sources	30
2.1 Mode Matching with Squeezed States of Light	38
3 The Fundamentals of Mode-Matching	42
3.1 Gaussian Beam Optics	42
3.1.1 Misalignment and Higher Order Modes	48
3.1.2 Mode Mismatch and Higher Order Modes	50
3.2 Wavefront Sensing	51
4 Simulating Mode-Matching with Finesse	54
4.1 How it works	54
4.2 Finesse Simulations	55
4.2.1 ALIGO Design with FC and Squeezer	55

4.2.2	Looking at just Modal Change	55
4.2.3	QM Limited Sensitivity	55
4.3	Results	55
5	Experimental Mode Matching Cavities at Syracuse	56
5.1	Adaptive Mode Matching	56
5.2	Actuators	56
5.2.1	Thermal Lenses	56
5.2.2	Translation Stages	57
5.3	Sensors	57
5.3.1	Bullseye Photodiodes (BPD)	57
5.3.2	Mode Converters	58
5.3.3	DC Mode Matching	61
6	Mode Matching Cavities at LIGO Hanford	62
6.1	Mode Matching IFO to OMC: Single Bounce vs DRMI	62
6.1.1	SR3 Heater	62
6.1.2	SRM Heater	62
6.2	Mode Matching Squeezer to OMC	62
6.3	Mode Matching as a Function of DARM Offset	63
6.4	Modal Contrast Defect	63
6.4.1	Simple Michelson Contrast Defect	64
6.5	Hot vs. Cold Interferometers	64
6.5.1	Thermal Lensing	65
6.6	Wavefront Distortions from Thermal Effects	66
6.7	Tuning Thermal Compensation for LIGO	70
6.7.1	Hartmann Wavefront Sensors	71
6.7.2	Ring Heater Commissioning	72
6.7.3	CO2 Commissioning	72
6.7.4	SR3 Thermal Actuator	73
6.7.5	Putting it all together	73
7	Solutions for Detector Upgrades	79
7.1	Sensors	79

CONTENTS	4
7.2 High Sensitivity Telescope	79
7.3 A Global Active Wavefront Control Scheme	79
7.3.1 Hard and Soft Mode Matching	80
Appendices	81
A Resonator Formulas	82
B Hermite Gauss Normalization	85
C Bullseye and Quadrant Photodiode Characterization	87
C.1 Quadrant Photodiodes (QPD)	87
C.2 Bullseye Photodiodes	88
C.2.1 Width	88
C.2.2 Pitch	89
C.2.3 Yaw	90
C.2.4 RF	90
D Overlap of Gaussian Beams	91

Chapter 1

Introduction

When gravitational waves were first detected in September 2015, the first question was, "Is it real?". The next was, "How do we get more?".

The Laser Interferometer Gravitational-Wave Observatory (LIGO), was built with the purpose of detecting the ripples in space-time caused by astrophysical events to understand the complexities hidden in the cosmos. In 2011, the advanced version of the LIGO detectors were installed and commissioned which detected the first signals from colliding black holes [2]. During the writing of this thesis, the detectors had hardware replaced in order to mitigate noise from scattered light and new optics which reduced the losses from absorption.

The first chapter of this thesis serves as an introduction to gravitational waves and their affect on a simple interferometer. The second chapter will describe the modern detectors and their dominating noise sources. Chapters 3-6 will be focused on experimental wavefront control for the current generation of detectors and beyond.

1.1 Gravitational Waves

In 1915, Albert Einstein published his theory of general relativity [28], which contains the most complete description of gravity to date. This theory has stood the test of time and scrutiny by correctly predicting the perihelion of mercury [26], the bending of light from massive objects [4], and the loss of energy from gravitational radiation [74]. The seminal equation in this theory, called the Einstein Field Equation is

$$G_{\mu\nu} = 8\pi T_{\mu\nu} \quad (1.1)$$

which is a set of 10 coupled second-order differential equations that are nonlinear and fully describes the interaction between space-time and mass-energy. Equation 1.1 is difficult to solve except in situations where specific approximations allow a user to find exact solutions such as spherical symmetry [14] [67]. In areas where the curvature is close to flat, the weak field approximation can be applied and the metric is described as

$$g_{\mu\nu} \approx \eta_{\mu\nu} + h_{\mu\nu} \quad (1.2)$$

where $\eta_{\mu\nu}$ is the metric of flat spacetime and $|h_{\mu\nu}| \ll 1$ is the perturbation due to a gravitational field. By plugging in equation 1.2 into 1.1 and using empty space we obtain the familiar wave equation

$$\left(\nabla^2 - \frac{1}{c^2} \frac{\partial^2}{\partial t^2} \right) h_{\mu\nu} = 0 \quad (1.3)$$

which has a plane-wave solution of the form $h_{\mu\nu} = A_{\mu\nu} e^{ik_\nu x^\nu}$. Using the gauge constraint $h_{,\nu}^{\mu\nu} = 0$, it follows that $A_{\mu\nu} k^\mu = 0$ which means that the gravitational wave amplitude is orthogonal to the propagation vector. Further imposing transverse-traceless gauge and assuming that the wave is traveling in the x^3 direction, it can be shown that the complex amplitude has physical significance expressed in the matrix

$$A_{\mu\nu} = \begin{pmatrix} 0 & 0 & 0 & 0 \\ 0 & A_{xx} & A_{yx} & 0 \\ 0 & A_{xy} & -A_{xx} & 0 \\ 0 & 0 & 0 & 0 \end{pmatrix} \quad (1.4)$$

Oftentimes, the four non-zero components of equation 1.4 can be categorized into two distinct polarizations: plus and cross where $h_+ = A_{xx} = -A_{yy}$ and $h_\times = A_{xy} = A_{yx}$.

Consider the four-velocity, U^α , in the transverse traceless gauge where the coordinate itself is attached the particles and incorporates any small wiggles that would shake the coordinates. Of course, any free particles will follow the geodesic equation

$$\nabla U^\alpha = \frac{d}{d\tau} U^\alpha + \Gamma_{\mu\nu}^\alpha U^\mu U^\nu = 0 \quad (1.5)$$

where $\Gamma_{\mu\nu}^\alpha = \frac{1}{2} g^{\gamma\alpha} (g_{\gamma\mu,\nu} + g_{\gamma\nu,\mu} - g_{\mu\nu,\gamma})$ are the famous Christoffel symbols. By evaluating the first term of the acceleration in equation 1.5,

$$\left(\frac{dU^\alpha}{d\tau} \right)_0 = -\Gamma_{00}^\alpha = \frac{1}{2} \eta_{\mu\nu} (h_{\beta 0,0} + h_{0\beta,0} + h_{00,\beta}) \quad (1.6)$$

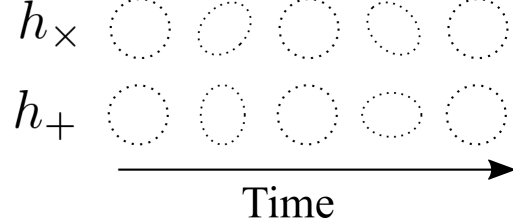


Figure 1.1: **Effects of a gravitational wave.** A ring of free floating particles will be stretched and squeezed by a passing gravitational wave, the two pictures represent the plus and cross polarizations.

However, comparing equation 1.4 and equation 1.6, it is clear that if the particle is initially at rest, then a moment later it is still at rest! The term "at rest" is actually used liberally here since the coordinate system varies along with the gravitational wave. To understand the physical interpretation of equation 1.4, imagine the gravitational wave propagating towards a ring of free floating particles in space. The spacetime will be modulated in a squeezed and stretched motion as shown in Figure 1.1.

Alternatively, one can ask if a gravitational wave passed by a pair of particles separated by length L , what would be the effect on the distance between two points [66]? The proper distance is defined as

$$\delta l = \int g_{\mu\nu} dx^\mu dx^\nu = \int_0^L g_{xx} dx \approx |g_{xx}(x=0)|^{1/2} \approx [1 + \frac{1}{2}h_{xx}(x=0)]L \quad (1.7)$$

which shows us two very important points about the nature of gravitational waves. Firstly, the effect is very small since the length variation, h_{xx} , is a small perturbation on flat space-time. Secondly, the effect is proportional to the initial separation between the particles. This means a detector which is large will have a better chance to measure these small effects, an important point that drove the design of the Laser Interferometer Gravitational-Wave Interferometer (LIGO).

1.2 Measuring Gravitational Waves with Light

Even with the theoretical formulation of gravitational waves resolved by the 1970s [60], developing a method of detecting gravitational waves with ground-based instruments was still a controversial topic among scientists in the field [23]. During the famous Chapel Hill Conference in 1957, which included some of the great minds of the era such as Wheeler, Schwinger, and Feynman, the experimental search for gravitational waves began to take hold. One thought experiment that was proposed by Feynmann [18] where he considered a bead sliding on a string with friction as a gravitational wave passes by. As the bead slides back and forth due to the wave described by equation 1.7, there will be some heat dissipated which means the gravitational wave must carry some energy.

There is still the issue of an incredible amount of accuracy required to measure the strain from even the

most dense astrophysical objects. The earliest attempts at detecting these small signals were famously done by Joseph Weber [73] using large resonant bars and piezoelectric transducers to extract the energy from gravitational waves at the resonant frequencies of the bars. However, these bars are limited by thermal noise and could only detect GWs in very narrow frequency bands.

With the development of lasers in the 1960s which created coherent and spatially confined light that could propagate long distances. As light travels in space, it picks up an important quality called *phase* as a function of distance. Interferometers are devices that measure small displacements by using a laser that is split by a partially transmitting mirror, which allows 50% of the light to get reflected and 50% to be transmitted. Each of the beams travel down the arms and reflect off of mirrors and return to the beamsplitter. Upon reaching the optic, the two beams recombine and by the principle of superposition the electromagnetic waves will add linearly at the output port (or antisymmetric port), Figure 1.2. The laser beams will gather phase as they propagate down each individual arm, and when recombining, the intensity of the light will be proportional to the phase differences between each beam. This will correspond to a differential length that is described by

$$L_- = l_x - l_y \quad (1.8)$$

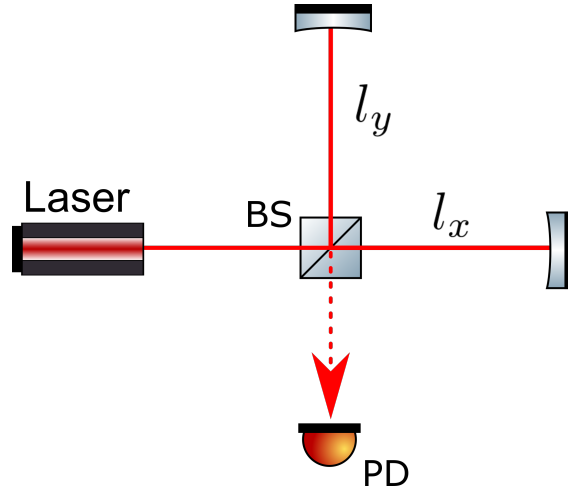


Figure 1.2: **A Michelson Interferometer.** A laser is split between with a partially transmitting optic called a beamsplitter (BS), then propagate down each arm to reflect off mirrors, sometimes called test masses (TM). The beams return to the beamsplitter and recombine, photodetectors are placed at the antisymmetric port (AS).

As shown in equation 1.7, the effect of gravitational waves on the proper length between two free falling objects is proportional to the initial separation. From Figure 1.1, it is intuitively clear that interferometry would be an ideal technique to detect signals from a gravitational wave. However, one can explicitly derive an interferometer's response to a GW from an astrophysical object.

First, denote the detector's coordinates using \hat{x} and \hat{y} to co-align with the interferometer arms respectively such that the \hat{z} axis points directly towards the zenith. Now consider a gravitational wave source arbitrarily located in the sky with respect to the Earth with the axis of propagation pointed in the \hat{z}' direction. Using the well known Euler angles, a relation from the detector frame to the source frame with coordinates $\{\hat{x}', \hat{y}', \hat{z}'\}$ can be seen in Figure 1.3.

If a gravitational wave at the source has emitted GWs with plus and cross polarizations as denoted by equation 1.4, then the detector time series can be regarded as [1] [32]

$$h(t) = F_+(\theta, \phi, \psi) h_+(t) + F_\times(\theta, \phi, \psi) h_\times(t) \quad (1.9)$$

where $F_+(\theta, \phi, \psi)$ and $F_\times(\theta, \phi, \psi)$ are the antenna pattern functions that project the gravitational wave amplitudes onto the detector frame shown in Figure.

$$F_+(\theta, \phi, \psi) = -\frac{1}{2}[1 + \cos^2(\theta)]\cos(2\phi)\cos(2\psi) - \cos(\theta)\sin(2\phi)\sin(2\psi) \quad (1.10)$$

$$F_\times(\theta, \phi, \psi) = +\frac{1}{2}[1 + \cos^2(\theta)]\sin(2\phi)\cos(2\psi) - \cos(\theta)\sin(2\phi)\sin(2\psi) \quad (1.11)$$

If the gravitational wave is located directly above the interferometer such that $\theta = 0$ and setting $\psi = 0$,

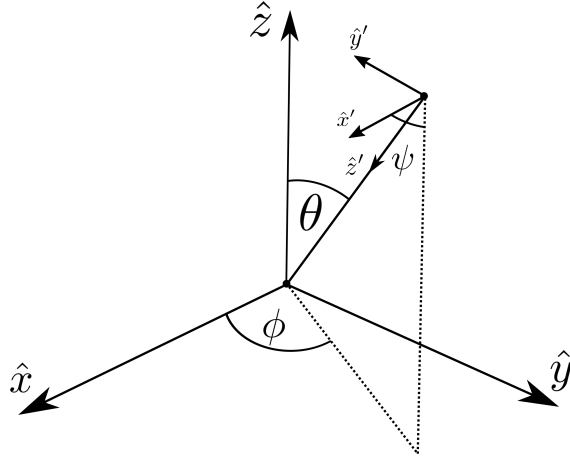


Figure 1.3: **Euler angles of gravitational radiation to the detector frame.** The \hat{x} and \hat{y} coordinates line up with the arms of the interferometer whereas \hat{z}' corresponds to the gravitational wave pointing.

then the magnitude of the antenna pattern is equal to unity. Furthermore, by rotating about the ϕ angle such that the detector arms align with the plus polarization, the null geodesic equation (ie the path of a photon) in the interferometer frame becomes

$$ds^2 = g_{\mu\nu}dx^\mu dx^\nu = -dt^2 + [1 + h_+]dx^2 + [1 - h_+]dy^2 + dz^2 = 0 \quad (1.12)$$

Now, if the photon is traveling along the x-arm, this means that $dy^2 = dz^2 = 0$ and the metric equation transforms to

$$\frac{dt}{dx} = \sqrt{1 + h_+} \approx 1 + \frac{1}{2}h_+ \quad (1.13)$$

The amount of time required for the photon to reach the x-end mirror (starting at $t = 0$) is equal to

$$t_1 = \int_0^{L_x} [1 + \frac{1}{2}h_+(x)] dx \quad (1.14)$$

where L_x is the total length of the x-arm. Upon returning to the beamsplitter, the photon's total time of flight for the x and y arms are, respectively,

$$t_2 = 2L_x + \frac{1}{2} \int_0^{L_x} [h_+(x) + h_+(x + L_x)] dx \quad (1.15)$$

$$t'_2 = 2L_y - \frac{1}{2} \int_0^{L_y} [h_+(y) + h_+(y + L_y)] dy \quad (1.16)$$

If the gravitational wave period is much longer than the time of flight, then h_+ does not change much during the measurement, which means $h_+(\eta_i) \approx h_+(\eta_i + L_{\eta_i}) \approx constant$. By subtracting the flight times of the photons for each arm and setting $L = L_x = L_y$, the difference is proportional to the gravitational wave perturbation multiplied by the sum of arm lengths (with a factor of c to get the units right),

$$\Delta t = t_2 - t'_2 = \frac{2L}{c} h_+ \quad (1.17)$$

By recasting the expression for time of flight in terms of the phase picked up laser light as it travels through space, the differential phase shift is

$$\Delta\Phi = \Phi(t_2) - \Phi(t'_2) = \frac{4\pi}{\lambda} h_+ L \quad (1.18)$$

The equation above is simple, however, it only works for gravitational wave signals that are not frequency dependent and it assumes that the path length can be arbitrarily long. Both points are actually not true [63] but we can alleviate these discrepancies by considering a gravitational wave signal of the form $h(t) = h_0 e^{i2\pi f_{GW} t}$ and repeating the calculation between equations 1.14 and 1.18:

$$\Delta\Phi(t) = h(t) \tau_{RT} \frac{2\pi c}{\lambda} \text{sinc}(f_{GW}\tau_{RT}) e^{i\pi f_{GW}\tau_{RT}} \quad (1.19)$$

where $\tau_{RT} = 2L/c$. The response for a detector has null points from the sinc function that is dependent

on the gravitational wave frequency and the round trip time constant. Which means that the instrument cannot be arbitrarily long, however, this point is not concerning because it is too expensive and difficult to make a terrestrial detector of this size. On the other hand, space-based detectors such as the LISA project will have to account for this effect. Figure 1.4 compares the response of an interferometer with 4 km arms versus 100 km, there is larger low frequency response for the longer detector but has large dips when approaching the kilohertz regime where solar mass compact binaries tend to merge.

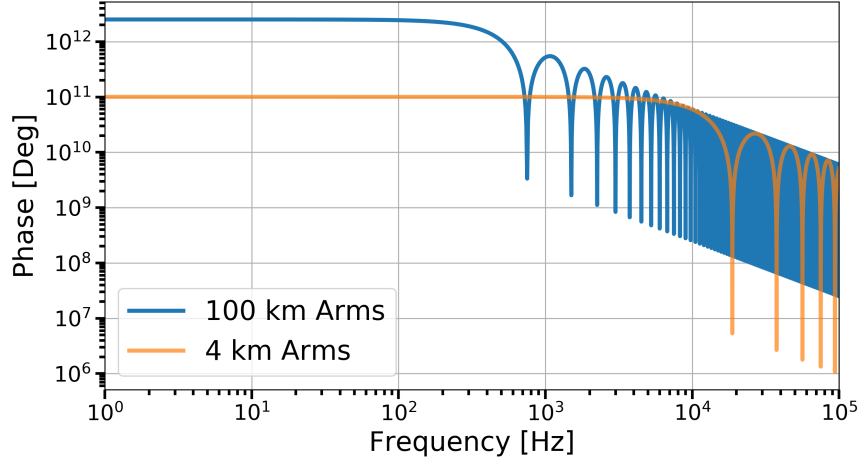


Figure 1.4: The phase response of an interferometer to a gravitational wave. The x-axis is in GW frequency and the y-axis is the accumulated phase

Laying out the response to gravitational waves is one thing but practically measuring $\Delta\Phi$ to detect astrophysical objects requires much more complex systems, so building modern detector is explained in section 2.

1.3 Detection of Gravitational Waves

The purpose of LIGO is to observe gravitational waves emanating from astrophysical objects [29], so it is natural to wonder how well a single detector can probe the universe. It is worthwhile to explicitly derive the inspiral horizon distance, which is how far a single detector can detect a binary system comprised of two equal mass compact objects optimally oriented in the sky relative to the detector. Signal-to-noise (SNR) is the comparison of foreground triggers to the background noise, which can be expressed as

$$\rho = 2 \int_{-\infty}^{\infty} \frac{\tilde{s}(f)\tilde{s}^*(f)}{S_n(f)} \quad (1.20)$$

where $S_n(f)$ is the one-sided average power spectral density of the detector noise and $\tilde{s}(f)$ is the Fourier transform of the detectors' response to a gravitational-wave signal.

Consider two dense objects which are approximated by points sources with mass m_1 and m_2 spiraling around each other. They are separated by a distance R such that the quadrupole equation from 1.2 still holds (i.e. flat space-time with small perturbations). The detector response, in units of strain, to the gravitational waves emitted by this type of source is [32],

$$s(t) = \frac{\mathcal{M}}{d_L} \Theta(\theta, \phi, \psi, i) [\pi f(t) \mathcal{M}]^{2/3} \cos[\Phi(t) + \text{constant}] \quad (1.21)$$

where

$$\mathcal{M} = (1+z) \frac{(m_1 m_2)^{3/5}}{(m_1 + m_2)^{1/5}} \quad (1.22a)$$

$$\Theta(\theta, \phi, \psi, i) = 2 \sqrt{[F_+(\theta, \phi, \psi)(1 + \cos^2(i))]^2 + [2F_X \cos(i)]^2} \quad (1.22b)$$

and F_+ and F_X are the antenna response of the interferometer in equations 1.10 and 1.11. By convention, \mathcal{M} is called the chirp mass and d_L is the luminosity distance. The orientation response, $\Theta(\theta, \phi, \psi, i)$, is a function that depends entirely on the detector orientation relative to the angular momentum vector of the binary. As the system emits gravitational waves, the orbit will shrink as a function of time, in turn, the orbital frequency will increase

$$f(t) = \frac{1}{\pi \mathcal{M}} \left[\frac{5}{256} \frac{\mathcal{M}}{T-t} \right]^{3/8} \quad (1.23)$$

By defining the binary phase as $f(t) = \frac{1}{2\pi} \frac{\partial \Phi}{\partial t}$, it is easy to recognize that the phase also evolves with time.

$$\Phi(t) = 2\pi \int_T^t f(t) dt = -2 \left(\frac{T-t}{5\mathcal{M}} \right)^{5/8} \quad (1.24)$$

What this means is that the gravitational wave signal from the binary will increase in amplitude and frequency as a function of time up until the coalescence time, T . There is actually a subtle difference between the coalescence time and the moment when adiabatic approximations fail which allows usage of the quadrupole formulation.

Plugging equation 1.21 into 1.20,

$$\rho = 8\Theta(\theta, \phi, \psi, i) \frac{r_0}{d_L} \left(\frac{\mathcal{M}}{1.2M_\odot} \right)^{5/6} \zeta(f_{\max}) \quad (1.25)$$

There are two important functions in the equation above that reflect the detector's performance in sensing

gravitational radiation from a binary inspiral, r_0 and $\zeta(f_{\max})$.

The characteristic distance, r_0 is how far the detector can see for a fixed binary's mass distribution,

$$r_0^2 = \frac{5}{192\pi^{4/3}} \left(\frac{3M_\odot}{20} \right)^{5/3} \int_0^\infty \frac{1}{S_n(f)} \frac{df}{f^{7/3}} \quad (1.26)$$

Due to the integrand's dependence on $f^{-7/3}$, lower frequency improvements in the detector's noise spectrum will contribute more to the distance.

$$\zeta(f_{\max}) = \frac{\int_0^{2f_{\max}} \frac{1}{S_n(f)} \frac{df}{f^{7/3}}}{\int_0^\infty \frac{1}{S_n(f)} \frac{df}{f^{7/3}}} \quad (1.27)$$

The sensitivity can be different for various mass distributions; $\zeta(f_{\max})$ is a normalized function that describes how well the detector's bandwidth overlaps the binary's frequency evolution. If f_{\max} sweeps across the detector's most sensitive frequency band (generally between 80 and 400 Hz), there can be relatively good overlap and $\zeta(f_{\max}) \approx 1$. However, if the masses are sufficiently large, f_{\max} will be lower because coalescence occurs before the objects reach a high enough frequency regime and this will result in $\zeta(f_{\max}) \approx 0$.

The process of two compact objects coalescing starts at lower frequencies and terminate at a maximal frequency, f_{\max} , that depends on when the objects reach their inner-most stable circular orbit, f_{ISCO} . If $m_1 = m_2$, then the maximum frequency is [32]

$$f_{\max} = \frac{f_{ISCO}}{1+z} = \frac{99\text{Hz}}{1+z} \frac{20M_\odot}{M} \quad (1.28)$$

where $M = m_1 + m_2$.

Chapter 2

The LIGO Instrument

The previous chapter dealt with gravitational waves and briefly touched on how a laser interferometer is well suited for detecting GWs and in its simplest form, the LIGO instrument is an incredibly large Michelson interferometer. However, to make a practical gravitational-wave observatory, the complexity will have to be extended far beyond what Michelson and Morley used. The next sections will explore the various upgrades to the instrument configuration that improve the sensitivity of LIGO.

2.0.1 Simple Michelson

As shown in Figure 1.2, the interferometer begins with a laser which is incident on a partially-reflecting and partially-transmitting beamsplitter that sends half of the laser light down each arm. The individual beams gather phase as they propagate down the arms and then reflect off of two end mirrors and eventually recombine at the same beamsplitter. Whether the light constructively or destructively interferes will depend on their relative accumulated phase from propagating down each arm. A photodetector is placed at the output and measures the total power which converts the total amount of light into an electronic signal. In Section 1.2, it was shown that the differential time of flight between photons traveling down the individual arms carry gravitational wave information. The difference in flight times, Δt , can be converted into how much phase, $\Delta\phi$, is accumulated by the photons as they propagate through space.

But the question remains, how does an interferometer explicitly measure $\Delta\phi$?

If the input electric field of the interferometer is E_0 , the beamsplitter will transmit $iE_0/\sqrt{2}$ down the x-arm and reflect $E_0/\sqrt{2}$ towards the y-arm. By setting the beamsplitter to be the origin, the two plane waves traveling down their respective arms will have gathered a phase ϕ_i , where the individual arms are denoted by the subscripts. Then, upon reflecting off the end mirrors and returning to the beamsplitter the

resultant fields are transmitted to the antisymmetric port. Each of the electric fields from the arms can be described by these equations

$$\begin{aligned} E_x &= \frac{iE_0}{2}e^{2i\phi_x} \\ E_y &= \frac{iE_0}{2}e^{2i\phi_y} \end{aligned} \quad (2.1)$$

Since the electromagnetic waves are linear, the resultant sum of waves at the antisymmetric port will be $E_{out} = E_x + E_y$. The photodiode at the output (or antisymmetric) port detects the integrated power which is related to the total electric field by

$$\begin{aligned} P_{AS} &= \int_{\text{Area}} I \, dA \\ &= \int_{\text{Area}} |E_x + E_y|^2 \, dA \\ &= P_{in} \cos^2(\Delta\phi) \end{aligned} \quad (2.2)$$

where $\Delta\phi = \phi_x - \phi_y = k_x l_x - k_y l_y$ and $P_{in} = \int_{\text{Area}} |E_0|^2 \, dA$ is the input power. By using equation 1.18 and the common (or average) arm length $l_+ = \frac{l_x + l_y}{2}$, the power due to a differential phase shift is

$$P_{AS}|_{\text{Bright}} \approx P_{in} (1 - 2\Delta\phi) = P_{in} (1 - 2kl_+ h_+) \quad (2.3)$$

There is a large DC term that is dependent on the input power and generally, it is very difficult to measure small changes in a large signal. This configuration can be referred to as being on a bright fringe. So the next obvious method is to shift the arm lengths such that the output port is operating on a dark fringe, normally this is called a null-point operation. However, there are difficulties associated with this method as well. Consider shifting the phase of equation 2.2 by $\pi/2$, which would result in

$$P_{AS}|_{\text{Dark}} = P_{in} \sin^2(\Delta\phi) \approx P_{in} (kl_+ h_+)^2 \quad (2.4)$$

This results in a second-order dependence on a gravitational-wave signal that is already approximated to be very small. So a good solution to the issue of how to *read* out a gravitational wave signal can be remedied using radio frequency (RF) detection methods. By changing the interferometer input from a single laser to adding an electro-optical modulator (EOM) that sinusoidally modulates the laser frequency and expanding

to first order using the Bessel functions,

$$\begin{aligned} E_{in} &= E_0 e^{i(wt + \beta \cos(\Omega t))} \\ &\approx E_0 e^{iwt} [J_0(\beta) + J_1(\beta) e^{i\Omega t} + J_1(\beta) e^{-i\Omega t}] \\ &= E_{C,in} + E_{SB+,in} + E_{SB-,in} \end{aligned} \quad (2.5)$$

where Ω and β are the modulation frequency and depths, respectively. The first term is commonly called the carrier field whereas the second and third terms are referred to as the (upper or lower) sidebands. Because there are multiple electric fields, it is useful to define an optical transfer function which maps the interferometer's input fields to its output,

$$E_{out} = E_C + E_{SB+} + E_{SB-} = \begin{pmatrix} t_C \\ t_{SB+} \\ t_{SB-} \end{pmatrix} \begin{pmatrix} E_{C,in} & E_{SB+,in} & E_{SB-,in} \end{pmatrix} \quad (2.6)$$

The carrier transfer function, t_C has already been calculated by equations 2.2 - 2.4 and the sideband transfer functions are not much different.

$$t_{SB\pm} = r_{x,\pm} e^{i\phi_{\pm,x}} - r_{y,\pm} e^{i\phi_{\pm,y}} \quad (2.7)$$

where $\phi_{\pm,i} = (k \pm k_\Omega) \ell_i = (\frac{w+\Omega}{c}) \ell_i$. In the current example, the sidebands and carrier fields reflect off the end mirrors identically, however, this will not be true in general when dealing with resonators that are highly frequency dependent. Plugging equation 2.7 into 2.6, the output electric field becomes

$$E_{out} = i e^{iwt} [J_0(\beta) k \ell_+ h_+ + J_1(\beta) \sin(k \Delta \ell + k_\Omega \Delta \ell) (e^{i\Omega t} + e^{-i\Omega t})] \quad (2.8)$$

where $\Delta \ell = \frac{l_x - l_y}{2}$ is the average differential arm length. The frequency offset of the sidebands allow them to accumulate phase differently than the carrier field. Thus, by choosing a static offset between the arm lengths such that the carrier signal is on a dark fringe, $k \Delta \ell = \pi/2$, but the sideband are slightly off the null point (Figure [2.1]) and hence leak into the anti-symmetric port. This technique is colloquially known as the *Schnupp Asymmetry* and the electric field reduces to

$$E_{out} = i e^{iwt} [J_0(\beta) k \ell_+ h_+ + J_1(\beta) \sin(k_\Omega \Delta \ell) (e^{i\Omega t} + e^{-i\Omega t})] \quad (2.9)$$

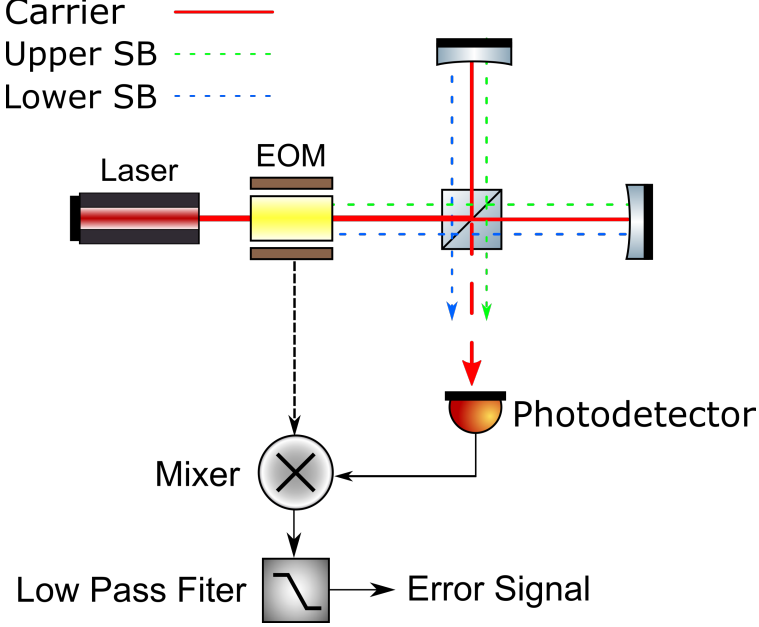


Figure 2.1: **A heterodyne detection scheme for interferometers.** The laser enters an electro-optical modulator which creates three fields described by equation 2.5 and read out by a photodetector. The error signal at the output is then filtered and described by equation 2.12.

The intensity, which is equal to the electric field squared can be described by

$$\begin{aligned}
 I = |E_{out}|^2 &= |E_C|^2 + |E_{SB+}|^2 + |E_{SB-}|^2 \\
 &\quad + 2\text{Re}\{ E_{SB+}E_{SB-}^* e^{2i\Omega t} \} \\
 &\quad + 2\text{Re}\{ (E_C E_{SB-}^* + E_{SB+} E_C^*) e^{i\Omega t} \}
 \end{aligned} \tag{2.10}$$

The last term is referred to as the *beat note* between the carrier signal and the sidebands. It is possible to extract the term at the modulation frequency using a mixer which is an analog device that outputs the product of two inputs. Usually, the same oscillator that was used to modulate the input beam can be one of the mixer inputs, $\cos(\Omega t)$, so that the demodulated signal is

$$\begin{aligned}
 I_{\text{Demod}} &\propto [4\pi J_0(\beta) J_1(\beta) \frac{\ell_+}{\lambda} \sin(k_\Omega \Delta \ell) h_+] [\cos(\Omega t) \sin(\Omega t + \phi_{\text{Demod}})] \\
 &\propto [4\pi J_0(\beta) J_1(\beta) \frac{\ell_+}{\lambda} \sin(k_\Omega \Delta \ell) h_+] [\sin(\phi_{\text{Demod}}) + \sin(2\Omega t + \phi_{\text{Demod}})]
 \end{aligned} \tag{2.11}$$

where ϕ_{Demod} is the phase that can be set by the user in order to account for extra phase shifts (ie. longer cables). After the mixer, there will be signals at DC, Ω , 2Ω and so on. However, the part that is linear in

the gravitational wave amplitude will be at DC so a low-pass filter will allow the final signal to dominate [7]:

$$S = 4\pi J_0(\beta) J_1(\beta) \frac{\ell_+}{\lambda} \sin(k_\Omega \Delta \ell) \sin(\phi_{Demod}) h_+ \quad (2.12)$$

This shows that a RF detection technique will be linear in GW signal with no large DC offset. Setting the carrier on a null point means $\Delta \ell = \frac{k_\Omega \pi}{2}$ and allows the designer to optimize the Schnupp asymmetry length to get the best signal for some modulation frequency. This type of readout scheme was used in Enhanced LIGO and is called heterodyne detection, where the sideband fields are produced by an EOM and its efficacy depends on the local oscillator's stability [35]. In contrast, the Advanced LIGO scheme uses a homodyne detection [43] method called "DC-Readout". Here the oscillator field is produced by slightly offsetting the arms away from the dark fringe and letting a small amount of carrier light through the antisymmetric port. A gravitational wave will induce sidebands on the carrier and this will allow the same mathematics as above to achieve a linear signal in gravitational wave strain. This method benefits from naturally being co-aligned and mode matched with the signal field. All techniques follow the same logic of beating the field containing useful information with a reference field to extrapolate a linear signal but the differences come from technical noise such as laser intensity fluctuations and effective quantum noise.

2.0.2 Fabry-Perot Cavities

There are two ways to improve the LIGO detectors: one is to increase the response from gravitational waves and the other is to decrease the noise contributions. From equation 1.18, the gravitational wave signal is proportional to the optical path length that the photon travels, which means the most straightforward method of increasing the sensitivity is to make the arms as long as possible (up to the null point described by equation 1.19). There are two methods to achieve this: a Herriott delay line or a Fabry-Perot resonator, the differences between each method is shown in Figure 2.2. At the time of writing this thesis, all modern gravitational wave detectors use the latter method.

A Fabry-Perot cavity is an optical system comprised of two or more partially transmitting mirrors with one laser input. To create such a resonator, the user must design a system so that once the electric field has made one round trip within the optical system, the phase of the beam is the same as when it started such that it constructively interferes. This is done by changing the cavity length, which may seem simple conceptually but in practice, controlling and sensing any optical cavity comes with a few challenges.

To start understanding the longitudinal degree of freedom, consider a two mirror system in Figure 2.2 which is separated by a length L with reflection and transmission coefficients: r_1, t_1, r_2, t_2 . Starting with a plane wave at the input mirror with amplitude E_0 , the beam will enter the cavity and propagate back

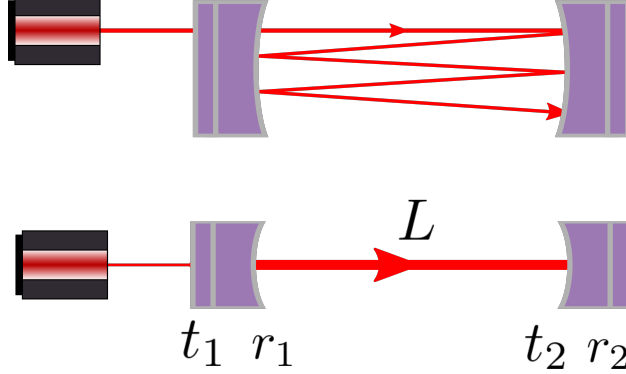


Figure 2.2: Delay Line (top) vs Fabry Perot (bottom)

between the two mirrors. The reflected, transmitted, and circulating fields [63], which are a result of the geometric series, can be described as

$$E_{\text{REFL}} = r_{FP} E_0 = \left(-r_1 + \frac{t_1^2 r_2 e^{-i2kL}}{1 - r_1 r_2 e^{-i2kL}} \right) E_0 \quad (2.13)$$

$$E_{\text{TRAN}} = t_{FP} E_0 = \left(\frac{t_1 t_2 e^{ikL}}{1 - r_1 r_2 e^{-i2kL}} \right) E_0 \quad (2.14)$$

$$E_{\text{CIRC}} = c_{FP} E_0 = \left(\frac{t_1}{1 - r_1 r_2 e^{-2ikL}} \right) E_0 \quad (2.15)$$

The above fields are all highly dependent on the round trip phase accumulated within the cavity which becomes resonant when the length is $L = n\lambda/2$. While on resonance, the circulating coefficient in the cavity is maximized such that the gain is

$$\text{Gain} = c_{FP}^2|_{\text{resonating}} = \left(\frac{t_1}{1 - r_1 r_2} \right)^2 \quad (2.16)$$

Notice that the fields are dependent on the cavity length and laser frequency, $2kL$, so one might naively determine that modulating the two parameters independently cause the same effect. However, when both are changing by large amounts, they are related by a frequency dependent transfer function [51]

$$C(\omega) \frac{\Delta\omega}{\omega} = -\frac{\Delta L}{L} \quad (2.17)$$

where $C(\omega) = \frac{1 - e^{-2i\omega L/c}}{2i\omega L/c}$. It is only when the cavity is on resonance that the frequency and length variations are related by $\frac{\Delta\omega}{\omega} = -\frac{\Delta L}{L}$. Depending on the relative reflection coefficients of the input and output mirrors, the fields on resonance will be different in amplitude. For example, in the LIGO 4 km arms, the end test masses are highly reflective with a transmission of about 4 parts per million while the input test masses

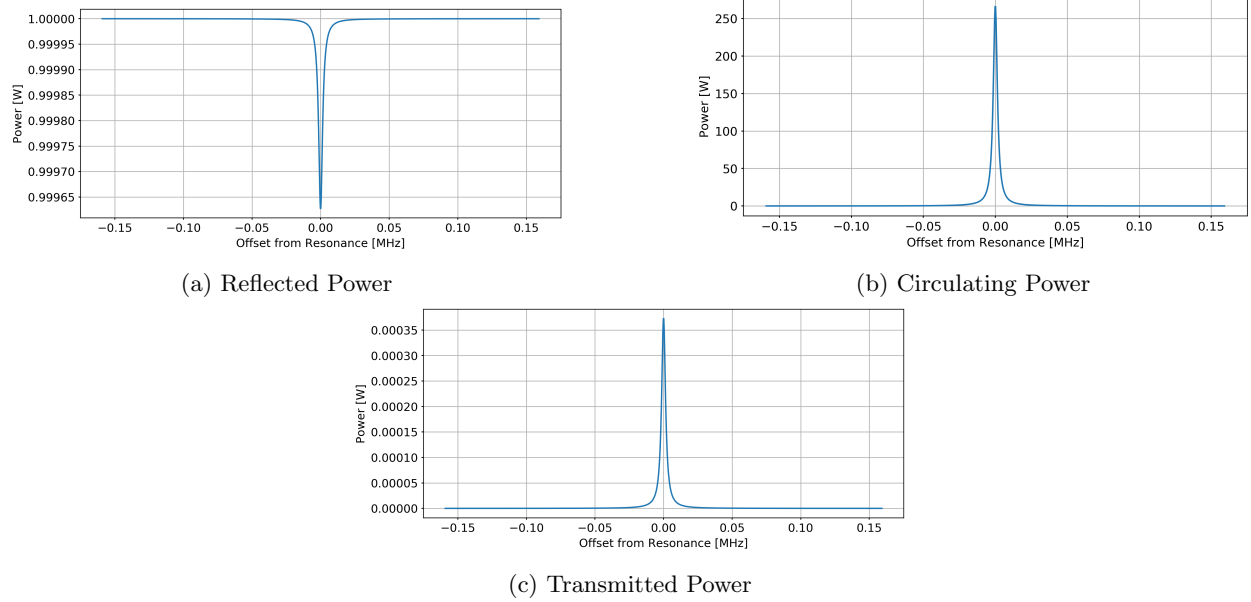


Figure 2.3: The has properties in Table [] to represent one of the LIGO 4km arms which are highly over-coupled cavities so almost all of the light reflects toward the beamsplitter. The input power is normalized to 1 Watt to show the relative gain of the circulating power.

have a transmission of about 0.015. This means that the arm cavities are very much over-coupled and almost all of the light reflects back towards the beamsplitter. It is important to understand the Fabry-Perot

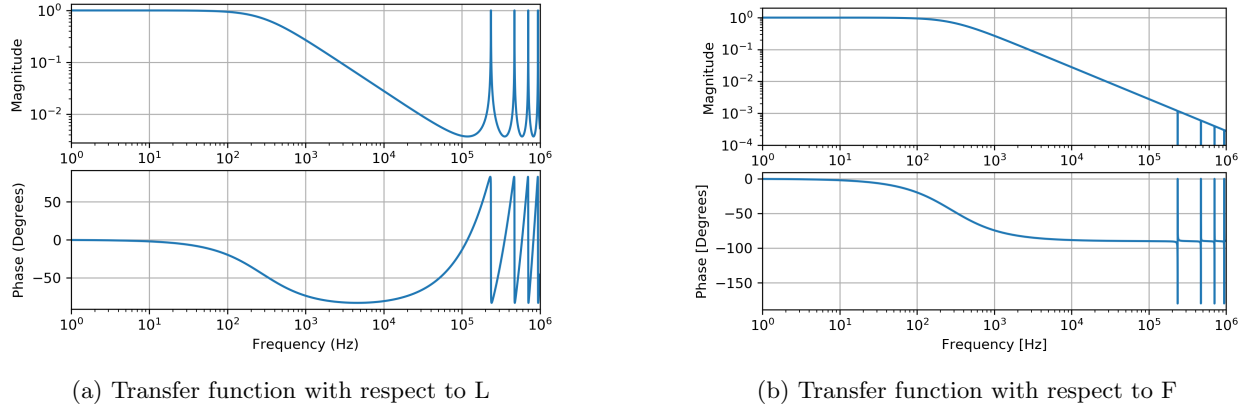


Figure 2.4: Bode Plots of a linear Fabry-Perot response in reflection.

response while sweeping through either the laser frequency or cavity length and measuring the reflected (or transmitted) fields, there are features of the power spectrum which relate directly to the cavity's physical properties.

The finesse describes the line width of the resonant peak and is function of r_1 and r_2 . A higher finesse

will mean the line width is smaller and taller:

$$\mathbb{F} = \frac{\pi\sqrt{r_1 r_2}}{1 - r_1 r_2} \quad (2.18)$$

The cavity storage time, τ_s , describes how long it takes the power circulating in the cavity to decay by a factor of $1/e$ if the laser suddenly turns off,

$$\tau_s = \frac{L}{c\pi} \mathbb{F} \quad (2.19)$$

The pole frequency, f_{pole} , is when the magnitude of the cavity's transfer function (see Figure 2.4) reaches 3db below the DC level:

$$f_{\text{pole}} = \frac{1}{4\pi\tau_s} \quad (2.20)$$

The free spectral range, f_{FSR} , is the frequency span from one resonant peak to the next.

$$f_{\text{FSR}} = \frac{c}{2L} \quad (2.21)$$

It is useful to understand the power circulating as a function of our defined parameters slightly off resonance by a length of ΔL

$$P_{\text{cav}} = |c_{FP}|^2 = \frac{\text{Gain}}{1 + \left(\frac{2\mathbb{F}}{\pi}\right)^2 \sin^2(k\Delta L)} \quad (2.22)$$

In order to prove that an optical cavity is stable, it is useful to introduce the matrices that describe a periodic optical system which is explicitly derived in appendix A. A Fabry Perot cavity that is separated by distance L with spherical mirrors that have radii of curvature R_1 and R_2 will need to satisfy

$$0 \leq \left(1 - \frac{L}{R_1}\right) \left(1 - \frac{L}{R_2}\right) \leq 1 \quad (2.23)$$

in order to be geometrically stable.

LIGO uses the frequency response of optical cavities for a number of reasons: Firstly, the round trip phase of the gravitational wave is amplified by the finesse (equation 2.18) of the 4 kilometer arm cavities, therefore increasing the sensitivity. Secondly, the input and output of the interferometer's Gaussian beam mode can be refined by only allowing the fundamental mode of the laser to resonate (input and output mode cleaners). Thirdly, Advanced LIGO uses a dual-recycled Michelson interferometer which means the symmetric port has a mirror inserted to resonate the light reflected from the Fabry Perot arms (power recycling) and another mirror shapes the frequency response of the differential cavity pole at the anti-symmetric port (signal recycling).

Achieving Resonance in an Optical Cavity

Described above are the theoretical constructs for a Fabry-Perot cavity, but the question remains, how does one practically construct a resonant optical cavity? The answer comes from using a heterodyne sensing scheme similar to the one described in Section 2.0.1. Except the optical system is not a Michelson interferometer but rather a two mirror cavity and can apply to a number of different geometries such as triangular or bow-tie cavities.

Starting with an input laser and EOM (electro-optical modulator) that imparts upper and lower sidebands at a modulation frequency Ω , the user injects three beams into the optical system described in Equation 2.5. When placing a photodetector on the reflection port, one should see the cavity's effect on each of the three electric fields.

$$E_{FP,out} = E_C + E_{SB+} + E_{SB-} = \begin{pmatrix} r_C \\ r_{SB+} \\ r_{SB-} \end{pmatrix} \begin{pmatrix} E_{C,in} & E_{SB+,in} & E_{SB-,in} \end{pmatrix} \quad (2.24)$$

where the reflection coefficients follow equation 2.13. Because sidebands are frequency shifted, they will effectively see a different cavity than the carrier and the total phase accumulated by the two fields will be different. To make a good reference for the resonant carrier beam, the modulation frequency k_Ω , is chosen such that sidebands are anti-resonant which effectively means they are rejected from entering the cavity.

$$r_C = -r_1 + \frac{t_1^2 r_2 e^{-i2kL}}{1 - r_1 r_2 e^{-i2kL}} \quad (2.25)$$

and

$$r_{SB\pm} = -r_1 + \frac{t_1^2 r_2 e^{-i2(k+k_\Omega)L}}{1 - r_1 r_2 e^{-i2(k+k_\Omega)L}} \quad (2.26)$$

The formalism to read out the error signal is shown in Equation 2.10 where a photodetector in reflection (see Figure 2.5) reads out the sum of fields squared and demodulates to get the error signal which will be linearly proportional to the laser frequency and cavity length [7].

$$\text{Error Signal} \propto \frac{LF}{\lambda} \left[\frac{\delta w}{w} + \frac{\delta L}{L} \right] \quad (2.27)$$

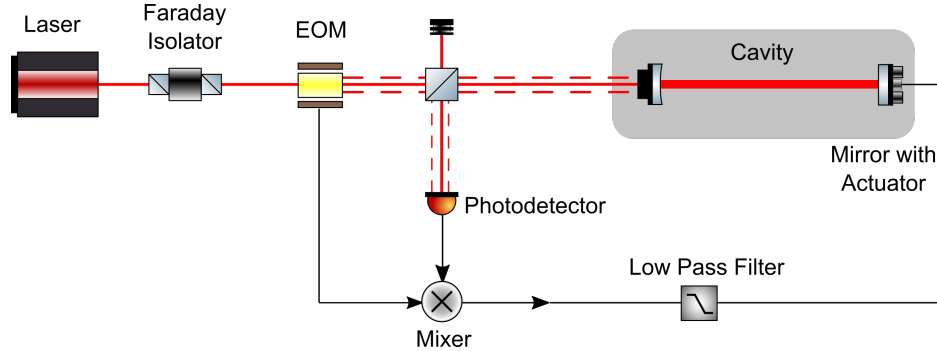


Figure 2.5: **Control scheme for an optical cavity.** The electric fields in reflection provide the error signal when mixed with the local oscillator and then gets low-passed for a DC signal to drive the end mirror which will control the length of the cavity, see Figure 2.6.

2.0.3 Fabry-Perot Michelson

Using an optical cavity to increase the number of bounces along the 4 kilometer arms will amplify the gravitational wave signal but it will also shape the frequency dependence of the sensitivity as well. This has already been alluded to in section 1.2 where the overall increase in arm length will tune the response function of equation 1.19. The same idea can apply to integrate the use of Fabry-Perot arms into a Michelson interferometer and looking at the signal at the antisymmetric port as a function of gravitational wave frequency. Previously in section 2.0.1, it was shown that the heterodyne RF detection technique required beating the sidebands with a carrier field containing the gravitational wave information. However, this is not the only way because the signal sidebands beating with a reference carrier field could also be a valid way of measuring a signal of interest. In fact, Advanced LIGO employs a specific type of homodyne detection called DC readout [35][22]. The idea is that the carrier field will resonate in the arms but will be slightly modulated due to a gravitational wave which will create audio frequency sidebands imparted on the field.

Figure 2.7 shows an input electric field of E_0 incident on a 50/50 beamsplitter which then enters two orthogonal arm cavities of length L_x and L_y . Notice that the distance from the beamsplitter to the input couplers for both arms denoted by l_x and l_y are independent variables, this is to account for the DARM offset which is analogous to the Schnupp asymmetry described in section 2.0.1. After partially transmitting and reflecting at the beamsplitter, the fields will resonate in each of the arm cavities and obey the reflectivity relations described by equation 2.13. Upon recombining at the beamsplitter, the antisymmetric port electric field will be related to the arm fields by,

$$E_{AS} = \frac{1}{\sqrt{2}}[E_x^{\text{ARM}} + E_y^{\text{ARM}}] \quad (2.28)$$

where $E_i^{\text{ARM}} = E(\omega) \pm [E(+\omega_{\text{GW}}) + E(-\omega_{\text{GW}})] \sin k\delta l$ is the reflected fields for the x and y arms which

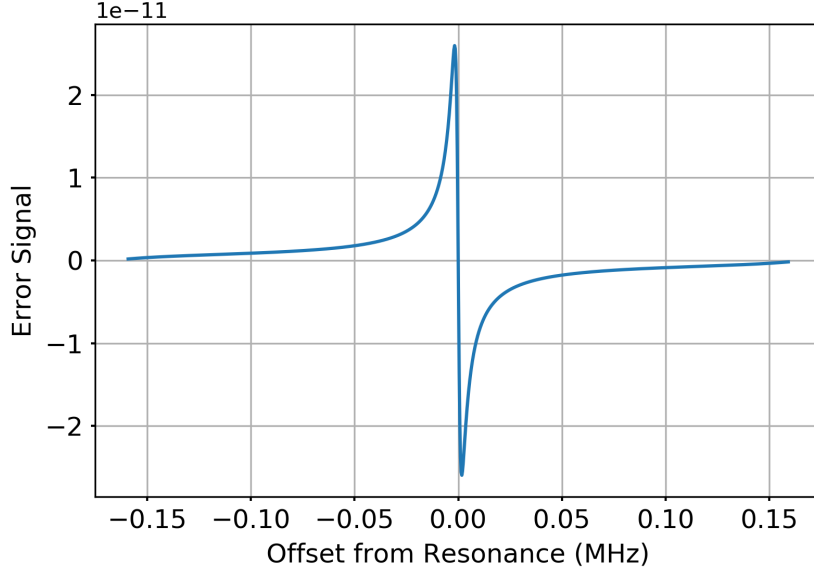


Figure 2.6: **Pound-Drever-Hall (PDH) error signal in reflection of a Fabry Perot cavity.** By modulating the frequency (or length) close to the zero offset point, the error signal is linear. However, if the actuation is too far away from the lock point, the signal becomes highly non-linear. Which means the drive output must wait until the error signal comes close enough to zero before triggering on.

contain the carrier(first term) and GW signal sidebands(last two terms). In this case, the gravitational wave sidebands are a single frequency for simplicity but this analysis will work for all frequencies spanning the LIGO sensitivity band. Intuitively, one can deduce that the antisymmetric port will only be sensitive to the differential motion between the arm cavities, which means the gravitational wave sidebands in the x-arm will be out of phase with the y-arm. Also it is important to note that inserting a DC microscopic length shift of a few picometers represented by $\delta l = l_x - l_y$ allows for some carrier leakage field to propagate towards the antisymmetric port which creates the static reference to form a beat note with the signal sidebands. The same effect can be achieved by introducing a static offset between the x and y arms; colloquially, this is referred to as DARM offset.

For the carrier field, the amplitude of reflection is simple because the LIGO arms are a strongly over-coupled cavity operating on resonance therefore

$$E(\omega) = \frac{E_0}{\sqrt{2}} \left(-r_1 + \frac{t_1^2 r_2}{1 - r_1 r_2} \right) \approx -\frac{E_0}{\sqrt{2}} \quad (2.29)$$

The sidebands are a different story because the modulation caused by the gravitational wave slightly move the field off resonance. Imagine the carrier circulating in the arms and then suddenly, a disturbance due to a gravitational wave displaces the end mirror at a frequency ω_{GW} by an amount ΔL . By using the

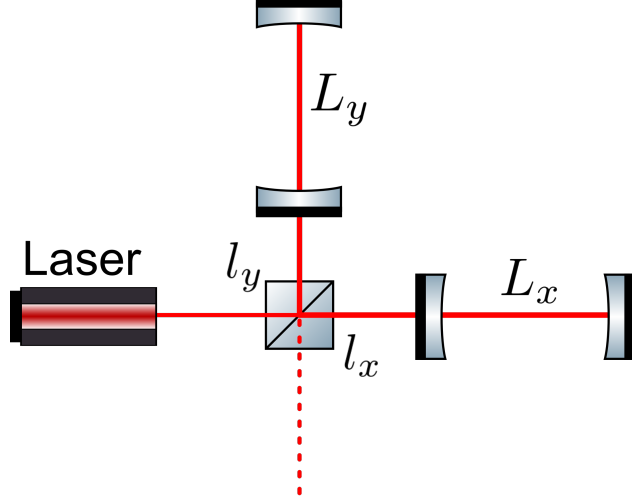


Figure 2.7: Michelson with Fabry Perot arms

same formalism as the expansion of a modulated field in equation 2.5, the sideband fields can be described by,

$$\begin{aligned} E(\pm\omega_{\text{GW}}) &= \left[\frac{t_1}{1 - r_1 r_2 e^{-2ikL}} \right] \frac{E_0}{\sqrt{2}} \left[\frac{t_1}{1 - r_1 r_2 e^{-2i(kL \pm \omega_{\text{GW}} \frac{L}{c})}} \right] ik\Delta L \\ &= \left[\frac{t_1^2}{1 - r_1 r_2} \right] \frac{E_0}{\sqrt{2}} \left[\frac{1}{1 - r_1 r_2 e^{-2i\omega_{\text{GW}} \frac{L}{c}}} \right] ik\Delta L \end{aligned} \quad (2.30)$$

The first bracket is the circulating field of the carrier signal amplified by the Fabry Perot cavity and the second bracket is the circulating field slightly off resonance due to the gravitational wave frequency offset. Setting the fields to resonate already simplifies the equation but it is also reasonable to approximate the gravitational wave as a weak signal and expand the exponential $e^{-2i\omega_{\text{GW}} \frac{L}{c}} \approx 1 - 2i\omega_{\text{GW}} \frac{L}{c}$. This transforms the signal sideband field into a simple form,

$$E(\pm\omega_{\text{GW}}) \approx \left[\frac{t_1}{1 - r_1 r_2} \right]^2 \frac{E_0}{\sqrt{2}} \left[\frac{1}{1 \pm i \frac{\omega_{\text{GW}}}{\omega_p}} \right] ik\Delta L \quad (2.31)$$

where $\omega_p = \frac{1 - r_1 r_2}{r_1 r_2} \frac{c}{2L}$ is the differential pole frequency; notice that it matches the single arm cavity pole.

The photodiode signal at the antisymmetric port is proportional to the beat note between the carrier and signal sideband after demodulation in the audio band with a phase ϕ_D ,

$$\begin{aligned} S &\propto 2[E(\omega)E^*(-\omega_{\text{GW}}) + E(-\omega_{\text{GW}})E^*(\omega)] \sin(k\delta l) \sin(\phi_D) \\ &\propto E_0^2 \frac{8\pi L}{\lambda} \left[\frac{t_1}{1 - r_1 r_2} \right]^2 \left[\frac{1}{1 - i \frac{\omega_{\text{GW}}}{\omega_p}} \right] \sin(k\delta l) \sin(\phi_D) h_{\text{GW}} \end{aligned} \quad (2.32)$$

where the length disturbance ΔL was transformed to originate from a gravitational wave signal $k\Delta L = \frac{2\pi L}{\lambda} h_{\text{GW}}$. The response of this particular interferometer to differential arm length motion is linearly propor-

tional to the gravitational wave amplitude as well as the input power $P_0 \propto E_0^2$, but there is also a frequency dependent component which is the same as a single Fabry-Perot cavity. This acts like a low pass filter above the corner frequency colloquially called the darm cavity pole.

2.0.4 Power-Recycled Fabry-Perot Interferometers

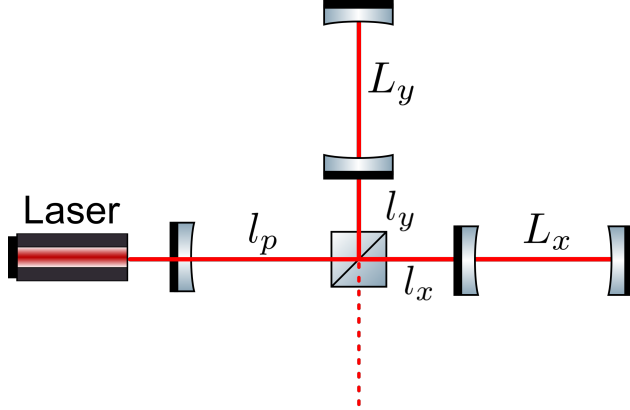


Figure 2.8: **A power recycled Fabry-Perot interferometer.** Adding a mirror at the symmetric port forms another resonator called the power recycling cavity (PRC) where the distance between from the power recycling mirror (PRM) to the beamsplitter is denoted by l_p . The power recycling cavity can actually be viewed as two linear cavities with the PRM making a cavity with each ITM.

If the interferometer is operating such that the intensity at the antisymmetric port is close to null, conservation of energy requires that the arm powers will reflect back towards the input laser. Fritschel et al [36] [33] showed the effects of adding a partially reflecting mirror to increase the Michelson optical gain for both the sideband and carrier fields.

Section 2.0.3 showed that the Michelson interferometer with Fabry Perot arms can be represented by a single cavity response. Therefore it is useful to model a power recycled interferometer by using a coupled cavity approach where the input mirror is replaced with the reflected field of the Michelson on a bright fringe. Here the reflectivity and transitivity of the power recycling mirror (PRM) is denoted by r_p and t_p , respectively.

In this configuration, the effective length of the cavity is the average path between the power recycling mirror and the high reflectivity surfaces of the input test masses,

$$l_{\text{PRC}} = l_p + \frac{l_x + l_y}{2} \quad (2.33)$$

The circulating power in the cavity is given by equation 2.15 but uses the reflectivity of arm cavities,

$$E_{\text{PRC}} = \frac{t_p}{1 - r_p r_{\text{FPM}} e^{-2ikl_{\text{PRC}}}} E_{\text{in}} \quad (2.34)$$

where $r_{\text{FPM}} \approx 1 - \frac{\mathbb{F}}{\pi} \mathcal{L}_{\text{ARM}}$ for high finesse cavities and the round trip arm cavity losses are denoted by \mathcal{L}_{ARM} . This is a valid approximation for the advanced LIGO arm cavities since their values for finesse can be around 250 or higher depending on the losses. This means the circulating power in the recycling cavity while on resonance can be expressed by

$$P_{\text{PRC}} = \frac{1 - r_p^2}{\left[1 - r_p(1 - \frac{\mathbb{F}}{\pi} \mathcal{L}_{\text{ARM}})\right]^2} P_{\text{in}} \quad (2.35)$$

By taking the derivative with respect to r_p and setting to zero, the optimal power recycling tuning is linearly proportional to the round trip loss,

$$r_{\text{opt}} = 1 - \frac{\mathbb{F}}{\pi} \mathcal{L}_{\text{ARM}} \quad (2.36)$$

so it is important to keep the arm cavity losses as low as possible and this also limits the ability to increase the finesse.

Adding a power recycling mirror will be equivalent to introducing higher power into the arm cavities but it will not shape the gravitational wave sideband frequency dependence in any other way. This can be reasoned qualitatively by imagining the signal sidebands that get created in the arm cavities and propagate to the beam splitter where they will combine, however, the stretching and squeezing from the gravitational wave pattern will make the x-arm shorter while lengthening the y-arm and vice versa. This makes the anti-symmetric port transmissive to the signal sidebands but the carrier field which mostly gets reflected to the symmetric port will see the power recycling amplification. This means the beat note between the static carrier field and gravitational wave signal for a power recycled Fabry-Perot interferometer is

$$S_{\text{PRFP}} \propto E_0^2 \frac{8\pi L}{\lambda} \sqrt{g_{\text{PRC}}} \left[\frac{t_1}{1 - r_1 r_2} \right]^2 \left[\frac{1}{1 - i \frac{\omega_{\text{GW}}}{\omega_p}} \right] \sin(k\delta l) \sin(\phi_D) h_{\text{GW}} \quad (2.37)$$

where $g_{\text{PRC}} = P_{\text{PRC}}/P_{\text{in}}$ is the power recycling gain.

2.0.5 Dual-Recycled Fabry-Perot Interferometers

One of the biggest changes made between initial and advanced LIGO was the addition of a signal recycling mirror at the antisymmetric port (Figure 2.9). In the previous section, it was shown that the gravitational

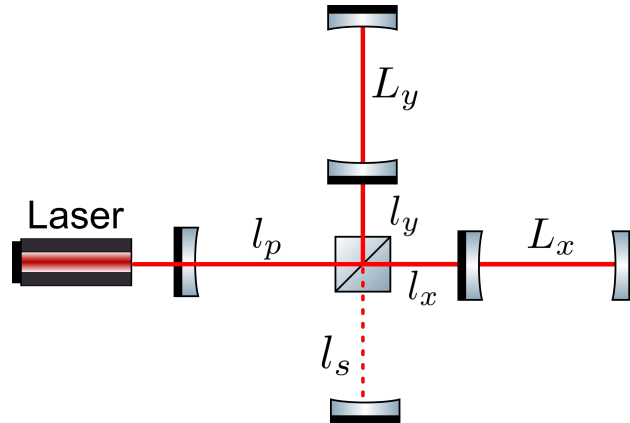


Figure 2.9: **A dual recycled Fabry-Perot interferometer.** Adding a signal recycling mirror (SRM) at the anti-symmetric port will change how the gravitational wave signal is read. Similar to the power recycling cavity, adding a mirror at the output port will create a resonator with the input test masses.

wave sensitivity was improved by adding a power recycling cavity to increase the effective input power into the Fabry-Perot cavities. Adding another partially reflecting optic called the signal recycling mirror (SRM) at the antisymmetric port to create a resonant cavity will shape the interferometer's response to gravitational waves. This allows for some flexibility in optimizing the instrument for specific sources such as binary neutron stars, but it also creates a more broadband response at higher frequencies while allowing the arm cavity finesse and/or power recycling to impart more power.

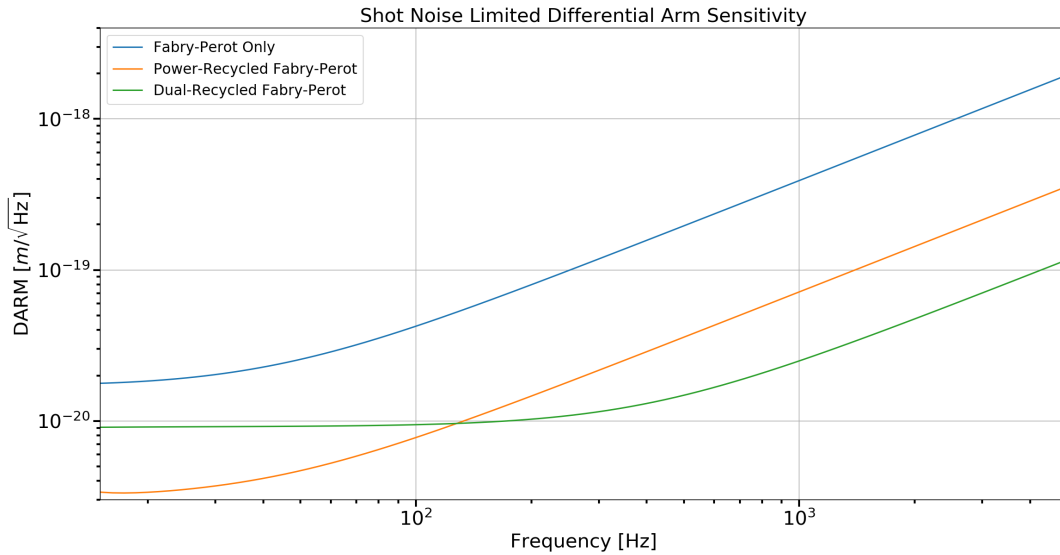


Figure 2.10: Shot noise limited sensitivity

A nice way to model the effect of signal recycling on the gravitational wave sidebands is to combine the SRM and arm cavity input test mass to create a combined mirror that is dependent on the round trip phase,

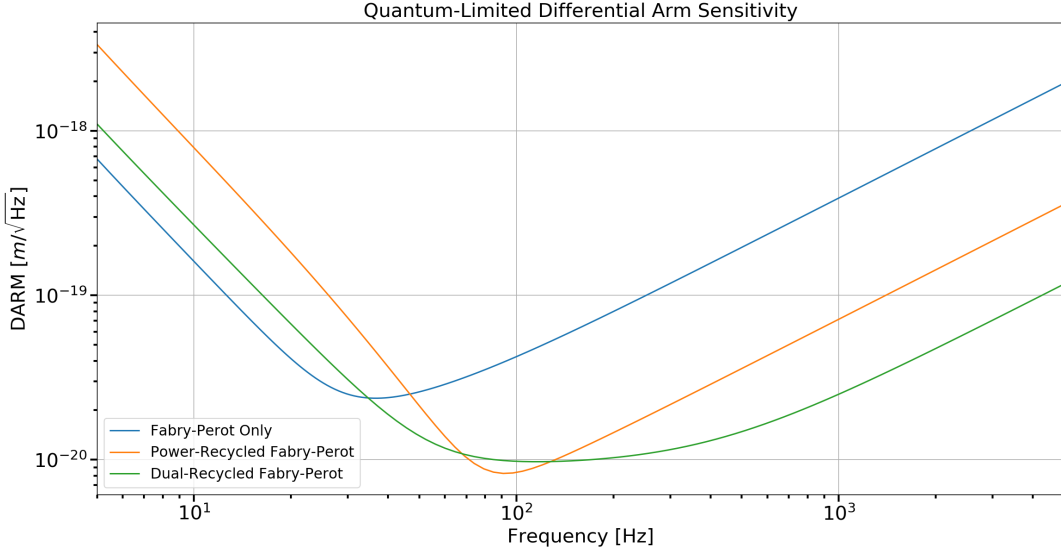


Figure 2.11: Quantum limited sensitivity by combining shot noise and radiation pressure

ϕ_s of the signal recycling cavity. The SRM will have a reflectivity and transmissivity equal to r_s and t_s , respectively, so the combined mirror will have a reflectivity and transmissivity equal to

$$r_{1+s} = \frac{r_1 - r_s e^{-2i\phi_s}}{1 - r_1 r_s e^{-2i\phi_s}} \quad (2.38)$$

$$t_{1+s} = \frac{t_1 t_s e^{i\phi_s}}{1 - r_1 r_s e^{-2i\phi_s}} \quad (2.39)$$

where $\phi_s = k(l_s + \frac{l_x+l_y}{2})$ is the average signal recycling length. Plugging this into equation 2.30 in place of the input test mass reflectivity shows that the cavity pole is directly affected by the signal recycling properties, namely, the SRM reflectivity and the microscopic detuning of the length. The field propagating to the true antisymmetric port is in transmission of the signal recycling cavity which is accounted for with the last bracketed term.

$$\begin{aligned} E_{AS}(\pm\omega_{GW}) &= \left[\frac{t_1^2}{1 - r_1 r_2} \right] \frac{E_0}{\sqrt{2}} \left[\frac{1}{1 \pm r_{1+s} r_2 e^{-2i\omega_{GW} \frac{L}{c}}} \right] \left[\frac{t_1 t_s e^{i\phi_s}}{1 - r_1 r_s e^{-2i\phi_s}} \right] i k \Delta L \\ &\propto \left[\frac{\text{Constant}}{1 \pm 2i \frac{r_{1+s} r_2}{1 - r_{1+s} r_2} \omega_{GW} \frac{L}{c}} \right] \\ &\propto \left[\frac{\text{Constant}}{1 \pm i \omega_{GW} / \omega_{DR}} \right] \end{aligned} \quad (2.40)$$

Here, the frequency dependence of the differential cavity pole with dual recycling is denoted by

$$\begin{aligned}\omega_{\text{DR}} &= \frac{1 - r_{1+s}r_2}{r_{1+s}r_2} \frac{c}{2L} \\ &= \frac{1 - r_1r_s e^{-2i\phi_s}}{(r_1 - r_s e^{-2i\phi_s})r_2} - 1\end{aligned}\quad (2.41)$$

Figure[ifoconfigs] The carrier field will also see a gain from the signal recycling cavity equal to

$$\sqrt{g_{\text{SRC}}} = \frac{t_s}{1 + r_s r_{\text{FPMe}} e^{-2i\phi_s}} \quad (2.42)$$

It is clear from the equations above that the gravitational wave sideband and carrier fields will see the signal recycling cavity effects differently and the responses are highly sensitive to the length detuning of ϕ_s . Putting all the pieces together to get the dual recycled Fabry-Perot interferometer response to gravitational waves,

$$S_{\text{DRFP}} \propto E_0^2 \frac{8\pi L}{\lambda} \sqrt{g_{\text{PRC}}} \sqrt{g_{\text{SRC}}} g_{\text{ARM}} \left[\frac{1}{1 - i \frac{\omega_{\text{GW}}}{\omega_{\text{DR}}}} \right] \sin(k\delta l) \sin(\phi_D) h_{\text{GW}} \quad (2.43)$$

The previous sections only considered the effect of Fabry-Perot cavities and recycling mirrors at the anti-symmetric port (AS) due to the differential length change (DARM) of the 4 kilometer arms but the Advanced LIGO interferometer has a few lengths which are actively controlled. The other degrees of freedom include the common arm length (CARM), the power recycling length (PRCL), and signal recycling length(SRCL). These signals are sensitive at ports other than AS, such as in reflection of PRM (REFL) and a pick off port in the power recycling cavity (POP). A good reference for what signals are expected at these important readout points can be found in [45] [46] [47]

2.0.6 Fundamental Noise Sources

The proceeding sections describe ways to increase the response of LIGO to gravitational waves; equally as important is the science of characterizing and reducing the noise contributions from everything that is not gravitational waves to optimize the sensitivity.

Quantum Noise

Virtually all undergraduate quantum mechanics textbooks include a section on the harmonic oscillator [[68]]. A particularly interesting result when solving the Schrödinger equation using creation (\hat{a}^\dagger) and annihilation (\hat{a}) operators is the existence of a non-zero energy ground state which has variances in momentum and position related by the Heisenberg uncertainty principle. When it comes to electromagnetic fields, the pair associated

with the uncertainty principle is the amplitude and phase of the laser beam.

As a result, one of the main noise sources that is limiting LIGO's sensitivity comes from the fluctuations of quantum vacuum entering the anti-symmetric port and coupling to the input laser. A quantum mechanical description of an interferometer was constructed by Caves [15][16] [17], where he used electric field operators to show that vacuum fluctuations are the cause of radiation pressure and shot noise in a simple interferometer (no resonant cavities). The following analysis below will also be simplified in this way but is reasonably close in estimating the amount radiation pressure and shot noise. For studies that take into account more complicated interferometer configurations with resonant cavities refer to Buonanno and Chen [13] [19]. In general, there has been an explosion of research efforts associated with lowering the noise contributions from vacuum fluctuations [48].

Quantum states: It is well known in physics [68] [39] that a solution to the quantum harmonic oscillator in the energy eigenbasis employs the annihilation and creation operators, \hat{a}^\dagger and \hat{a} , to factorize the Hamiltonian

$$\hat{H} = \hbar\omega(\hat{N} + 1/2) \quad (2.44)$$

where $\hat{N} = \hat{a}^\dagger\hat{a}$ is the number operator. When using this formalism to create a coherent electromagnetic field, it is useful to define a unitary operator that displaces the vacuum state [37]:

$$\hat{D} \equiv \hat{D}(\alpha) \equiv \exp(\alpha\hat{a}^\dagger - \alpha^*\hat{a}) = e^{-\frac{|\alpha|^2}{2}} e^{\alpha\hat{a}^\dagger} e^{\alpha^*\hat{a}} \quad (2.45)$$

and has the properties,

$$\begin{aligned} \hat{D}(\alpha) &= \hat{D}^{-1}(\alpha) = \hat{D}(-\alpha) \\ \hat{D}^\dagger \hat{a} \hat{D} &= \hat{a} + \alpha \\ \hat{D}^\dagger \hat{a}^\dagger \hat{D} &= \hat{a}^\dagger + \alpha^* \end{aligned} \quad (2.46)$$

When applying the displacement operation on the vacuum state, the resultant vector has an amplitude α and follows the same uncertainty distribution as an unperturbed vacuum vector as shown in Figure[StickandBall],

$$|\alpha\rangle = \hat{D} |0\rangle = e^{-\frac{|\alpha|^2}{2}} e^{\alpha\hat{a}^\dagger} |0\rangle \quad (2.47)$$

Radiation Pressure

One might naively think that power fluctuations in the main laser causes radiation pressure effects on the test masses which will result in noise. However, if the 50/50 beamsplitter is perfect, then the momentum transfer to each test mass will result in a common length change and will not vary the intensity at the antisymmetric port (or the symmetric port for that matter). However, the baseline laser power will be

important when considering a full quantum mechanical picture of radiation pressure.

Consider plane wave waves entering the interferometer from both the symmetric and anti-symmetric ports. This method is similar to the input-output methods of section 2.0.1, however, the difference being that the beamsplitter will couple the electric fields from the input laser and quantum vacuum.

The electric fields combine at the beamsplitter from both ports and add linearly,

$$E_x = \frac{1}{\sqrt{2}} \left[iE_0 + E_{AS,in} \right] \quad (2.48a)$$

$$E_y = \frac{1}{\sqrt{2}} \left[E_0 + iE_{AS,in} \right] \quad (2.48b)$$

where E_0 is the input field from the laser and $E_{AS,in}$ is the field from the anti-symmetric port. The electric fields will travel down each arm and strike the mirrors with intensities denoted by,

$$|E_x|^2 = \frac{1}{2} \left[|E_0|^2 + |E_{AS,in}|^2 + i(E_0 E_{AS,in}^* - E_0^* E_{AS,in}) \right] \quad (2.49a)$$

$$|E_y|^2 = \frac{1}{2} \left[|E_0|^2 + |E_{AS,in}|^2 - i(E_0 E_{AS,in}^* - E_0^* E_{AS,in}) \right] \quad (2.49b)$$

Therefore, differential momentum transfer between the two masses will be equal to the differences in intensities between the two arms:

$$\begin{aligned} \mathbf{P} &= \frac{2\hbar\omega}{c} \left(|E_x|^2 - |E_y|^2 \right) \\ &= \frac{2\hbar\omega}{c} \left(E_0 E_{AS,in}^* - E_0^* E_{AS,in} \right) \\ \Rightarrow \hat{\mathbf{P}} &= \frac{2\hbar\omega}{c} \left(\hat{a}_1^\dagger \hat{a}_2 - \hat{a}_2^\dagger \hat{a}_1 \right) \end{aligned} \quad (2.50)$$

The last part of equation 2.50 replaces the classical electric fields with creation and annihilation operators for the symmetric input mode ($\hat{a}_1^\dagger, \hat{a}_1$) and antisymmetric input mode ($\hat{a}_2^\dagger, \hat{a}_2$) modes. Recall that there is a well established convention denoting the wave function of the two dimensional modes of the quantum harmonic oscillator [37], $|\alpha, \beta\rangle$, where α denotes the input symmetric mode and β refers to the input antisymmetric mode:

$$|\alpha, 0\rangle = \hat{D}_1(\alpha) |0, 0\rangle \quad (2.51)$$

The interesting results arising from this formulation is the expectation value turns out to be null,

$$\langle \hat{\mathbf{P}} \rangle = \langle \alpha, 0 | \hat{\mathbf{P}} | \alpha, 0 \rangle = 0 \quad (2.52)$$

However, the variance of the momentum transfer is non-zero,

$$\begin{aligned}\Delta\mathbf{P}^2 &= \langle \hat{\mathbf{P}}^2 \rangle - \langle \hat{\mathbf{P}} \rangle^2 \\ &= \left(\frac{2\hbar\omega}{c} \right)^2 \langle \alpha, 0 | \hat{a}_1^\dagger \hat{a}_2 \hat{a}_1 \hat{a}_2^\dagger + \hat{a}_2^\dagger \hat{a}_1 \hat{a}_2 \hat{a}_1^\dagger - \hat{a}_2^\dagger \hat{a}_1 \hat{a}_1 \hat{a}_2^\dagger - \hat{a}_1^\dagger \hat{a}_2 \hat{a}_2 \hat{a}_1^\dagger | \alpha, 0 \rangle \\ &= \left(\frac{2\hbar\omega}{c} \right)^2 |\alpha|^2\end{aligned}\quad (2.53)$$

For some time interval ΔT , the input laser power consisting of $\langle N \rangle = |\alpha|^2$ photons is

$$P_{in} = \frac{\hbar\omega}{\Delta T} |\alpha|^2 \quad (2.54)$$

To solve for the amplitude spectral density of the displacement, Newton's second law can be applied in the frequency domain

$$M(2\pi f)^2 \tilde{x}(f) = \tilde{F}(f) = \frac{\Delta\mathbf{P}}{\Delta T} \quad (2.55)$$

Here, the quantum radiation force spectrum, $\tilde{F}(f)$, is actually flat in frequency because the impacting photons have a randomly distributed amplitude but this gives a straightforward pathway to calculate the displacement spectrum ,

$$\tilde{x}_{RP}(f) = \sqrt{\frac{\hbar\omega}{\Delta T} P_{in}} \frac{1}{2Mc(\pi f)^2} \quad (2.56)$$

This means the noise spectral density of radiation pressure for an interferometer with a mirror of mass $M = 40$ kg, input power $P_{in} = 125$ Watts, and laser frequency $\lambda = 1064$ nm

$$\tilde{h}_{RP}(f) = 2.04 \times 10^{-20} \frac{1}{f^2} \left[\frac{\text{Strain}}{\sqrt{\text{Hz}}} \right] \quad (2.57)$$

So it is shown that the contribution of quantum radiation pressure in a simple interferometer increases with the square root of the input power.

Shot Noise

Another way that quantum fluctuations at the antisymmetric port can vary the sensitivity is by adding phase noise. Imagine holding the test masses rigidly such that the only effects on the output light is due to a phase change in the laser light in the arms. By using the same formulation for radiation pressure but propagating the fields back to the beam splitter, equations 2.48 will have extra phase that depends on the arm lengths are denoted by l_x and l_y in a simple Michelson interferometer,

$$E_{x,\text{out}} = \frac{1}{\sqrt{2}} \left[iE_0 + E_{AS,\text{in}} \right] e^{-i2kl_x} \quad (2.58a)$$

$$E_{y,\text{out}} = \frac{1}{\sqrt{2}} \left[E_0 + iE_{AS,\text{in}} \right] e^{-i2kl_y} \quad (2.58b)$$

Therefore the antisymmetric port field is described by

$$\begin{aligned} E_{AS,\text{out}} &= \frac{1}{\sqrt{2}} (E_{x,\text{out}} + iE_{y,\text{out}}) \\ &= ie^{-ikl_x - ikl_y} [\cos(\Delta\phi)E_0 - \sin(\Delta\phi)E_{AS,\text{in}}] \end{aligned} \quad (2.59)$$

where $\Delta\phi = k(l_x - l_y)$ is used for brevity. The intensity is once again found by squaring the electric field,

$$\begin{aligned} \mathbf{I}_{AS,\text{out}} &= |E_{AS,\text{out}}|^2 \\ &= \left[\cos^2(\Delta\phi)|E_0|^2 + \sin^2(\Delta\phi)|E_{AS,\text{in}}|^2 - \sin(\Delta\phi)\cos(\Delta\phi)[E_0E_{AS,\text{in}}^* + E_0^*E_{AS,\text{in}}] \right] \\ \Rightarrow \hat{\mathbf{I}}_{AS,\text{out}} &= \left[\cos^2(\Delta\phi)a_1^\dagger a_1 + \sin^2(\Delta\phi)a_2^\dagger a_2 - \sin(\Delta\phi)\cos(\Delta\phi)[a_1^\dagger a_2 + a_2^\dagger a_1] \right] \end{aligned} \quad (2.60)$$

The expectation value for the intensity using an input coherent laser with α and quantum vacuum input at the antisymmetric port is

$$\begin{aligned} \langle \hat{\mathbf{I}} \rangle &= \langle \alpha, 0 | \hat{\mathbf{I}}_{AS,\text{out}} | \alpha, 0 \rangle \\ &= \cos^2(\Delta\phi)|\alpha|^2 \end{aligned} \quad (2.61)$$

which matches the classical description of a Michelson output described in section 2.0.1. Following the same methods to calculate the radiation pressure, photon number variance is

$$\begin{aligned} \Delta \mathbf{I} &= \sqrt{\langle \hat{\mathbf{I}}^2 \rangle - \langle \hat{\mathbf{I}} \rangle^2} \\ &= |\alpha| [\cos^2(\Delta\phi)] \end{aligned} \quad (2.62)$$

In order to cast the variance into an expected phase noise, consider the derivative of the intensity with respect to the phase and plugging in the input power,

$$\frac{\partial I}{\partial \phi} = -2|\alpha|^2 \cos(\Delta\phi) \sin(\Delta\phi) \quad (2.63)$$

$$\delta\phi = \sqrt{\frac{\hbar\omega}{P_{\text{in}}}} \cot(\Delta\phi) \quad (2.64)$$

Here $\delta\phi$ is the microscopic change in phase due to shot noise, whereas $\Delta\phi$ is the DC offset in the arm lengths to begin with. So in general, the shot noise contribution is dependent on the amount of light present at the anti-symmetric port and this will vary depending on what type of signal readout scheme is implemented. To calculate the shot noise sensitivity, the phase shift in shot noise can be scaled by a factor of $\frac{\lambda}{2\pi} \frac{1}{L}$ where λ is

the laser wavelength and L is the DC length of the Michelson arms,

$$\tilde{h}_{SN}(f) = 8.2 \times 10^{-22} \left[\frac{\text{Strain}}{\sqrt{\text{Hz}}} \right] \quad (2.65)$$

Unsurprisingly, the shot noise is proportional to $1/\sqrt{P_{\text{in}}}$ and the initial phase difference between the interferometer arms. There are a few subtleties associated with measuring shot noise, this model assumes that the interferometer readout is a single photodetector located at the antisymmetric port. However, it is possible to measure the light at two different phases (90 degrees apart) and subtract the results to get better averaging. As shown in section 2.0.5, there is a freedom to choose the readout scheme of the interferometer (heterodyne or homodyne) which will also affect the overall quantum sensitivity and introducing Fabry-Perot cavities will shape the shot noise for frequencies above the differential cavity pole in equations 2.31 and 2.41.

Seismic Noise

Reference:[Kissel Thesis] The main contributions to seismic noise are primarily caused by either natural occurrences (tectonic plates, wind driven microcosms, oceanic storms etc) or man-made disturbances (heavy automotive traffic, industrial machinery, etc) which contribute to the background hum of motion. In general, this will be the low frequency barrier for all terrestrial gravitational-wave detectors. One of the biggest upgrades from eLIGO to aLIGO was the increase in complexity for seismic isolation and suspensions. Using multiple stages of actively controlled platforms [52] [53] [54][3], the noise contribution can be attenuated for frequencies larger than 1Hz; in addition, the use of quadruple pendulums to hang the main arm cavity optics further reduces the motion above the pendulum's resonance frequency[24][8]. This is a tremendous upgrade from the mostly passive isolation methods used in initial LIGO. An interesting point to note is that the estimate of noise contributions from seismic activities to the strain sensitivity is negligible for frequencies above 10 Hz, but absolutely vital for lock acquisition and resonator stability [77] [34].

Thermal Noise

Brownian motion [27] is the random movement of particles suspended in a fluid. The LIGO test masses that make up the 4 kilometer long Fabry-Perot cavities are large macroscopic objects but their constituent atoms can be excited by the ambient temperature which leads to random motion. Those atoms are interconnected which allow for the propagation of an infinite number of elastic wave modes that contain random relative phases and the linear superposition of the modes create distortions that result in thermal noise.

A good way to start analyzing thermal noise is to consider a simple harmonic oscillator with mass m ,

that is in a thermal bath with a damping force, $F = -b\dot{x}(t)$.

$$\ddot{x}(t) + \gamma\dot{x}(t) + \omega_0^2x(t) = F/m \quad (2.66)$$

Here, $\gamma = b/m$ and the force, F , can be described by white noise. In this case, the force represents work being done on the system by the external world whereas the damping factor is the release of the system's energy to the outside world. By taking the Fourier transform, the equation of motion becomes

$$\tilde{x}(f) = \frac{\tilde{F}(f)}{m} \frac{1}{\omega^2 + i\gamma\omega + \omega_0^2} \quad (2.67)$$

This implies that the spectral density for viscous damping is

$$S_{Vis} = \frac{S_F}{m^2} \frac{1}{(\omega^2 - \omega_0^2)^2 + (\gamma\omega)^2} \quad (2.68)$$

Because the noise is due to a thermal bath, the integrated power over all frequencies must satisfy this equation

$$\frac{1}{2} \int_{-\infty}^{\infty} S_{Vis}(\omega) \frac{d\omega}{2\pi} = \frac{k_B T}{m\omega_0^2} \quad (2.69)$$

where k_B is the familiar Boltzmann's constant and T is the ambient temperature. Solving the integral and plugging the result for S_F back into the equation 2.68 gives the power spectrum for viscous damping,

$$S_{Vis} = \frac{4k_B T \gamma}{m} \frac{1}{(\omega^2 - \omega_0^2)^2 + (\gamma\omega)^2} \quad (2.70)$$

This equation shows that for three different frequency regimes, the response can vary wildly.

$$\omega \ll \omega_0 \rightarrow S_{Vis} = \frac{4k_B T}{m Q \omega_0^3} \quad (2.71a)$$

$$\omega \approx \omega_0 \rightarrow S_{Vis} = \frac{4k_B T}{m \omega_0^3} Q \quad (2.71b)$$

$$\omega \gg \omega_0 \rightarrow S_{Vis} = \frac{4k_B T}{m Q} \frac{\omega_0}{\omega^4} \quad (2.71c)$$

where $Q = \omega_0/\gamma$ is commonly known as the quality factor of a resonator. Qualitatively, this is directly proportional to the resonance height and its thinness. Figure 2.12 shows the resultant frequency dependent amplitude spectral density for a few different quality factors, for higher Q systems the amount of noise contribution from thermal noise is reduced at frequencies above the resonance. Another commonly used

definition of the quality factor is the amount of energy loss per cycle, if the Q of a system is high, then the amount of energy loss per oscillation is very small and will take a longer time returning to equilibrium. A good description of the quality factor and its application to gravitational wave detectors can be found in section 7.5 of [63].

As system's mode number increases, the previous analysis becomes very difficult to solve analytically. However, the connection between a damped harmonic oscillator's energy loss and power spectrum can be described generically using the Fluctuation Dissipation Theorem,

$$S_x(f) = \frac{k_B T}{\pi^2 f^2} |\operatorname{Re}(Y(f))| \quad (2.72)$$

where $Y(f)$ is the complex mechanical admittance (inverse of the impedance) of a system. The physical interpretation of equation 2.72 can be viewed as a tunnel of energy between a system of interest and the outside world. If there is an ability to couple energy from one system to another via some process, then the reverse must be true as well. This subtle but powerful statement can be applied generally. For example, a resistor which is able to dissipate thermal energy when current is flowing through it will convert random external temperature fluctuations into stray currents that results in *Johnson Noise*. Another principle which the FD theorem relies upon is that when the system is in thermal equilibrium, its response to fluctuations will be the same as applying a small force randomly.

Using this method, the mechanical admittance of a system is defined as $Y(f) = \dot{x}(f)/F(f)$ which can be written down directly for a damped harmonic oscillator using equation 2.67,

$$\begin{aligned} \frac{\dot{x}(f)}{F} &= \frac{i\omega}{m} \frac{1}{\omega_0^2 - \omega^2 + i\gamma\omega} \\ &= \frac{i\omega}{m} \frac{(\omega_0^2 - \omega^2 - i\gamma\omega)}{(\omega_0^2 - \omega^2)^2 + (\gamma\omega)^2} \end{aligned} \quad (2.73)$$

and by plugging this into the fluctuation dissipation theorem, the power spectral density matches equation 2.70 for the viscous damping. To extend the usage further, consider the thermal noise from a solid which has some thermoelastic dissipation from an internal mode given by $F_{diss} = -k(1 + \phi_L)x(t)$ where the phase term comes from the lag between applied force and the system's response to said force. By solving Newton's second law with this new damping term, the displacement spectrum becomes

$$\tilde{x}(f) = \frac{\tilde{F}}{m} \frac{1}{(1 + i\phi_L)\omega_0^2 - \omega^2} \quad (2.74)$$

Unlike the previous example of viscous damping, the integral for thermoelastic dissipation only holds for

some frequency regime but implementing the fluctuation dissipation theorem leads directly to the noise power spectrum,

$$S_{TN}(f) = \frac{4k_B T \omega_0^2 \phi_L}{m\omega} \frac{1}{(\omega^2 - \omega_0^2)^2 + (\omega_0 \phi_L)^2} \quad (2.75)$$

The frequency response will also be different compared to viscoelastic dissipation,

$$\omega \ll \omega_0 \rightarrow S_{vis} = \frac{4k_B T}{mQ\omega\omega_0^2} \quad (2.76a)$$

$$\omega \approx \omega_0 \rightarrow S_{vis} = \frac{4k_B T}{m\omega_0^3} Q \quad (2.76b)$$

$$\omega \gg \omega_0 \rightarrow S_{vis} = \frac{4k_B T}{mQ} \frac{\omega_0^2}{\omega^5} \quad (2.76c)$$

The structural damping formalism can also be applied to the suspension fibers which hold the 40 kilogram test masses [38], [63] which yield a noise spectral density that contains resonances at a variety of frequencies. In Advanced LIGO, the violin modes and their harmonics could get rung up from earthquakes and saturate the output mode cleaner's DC photodiodes so they must be actively damped in order to obtain nominal low noise.

The largest contribution to the total thermal noise for current interferometers do not stem from viscous damping [65], thermoelastic damping of the substrate [63], or internal friction of the suspension fibers. The most dominant type of thermal noise is from the mechanical loss of the dielectric coatings [40] [30] which cause phase noise at the high reflectivity surface of the mirrors.

Newtonian Noise

Described in the previous sections are noise sources which can be reduced using increasingly complicated techniques such as increased isolation stages for seismic or using squeezed states of light for quantum noise. However, for Newtonian noise caused by fluctuating gravitational fields from the wave motion of the ground [64] and [44] is one that cannot easily be reduced but possibly be measured and fed-forward or subtracted off-line [25].

2.1 Mode Matching with Squeezed States of Light

In Section 2.0.6, the quantum limited sensitivity for a Michelson interferometer was shown to be composed of shot noise and radiation pressure. Although quantum fluctuations are a fundamental noise source, their effects can be modified by manipulating the vacuum state with correlated photons and injecting these states

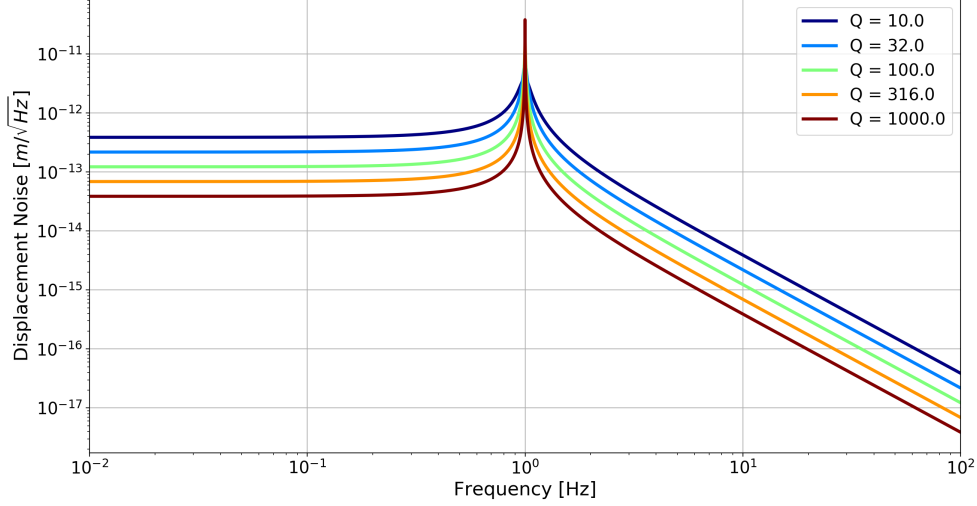


Figure 2.12: **Displacement spectrum for thermal noise.** By varying the resonance width of a system, the thermal noise at frequencies above the resonant peak will be decreased for higher Q's.

of light into the antisymmetric port of the interferometer. Within the LIGO community, this procedure of modifying quantum vacuum is called squeezing. The production of squeezed states with nonlinear devices is a well understood subject and was successfully tested in the sixth LIGO science run [20][21]. An extension of the formalism described in Section 2.0.6 was developed by Caves-Schumaker [16] which describes two-photon quantum optics and squeezing, but it is outside of the scope in terms of mode matching.

However, it is useful to understand the quantum noise in a way which scales the interferometer sensitivity in terms of the *Standard Quantum Limit* (SQL). The radiation pressure and shot noise add in quadrature to form the quantum noise and both are proportional to the square root of the input power but in different regimes. The SQL refers to the input power minimizes the total quantum noise and is the minimum achievable noise without squeezing. The radiation-pressure back-action coupling constant, κ , is given by [48]

$$\kappa = \frac{4P_0\omega_0}{mc^2f^2} \quad (2.77)$$

where P_0 is the input power on the beamsplitter, ω_0 is the laser angular frequency, m is the optic mass, and f is the Fourier domain frequency. The SQL for a simple Michelson is given by [48],

$$S_{SQL} = \frac{4\hbar}{mL^2f^2} \quad (2.78)$$

With these two equations above, the total single-sided power spectral density for a simple Michelson is

$$S_{SM} = \frac{S_{SQL}}{2} \left(\frac{1}{\kappa} + \kappa \right) \quad (2.79)$$

Here the first term is represents the shot noise while the second term is the radiation pressure contribution.

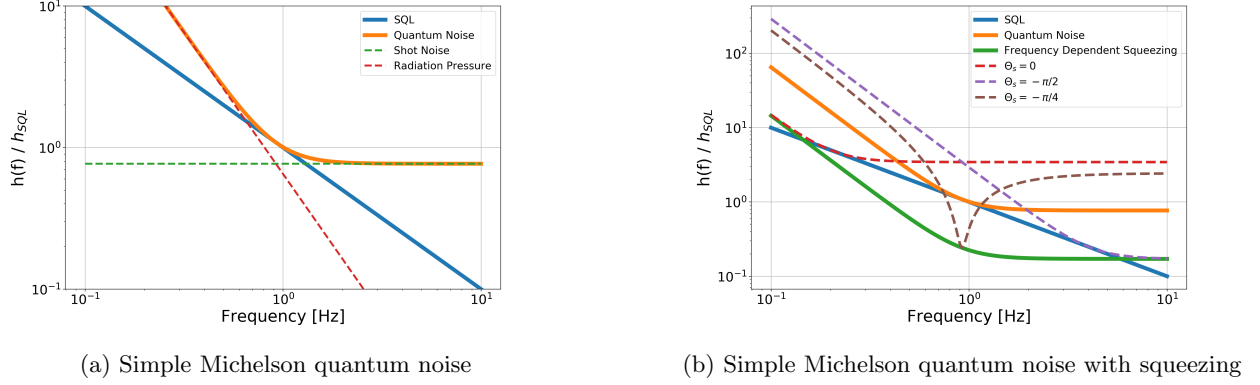
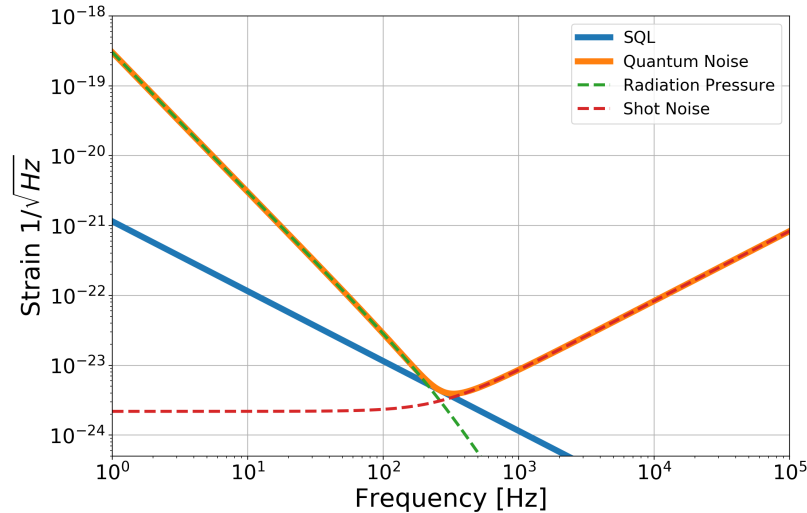


Figure 2.13: The amplitude spectral density of gravitational wave strain normalized by the standard quantum limit.

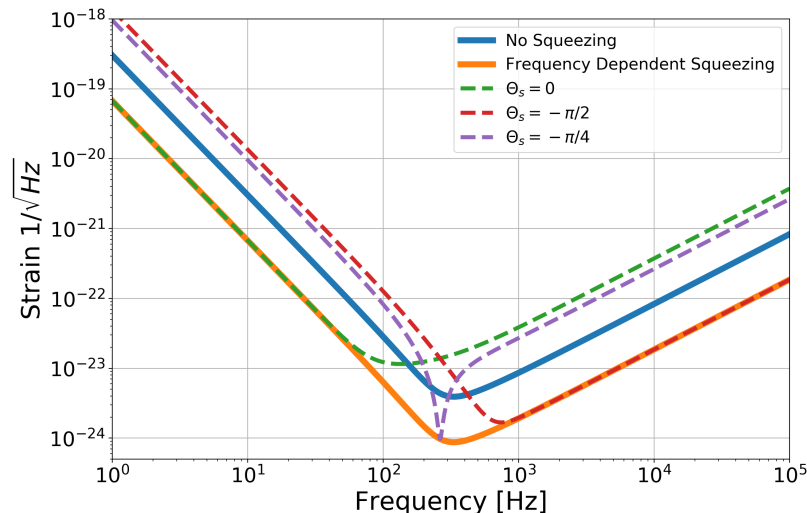
Modifying the field entering the antisymmetric port by replacing the quantum vacuum with a squeezed state has interesting effects on the strain sensitivity and reduces the noise floor below the standard quantum limit. The power spectral density for a simple Michelson with injected squeezing is described by [48]

$$\begin{aligned} S_{SMSqz} &= \frac{S_{SQL}}{2} \left(\frac{1}{\kappa} + \kappa \right) [\cosh 2R - \cos(2(\phi_s + \theta_s)) \sinh 2R] \\ &= \frac{S_{SQL}}{2} \left(\frac{1}{\kappa} + \kappa \right) e^{-2R} \quad \text{for } \theta_s = -\phi_s \end{aligned} \quad (2.80)$$

where R is the squeeze factor, θ_s is the squeeze angle, and $\phi_s = \cot^{-1}(\kappa)$. The squeeze angle can change the regime of strain which is affected, for example, when injecting for optimal shot noise reduction one would choose $\theta_s = \pi/2$. However, when trying to reduce the radiation pressure noise, then choosing $\theta_s = 0$ is optimal. For the second line in the equation above, to achieve broadband squeezing, the squeeze angle must be rotated as a function of frequency. Fortunately, this can be achieved by reflecting the squeezer beam off a filter cavity before injecting into the interferometer [57] [31].



(a) Power recycled Fabry Perot Michelson quantum noise



(b) Power recycled Fabry Perot Michelson quantum noise with various squeezing angles

Figure 2.14: Add a caption

Chapter 3

The Fundamentals of Mode-Matching

The plane wave and the spherical wave represent the two extremes of transverse spatial confinement. The former is a collimated beam that has one steady wavefront whose normal vector is parallel with the axis of propagation, whereas the latter type of wave has a single point of origin and its normal rays diverge in all directions. There exists a solution which is a medium between the two cases called a Gaussian beam. When dealing with length sensing degrees of freedoms such as section 2.0.2, the simple plane wave approximation is sufficient in describing the dynamics, however, when trying to understand the misalignment and mode-mismatch signals, it is necessary to incorporate Gaussian beams and associated their higher order modes.

3.1 Gaussian Beam Optics

Consider the famous Maxwell's equations:

$$\begin{aligned}\nabla \times \mathbf{E} &= -\frac{\partial \mathbf{B}}{\partial t} \\ \nabla \cdot \mathbf{B} &= 0 \\ \nabla \times \mathbf{B} &= \mu \mathbf{J} + \frac{1}{c^2} \frac{\partial \mathbf{E}}{\partial t} \\ \nabla \cdot \mathbf{E} &= \frac{\rho}{\epsilon}\end{aligned}\tag{3.1}$$

Concentrating on the electric field in vacuum, we arrive at the Helmholtz Equation

$$(\nabla^2 + k^2)\mathbf{U}(\mathbf{r}, t) = 0\tag{3.2}$$

where $k = \frac{2\pi\nu}{c}$ is the wave number and $\mathbf{U}(\mathbf{r}, t)$ is the complex amplitude which can describe either the

electric or magnetic fields. There are a variety of solutions to equation 3.2 which include the plane and spherical waves [62]. These two types of solutions are the extremes when considering the angle and spatial distribution as a function of propagation. The plane wave which has been used in chapter 1 is a beam whose rays have no variance in the spatial direction as it propagates through space, whereas the spherical wave starts at a point and spreads as a function of distance from the origin. Somewhere in between these two extrema is the paraxial wave which is a wave pattern that has its rays at small angles relative to the direction of propagation (see Figure[raysoflight]). It is possible to express the paraxial solution to equation 3.2 as a plane wave with a modulated complex envelope $\mathbf{A}(r)$

$$\mathbf{U}(\mathbf{r}) = \mathbf{A}(\mathbf{r})e^{-ikz} \quad (3.3)$$

However, in order for the paraxial wave to exist, $\mathbf{U}(r)$ must satisfy the Helmholtz equation or alternatively, the complex amplitude portion must satisfy a separate differential equation known as the paraxial Helmholtz Equation. By imposing the constraints which force the envelope to vary slowly with respect to the z-axis within the distance of one wavelength $\lambda = 2\pi/k$,

$$\left| \frac{\partial^2 \mathbf{A}}{\partial z^2} \right| \ll \left| k \frac{\partial \mathbf{A}}{\partial z} \right| \quad (3.4a)$$

$$\left| \frac{\partial^2 \mathbf{A}}{\partial z^2} \right| \ll \left| k \frac{\partial^2 \mathbf{A}}{\partial x^2} \right| \quad (3.4b)$$

$$\left| \frac{\partial^2 \mathbf{A}}{\partial z^2} \right| \ll \left| k \frac{\partial^2 \mathbf{A}}{\partial y^2} \right| \quad (3.4c)$$

the partial differential equation which arises is called the Paraxial Helmholtz Equation:

$$\nabla_T^2 A(r) - i2k \frac{\partial A(r)}{\partial z} = 0 \quad (3.5)$$

where $\nabla_T^2 = \frac{\partial^2}{\partial x^2} + \frac{\partial^2}{\partial y^2}$ is the transverse Laplacian. A simple solution for equation 3.5 is the complex paraboloidal wave

$$A(\mathbf{r}) = \frac{A_0}{q(z)} e^{\frac{-ikr^2}{2q(z)}}, \quad q(z) = z + iz_0 \quad (3.6)$$

where z_0 is the Rayleigh range and is directly proportional to the square of the waist size. In order to separate the amplitude and phase portions of the wave, it is useful to rewrite $q(z)$ as

$$\frac{1}{q(z)} = \frac{1}{R(z)} - i \frac{\lambda}{\pi W^2(z)} \quad (3.7)$$

Plugging equation 3.7 into 3.6 leads directly to the complex amplitude for a Gaussian Beam

$$U(r, z) = A_0 \frac{W_0}{W(z)} e^{-\frac{r^2}{W^2(z)}} e^{-ikz - ik \frac{r^2}{2R(z)} + i\phi(z)} \quad (3.8)$$

where

$$W(z) = W_0 \sqrt{1 + \left(\frac{z}{z_0}\right)^2} \quad (3.9a)$$

$$R(z) = z \left[1 + \left(\frac{z}{z_0} \right)^2 \right] \quad (3.9b)$$

$$\phi(z) = \tan^{-1} \left(\frac{z_0}{z} \right) \quad (3.9c)$$

$$W_0 = \sqrt{\frac{\lambda z_0}{\pi}} \quad (3.9d)$$

The Gaussian beams are named as such because of the intensity distribution,

$$I(r, z) = |U(r, z)|^2 = I_0 \left[\frac{w_0}{w(z)} \right]^2 \exp \left[\frac{-2r^2}{w^2(z)} \right] \quad (3.10)$$

where $I_0 = |A_0|^2$ and has a peak at $r = 0$ and $z = 0$. The width increases as the beam propagates along the \hat{z} axis away from the waist position and the intensity maximum on the beam axis decreases (see Figure 3.3),

$$I(0, z) = \frac{I_0}{1 + (z/z_0)^2} \quad (3.11)$$

When it comes to sensing a laser beam, the most common way is using a photodetector which is a transducer that transforms the integrated intensity or power into an electronic current.

Gouy Phase

The Gouy phase given by equation 3.9c is the phase lag between a Gaussian beam and a perfect plane wave that occurs as a function of propagation along the \hat{z} -axis which ranges from $\phi(z) = \pm\pi/2$ for $z = \pm\infty$. Physically, this could be interpreted as the difference between the laser beam behaving like a plane wave when $z \approx 0$ (or near field) and eventually evolving into a spherical wave when $z \approx \pm\infty$ (or far field) (see Figure 3.2). Although this phenomenon is interesting mathematically, most texts do not consider how to practically use or measure the Gouy phase. In LIGO technical notes and electronic logs, the Gouy phase of sensors or actuators are used to describe where along the beam path the piece of equipment is located. This will indicate what degree of freedom is being observed or adjusted. For example, in ray optics [62] a laser beam has two degrees of freedom, the displacement and angle from the optical axis. If an actuator such as

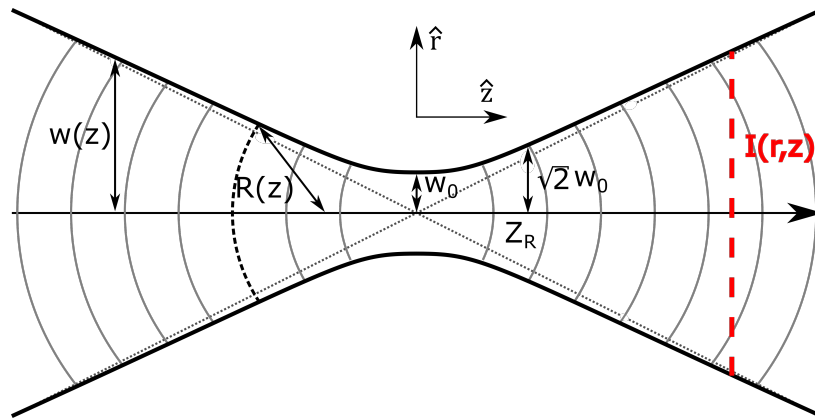


Figure 3.1: **A depiction of the Gaussian beam properties with respect to cylindrical coordinates.** Because the beam is axially symmetric, the two coordinates are denoted by \hat{r} for the radial and \hat{z} for the axis of propagation with the origin located at the center. The thick dark lines represent the beam size, $w(z)$, which is minimal at the waist, $w(z) = w_0$ when $z = 0$ and asymptotic towards $\lambda/\pi w_0$ when $z \approx \infty$ as shown by the dotted gray lines. The red dashed line represents the intensity cross section of the beam which changes to a wider and flatter profile as a function of distance from the waist.

a piezo-electric transducer with an attached reflective mirror is placed near the origin or focus of the laser beam, then the controlled degree of freedom is only the angle. Alternatively, if the actuator is placed in the far field then the controlled degree of freedom is almost entirely displacement. This is also true of sensors at various points along the \hat{z} -axis to determine the exact alignment of the optical beam.

In practice, it is impossible to sense the true waist of an optical system because it could be inside a Fabry-Perot cavity. So the clever designer must insert a pick-off beam to sample the transmission or reflection of the interested optical system and use a combination of lenses to create a telescope for the sensors and infers the degrees of freedom. Then, by rotating to the two-dimensional space created by the sensors to represent the interested space spanned by the optical system's degrees of freedom; colloquially, this is known as a sensing matrix. Using this method, sensors do not have to be exactly at the near or far field because it is only required that the two sensors are separated by $\pi/2$ in Gouy phase, in fact, it is usually easier to place one sensor at $+\pi/4$ and the other at $-\pi/4$.

Unfortunately, there is no transducer that directly measures the Gouy phase so in order to *determine* the Gouy phase of a particular sensor or actuator, one must model the beam propagation and fit the waist location.

Hermite-Gauss Modes

The fundamental Gaussian beam is not the only solution which can be used to solve equation 3.5. In fact, there exists a complete set of solutions that can solve the paraxial Helmholtz Equation in rectangular

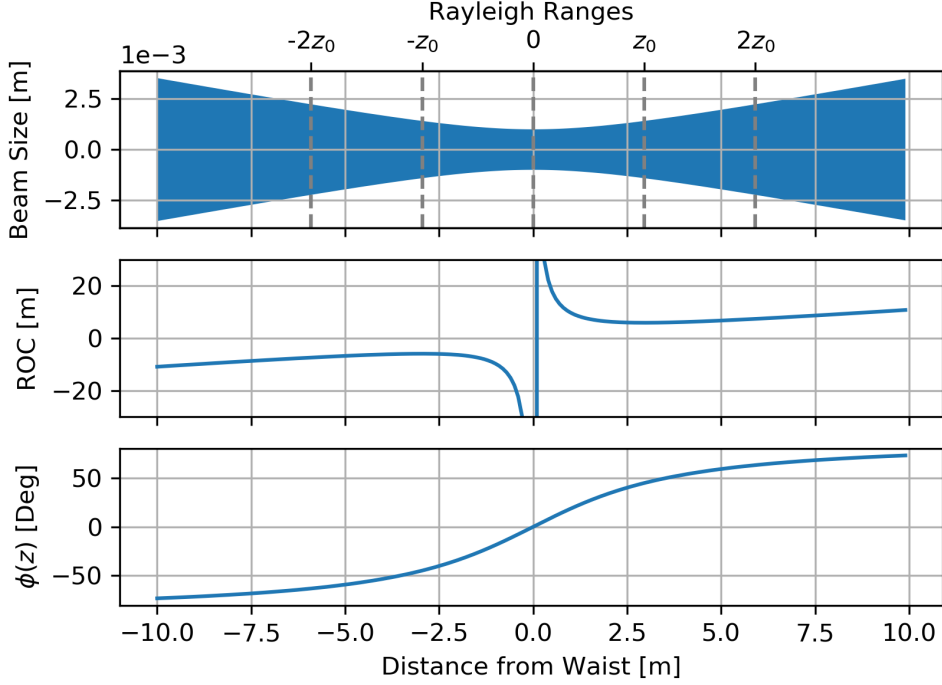


Figure 3.2: Beam size, radius of curvature, and Gouy phase as a function of distance propagation from the waist. The vertical dashed gray lines represent the integer number of Rayleigh ranges. At the point $z = z_0$, the beam size is $\sqrt{2}$ of the waist size and the radius of curvature is minimal. At this point, the Gouy phase propagation is lagging the plane wave by $\pi/4$ and the beam intensity is half of that at the waist.

coordinates, which are referred to as the Hermite Gauss modes

$$U_{mn}(x, y, z) = A_{mn} \left[\frac{W_0}{W(z)} \right] \mathbb{G}_m \left(\frac{\sqrt{2}x}{W(z)} \right) \mathbb{G}_n \left(\frac{\sqrt{2}y}{W(z)} \right) \times \exp \left\{ -ikz - \frac{ik(x^2 + y^2)}{2R(z)} + i(m+n+1)\phi(z) \right\} \quad (3.12)$$

where,

$$\mathbb{G}(u) = \mathbb{H}(u) \exp(-u^2/2) \quad (3.13)$$

and $\mathbb{H}(u)$ are the well known Hermite polynomials. It is important to mention that the Gouy phase of the complex amplitude is different than the fundamental Gaussian beam by a factor of $(m+n+1)$ and that the intensity distribution of these higher order modes are much different. Both of these facts will become extremely important in the following wavefront sensing discussion.

The extra Gouy phase that a higher order mode accrues as a function of z shows up as in the frequency or cavity length domain as one sweeps through a full free spectral range using an offset in the length or frequency error signal. This can be directly used to measure the higher order mode separation and becomes important

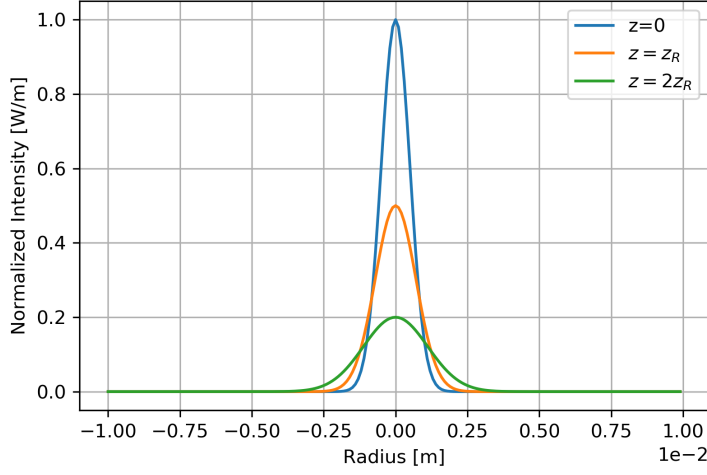


Figure 3.3: Intensity

if the cavity has a low finesse which means the fundamental Gaussian mode has a spread comparable in frequency to the first order mode then it is easy to hop from one to the other.

Laguerre Modes

Another complete set of alternative solutions to equation 3.5 exists which are called the Laguerre-Gauss modes

$$V_{\mu\nu}(\rho, \theta, z) = A_{\mu\nu} \left[\frac{W_0}{W(z)} \right] \mathbb{L}_\nu^\mu \left(\frac{\sqrt{2}x}{W(z)} \right) \times \exp \left\{ -ikz - \frac{ik\rho^2}{2R(z)} + i(\mu + 2\nu + 1)\phi(z) \right\} \quad (3.14)$$

where $\mathbb{L}_\nu^\mu \left(\frac{\sqrt{2}x}{W(z)} \right)$ is the Laguerre polynomial function. Both equations 3.12 and 3.14 are able to fully describe any complex electromagnetic amplitude; and because they both form complete sets, there is a rotation which can map from one basis to the other [6] [59]

$$U_{\mu\nu}^{LG}(x, y, z) = \sum_k^N i^k b(n, m, k) U_{N-k, k}^{HG}(x, y, z) \quad (3.15)$$

where

$$b(n, m, k) = \sqrt{\left(\frac{(N-k)!k!}{2^N n! m!} \right)} \frac{1}{k!} \frac{d^k}{dt^k} [(1-t)^m (1+t)^m]|_{t=0} \quad (3.16)$$

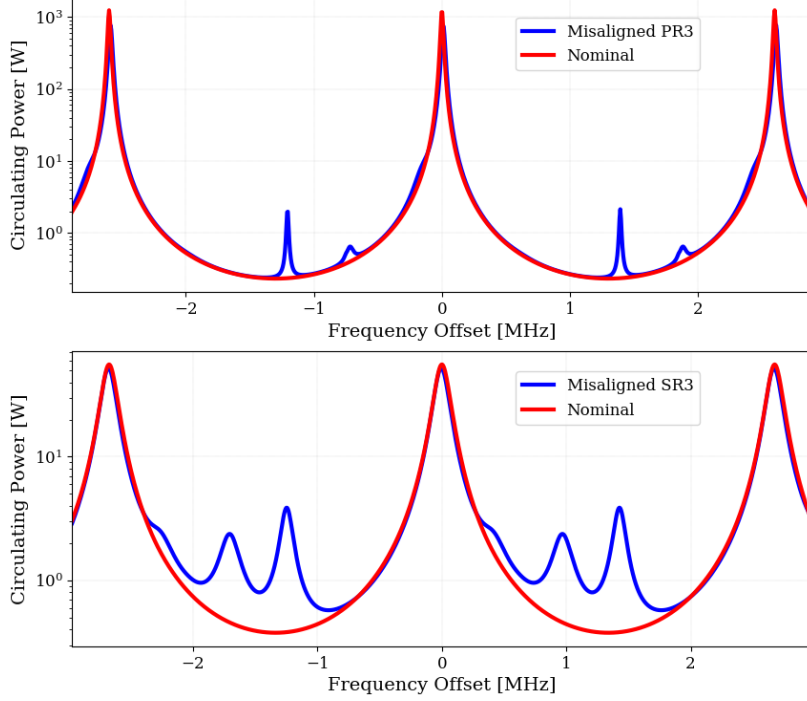


Figure 3.4: A Finesse model of a longitudinal mode scan comparing the Advanced LIGO power recycling and signal recycling cavities The upper and lower plots represent the PRC and SRC, respectively. The main difference between these two optical cavities is obvious when comparing the three large peaks corresponding to the 00 mode resonances. The power recycling cavity has a much higher and sharper peak which indicates higher finesse whereas the signal recycling cavity is a much lower finesse which has a broader and shorter peak. The red traces are with nominal alignment whereas the blue lines correspond to misalignments of PR3 and SR3 by $1\mu\text{rad}$ which allow higher order mode content to resonate as a function of length.

3.1.1 Misalignment and Higher Order Modes

Morrison and Anderson [5] [55] derived a simplistic way of how small misalignments and mode mismatch in cavities can couple the fundamental Gaussian beam into various higher order modes. This is done by taking a linear cavity and using its perfectly matched Gaussian beam as a reference, and then varying the input electric field with small perturbations and expanding in terms of the higher order modes. So long as the mismatches are small, it is possible to consider only the first few terms of the expansion which have gained most of their power from the fundamental mode.

Consider the first three Hermite-Gauss modes of equation 3.12 in one dimension and normalized to set the total optical power to unity:

$$\begin{aligned}
U_0(r) &= \left(\frac{2}{\pi w^2(z)} \right)^{1/4} e^{-r^2/w^2(z)} \\
U_1(r) &= \left(\frac{2}{\pi w^2(z)} \right)^{1/4} \frac{2r}{w(z)} e^{-r^2/w^2(z)}, \\
U_2(r) &= \left(\frac{2}{\pi w^2(z)} \right)^{1/4} \frac{1}{\sqrt{2}} \left(\frac{4r^2}{w^2(z)} - 1 \right) e^{-r^2/w^2(z)}
\end{aligned} \tag{3.17}$$

Beam Axis Tilted

If the input beam into an optical cavity is tilted by an angle α with respect to the nominal cavity axis, the wave front of the input beam will have an extra phase propagation relative to the cavity that is approximately proportional to $e^{ik\alpha r}$. By implementing the small angle approximation, which is valid if the misalignment is much smaller than the divergence angle of the fundamental mode $k\alpha r \ll 1$, the resultant input beam is

$$\Psi \approx U_0(r)e^{ik\alpha r} \approx U_0(r)(1 + ik\alpha r) = U_0(r) + \frac{ik\alpha w(z)}{\sqrt{2\pi}} U_1(r) \tag{3.18}$$

Here the factor associated with the first higher order mode is complex, indicating there is a 90 degree phase difference between the fundamental and off axis mode.

Beam Axis Displaced

If the input beam is displaced in the transverse direction by a quantity Δr , the resultant waveform will be

$$\begin{aligned}
\Psi &= U_0(r + \Delta r) \\
&= \left(\frac{2}{\pi w^2(z)} \right)^{1/4} e^{-(r+\Delta r)^2/w^2(z)} \\
&= \left(\frac{2}{\pi w^2(z)} \right)^{1/4} e^{-(r^2+2r\Delta r+\Delta r^2)/w^2(z)} \\
&\approx \left(\frac{2}{\pi w^2(z)} \right)^{1/4} e^{-r^2/w^2(z)} e^{-2r\Delta r/w^2(z)} \\
&\approx \left(\frac{2}{\pi w^2(z)} \right)^{1/4} e^{-r^2/w^2(z)} \left(1 - \frac{2r\Delta r}{w^2(z)} \right) \\
&= \left(U_0(r) - \sqrt{\frac{2}{\pi}} \frac{\Delta r}{w(z)} U_1(r) \right)
\end{aligned} \tag{3.19}$$

Similarly to a tilted input beam axis, the displaced beam axis couples power to the first higher order mode, however, the latter does not have a 90 degree phase difference previously seen in the former. This point is of extreme importance when trying to discern between the two effects as shown in Section [3.3]. Although comparing the two cases in Figure, one can already see the difference between the wavefronts in the near field, $z \ll z_R$, and the far field, $z \gg z_R$.

In the near field, there is no phase difference due to a displaced beam, but there is one for a tilted beam. Conversely, in the far field, there is no phase difference due to a tilted beam, but there is one from a displaced beam. In order to implement a closed loop feedback system, the wavefront sensors discussed in Section 3.2 will use this precise logic to extract an error signal.

3.1.2 Mode Mismatch and Higher Order Modes

Waist Size Shifted

By considering the effect of evaluating the fundamental mode at the waist position, $z = 0$, but changing the waist size by a small amount ϵ , it is possible to see coupling into higher order modes by expanding to first order.

$$\begin{aligned}
 \Psi &= U_0(r, w(z) = w_0/(1 + \epsilon)) \\
 &= \left(\frac{2}{\pi w_0^2} \right)^{1/4} \sqrt{1 + \epsilon} \quad e^{-r^2(1+\epsilon)^2/w_0^2} \\
 &\approx \left(\frac{2}{\pi w_0^2} \right)^{1/4} (1 + \epsilon/2) \quad e^{-r^2/w_0^2} \quad e^{-2r^2\epsilon/w_0^2} \\
 &\approx \left(\frac{2}{\pi w_0^2} \right)^{1/4} (1 + \epsilon/2) \quad e^{-r^2/w_0^2} \quad (1 - 2r^2\epsilon/w_0^2) \\
 &\approx \left(\frac{2}{\pi w_0^2} \right)^{1/4} \left(1 + 2\epsilon \left(\frac{1}{4} - \frac{r^2}{w_0^2} \right) \right) \quad e^{-r^2/w_0^2} \\
 &= U_0(r) - \frac{\epsilon}{\sqrt{2}} U_2(r)
 \end{aligned} \tag{3.20}$$

Changing the waist size by a small amount will couple the fundamental mode to the in-phase second order Hermite Gauss mode.

Waist Position Shifted

To repeat the process from above with a waist position shift, it is useful to start with a more general equation that includes the phase that is gained from including the radius of curvature,

$$\Psi = \left(\frac{2}{\pi w^2(z)} \right)^{1/4} \quad e^{-r^2/w^2(z)} \quad e^{-ikr^2/2R(z)} \tag{3.21}$$

where $R(z)$ is from equation 3.9b. It is also useful to approximate the shift in waist position along the longitudinal axis is small compared to the Rayleigh range of the beam, $\Delta z \ll z_0$, which leaves the waist

size approximately the same and the radius of curvature inversely proportional to the shift.

$$w^2(\Delta z) = w_0^2 \left[1 + \left(\frac{\Delta z}{z_0} \right)^2 \right] \approx w_0^2 \quad (3.22a)$$

$$R(\Delta z) = \Delta z \left(1 + \left(\frac{z_0}{\Delta z} \right)^2 \right) \approx \frac{z_0^2}{\Delta z} \quad (3.22b)$$

Plugging the equations above into 3.21,

$$\begin{aligned} \Psi &\approx \left(\frac{2}{\pi w_0^2} \right)^{1/4} e^{-r^2/w_0^2} e^{-ikr^2 \Delta z / 2z_0^2} \\ &\approx \left(\frac{2}{\pi w_0^2} \right)^{1/4} e^{-r^2/w_0^2} \left(1 - \frac{ikr^2 \Delta z}{2z_0^2} \right) \\ &= U_0(r) - \left(\frac{2}{\pi w_0^2} \right)^{1/4} e^{-r^2/w_0^2} \frac{ikr^2 \Delta z}{2z_0^2} \\ &= U_0(r) - i \frac{\Delta z}{2kw_0^2} \left(4U_2(r) + U_0(r) \right) \end{aligned} \quad (3.23)$$

The equations above show that a fundamental Gaussian mode that is shifted in waist position will couple power to the second order Hermite Gauss mode. Although changes in the waist size or position couple power to the same mode, they differ by a 90 degrees in phase as denoted by the extra factor of i in the coupling coefficient. By recognizing the two effects are in different quadrature phases will allow a user to design a system to distinguish between the different types of physical couplings, this is shown in Section 3.2.

In order to be physically valid one would need to consider the full two dimensional space so that the equation would encapsulate the full transverse mode, however, the x and y components would follow the exact same derivation. On that point, it is important to note that only the mode mismatch couplings from either a varying waist position or size has higher order modes that are circularly symmetric.

3.2 Wavefront Sensing

Heterodyne detection via modal decomposition of the full electric field allows the use of wavefront sensors to extract an error signal from the optical system. Hefetz et.al [41] created a formalism to describe the use of wavefront sensors by creating frequency sidebands which accumulate a different Gouy phase than the electric field at the carrier frequency when passed through the optical system. By observing the demodulated signal of the intensity, it is possible to obtain a linear signal that corresponds to a physical misalignment or mode mismatch.

Fundamentally, the purpose of wavefront sensing is to detect the content of higher order modes due

to physical disturbances of the optical cavity (ie. mode mismatch or misalignment). In other words, it is examining the difference between the incoming beam's and the cavity's eigenmodes.

Consider a general equation for an electric field which is a linear combination of all higher order modes of the complex amplitude

$$E(x, y, z) = \sum_{m,n}^{\infty} a_{mn} U_{mn}(x, y, z) \quad (3.24)$$

where $U_{mn}(x, y, z)$ are the eigenmodes described in equation 3.12 (or 3.14) and a_{mn} is the complex amplitude. It is also convenient in the following analysis to use vectors when describing the composition of the electric fields.

$$|E(x, y, z)\rangle = \begin{pmatrix} E_{00} \\ E_{01} \\ E_{10} \\ E_{20} \\ E_{02} \end{pmatrix} \quad (3.25)$$

When creating a theory that involves laser beams, it is useful to define operators that are important in describing physical situations. For example, laser beams propagate through space and pick up phase according to equation 3.12 which can be represented by the spatial propagation operator,

$$\hat{P}_{mn,kl} = \delta_{mn}\delta_{kl} \exp[-ik(z_2 - z_1)]\exp[i(m + n + 1)\phi(z)] \quad (3.26)$$

However, it is useful to compare how the fundamental Gaussian mode propagates compared to the higher order modes,

$$\hat{\eta}_{\mu\nu} = \begin{pmatrix} e^{i\phi} & 0 & 0 & 0 & 0 \\ 0 & e^{2i\phi} & 0 & 0 & 0 \\ 0 & 0 & e^{2i\phi} & 0 & 0 \\ 0 & 0 & 0 & e^{3i\phi} & 0 \\ 0 & 0 & 0 & 0 & e^{3i\phi} \end{pmatrix} \quad (3.27)$$

From the above diagonal elements, it is clear that the higher order modes have an extra phase compared to the fundamental 00 mode, this effect will be extremely important on how an error signal can be derived from the optical system.

$$|E(x, y, z_2)\rangle = \hat{M}(x, y, z_1, z_2) |E(x, y, z_1)\rangle \quad (3.28)$$

where $\hat{M}(x, y, z_1, z_2)$ is the misalignment operator. Since we are using the paraxial approximation, the z-components of the misalignment operator are small so we can approximate $\hat{M}(x, y, z_1, z_2) \approx \hat{M}(x, y)$ and the expectation value is

$$M_{mn,kl} = \langle U_{mn}(x, y, z_1) | M(x, y) | U_{kl}(x, y, z_2) \rangle \quad (3.29)$$

where the product is an integral over the transverse space $\iint_{D(x,y)} dx dy$

$$\hat{\Theta}_{\mu\nu} = \begin{pmatrix} 1 & 2i\theta_x & 2i\theta_y & 0 & 0 \\ 2i\theta_x & 1 & 0 & 0 & 0 \\ 2i\theta_y & 0 & 1 & 0 & 0 \\ 0 & 0 & 0 & 1 & 0 \\ 0 & 0 & 0 & 0 & 1 \end{pmatrix} \quad (3.30)$$

$$\hat{\mathbb{D}}_{\mu\nu} = \begin{pmatrix} 1 & \alpha_x/\omega_0 & \alpha_y/\omega_0 & 0 & 0 \\ \alpha_x/\omega_0 & 1 & 0 & 0 & 0 \\ \alpha_y/\omega_0 & 0 & 1 & 0 & 0 \\ 0 & 0 & 0 & 1 & 0 \\ 0 & 0 & 0 & 0 & 1 \end{pmatrix} \quad (3.31)$$

$$\hat{\mathbb{Z}}_{\mu\nu} = \begin{pmatrix} 1 & 0 & 0 & \Delta z_x & \Delta z_y \\ 0 & 1 & 0 & 0 & 0 \\ 0 & 0 & 1 & 0 & 0 \\ \Delta z_x & 0 & 0 & 1 & 0 \\ \Delta z_y & 0 & 0 & 0 & 1 \end{pmatrix} \quad (3.32)$$

where $\Delta z_{(x,y)} = \frac{i}{\sqrt{2}} \frac{\lambda b}{2\pi\omega_0}$

$$\hat{\mathbb{Z}}_{0,\mu\nu} = \begin{pmatrix} 1 & 0 & 0 & \Delta z_{0,x} & \Delta z_{0,y} \\ 0 & 1 & 0 & 0 & 0 \\ 0 & 0 & 1 & 0 & 0 \\ \Delta z_{0,x} & 0 & 0 & 1 & 0 \\ \Delta z_{0,y} & 0 & 0 & 0 & 1 \end{pmatrix} \quad (3.33)$$

where $\Delta z_{0,(x,y)} = \frac{1}{\sqrt{2}} \frac{\omega' - \omega_0}{\omega_0}$

Figure: Beat frequency between two modes.

Chapter 4

Simulating Mode-Matching with Finesse

As with most simple concepts Within LIGO, the complexity scales very rapidly in application to the main interferometer and mode matching is no exception so it is useful to use a full scale simulation to extract as much information as possible.

Mode matching a linear cavity which has a single waist size and location relative to the input beam equates to two degrees of freedom. There is an arbitrary method where one could match the optical cavity with the input beam using heaters on the test mass or one could have deformable lenses which shape the incoming beam; this picture works for cavities which feed one Gaussian mode into the another such as the input (or output) mode cleaner.

4.1 How it works

[58] Summary of how Finesse works (input output matrix), how it handles HOMs

4.2 Finesse Simulations

4.2.1 ALIGO Design with FC and Squeezer

4.2.2 Looking at just Modal Change

4.2.3 QM Limited Sensitivity

4.3 Results

* Signal recycling cavity mismatches

* Mismatches before the OMC

* Mismatch contour graph: Comparing all of ALIGO cavities

* Optical Spring pops up at 7.4 Hz in the Signal-to-Darm TF, re-run with varying SRM Trans which should.

Chapter 5

Experimental Mode Matching

Cavities at Syracuse

In conjunction with Sandoval et al, the adaptive mode matching experiment was able to show the feasibility of a fully dynamical system.

5.1 Adaptive Mode Matching

Adaptive controls require both actuators and sensors which are interfaced in a real-time system that uses analog-to-digital (ADC) and digital-to-analog (DAC) converters. LIGO uses a front end computer that reads in data and processes the signals based off a Simulink graphical model that allows for simple logic, mathematical operations, and frequency dependent filtering. The real time data acquisition code is user-interfaced with a Motif Editor and Display Manager (MEDM) that is able to report and execute variables such as gains and matrix elements.

5.2 Actuators

5.2.1 Thermal Lenses

Fabian's work and UFL paper.

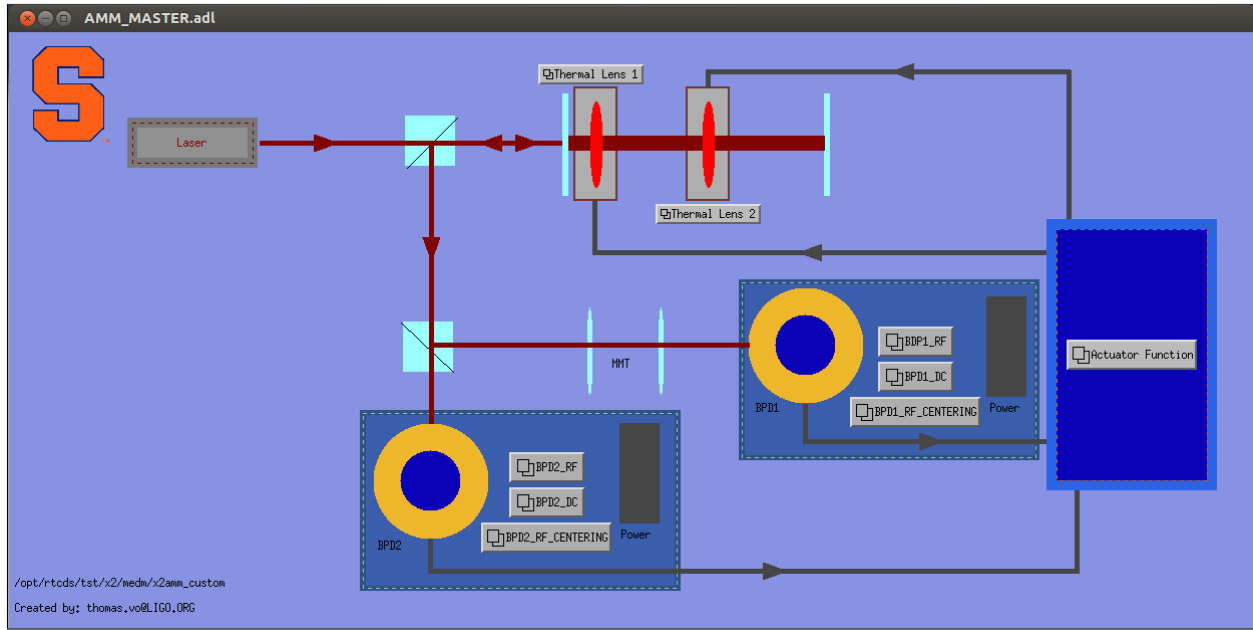


Figure 5.1: [MEDM master screen for adaptive mode matching at Syracuse] Here, the demodulated error signal in reflection of the Fabry-Perot cavity is fed into two RF detectors that have rotational phasing. Then the signal is sent to an actuator function which allows for diagonalizing the signals and can be sent to a set of thermal lens at different Gouy phases for actuation.

5.2.2 Translation Stages

5.3 Sensors

Recall in Section 3.2 that the RF modal decomposition technique relies on comparing the Gouy phase of the higher order modes to the fundamental Gaussian mode using an array of RF photodiodes to extract an error signal. The complication arises when using this method to extract the beat note between the fundamental mode and symmetric donut mode because the photodetector arrays must match the higher order mode geometry. This is easier to deal with when trying to sense angular distortions from a misaligned cavity because the 01 and 10 modes can be sensed with a split photodetector, however, using that a quadrant photodiode will not work to sense mode mismatch due to the cylindrical symmetry of the 02 and 20 modes. To date, Advanced LIGO uses no RF sensors to detect mode matching so the next sections will provide sensing methods which can be used for dynamic closed loop feedback control.

5.3.1 Bullseye Photodiodes (BPD)

It is clear that using a quadrant photodetector to measure the symmetric $U_{20} + U_{02}$ mode which arises from mismatch is futile because the integrated power on each side will be exactly the same due to donut mode

symmetry. So it is simplest to try subtracting the inner beam power from the outer ring of the electric field in order to measure a phase difference using a specialized RF photodiode called a Bullseye Photodetector shown in Figure [].

BPD Calibration

To use the BPDs, there are a few steps required in designing the optical setup which is different than the standard PDH or WFS method. Most notably, the beam size incident on the BPD must be tuned such that the zero crossing of the $(U_{20} + U_{02})$ matches the boundary between the inner and outer segments. This condition is met if $\omega_0 = \sqrt{2}r_0$ and Appendix C shows the power ratio of the outer to inner segments when this is true,

$$\text{Power Ratio} = \frac{P_2 + P_3 + P_4}{P_1} = \frac{e^{-2r_0^2/\omega_0^2}}{1 - e^{-2r_0^2/\omega_0^2}} \approx 0.582 \quad (5.1)$$

Picture of BPD

Pitch and Yaw sensing matrix

Demodulation phase

Another constraint on using this method is that the Gouy phase separation between successive BPDs must be close to 45 or 135 degrees so that the error signals from each BPD can be orthogonalized, this is in contrast to angular wavefront sensors which require 90 degree Gouy phase separation.

5.3.2 Mode Converters

The bullseye photodiodes can be difficult to calibrate and manufacture so a particularly interesting method of sensing mode mismatch is to convert the axisymmetric fields with a cylindrical telescope such that an error signal can be extracted with quadrant photodiode . Using lenses which have two radii of curvature for each direction (x or y) with one being flat and the orthogonal is curved with some focal length, f . The idea is to break the cylindrical symmetry of the donut mode (Figure []) and convert the beam into a pringle mode, then, an error signal can be extracted using the radio frequency quadrant photodiode that the angular wavefront sensors employ

Vector formalism for laser beams and optical cavities

Consider an optical cavity that is longitudinally resonant on the TEM_{00} mode using the Pound-Drever-Hall technique shown in Section 2.0.2 and also locked with angular wavefront sensors shown in Section 3.2. When there is a small mismatch between the waist size and position of the input beam relative to the cavity, this is equivalent to coupling the TEM-00 mode into higher order modes. Since mode matching is only concerned

with coupling to the second order modes, the resultant field in reflection (r_{FP}) of a Fabry-Perot resonator will have the form

$$|U_{refl}\rangle = r_{FP} \begin{pmatrix} U_{00} \\ 0 \\ 0 \end{pmatrix} + \epsilon \begin{pmatrix} 0 \\ U_{20} \\ U_{02} \end{pmatrix} \quad (5.2)$$

$$\epsilon = \frac{1}{\sqrt{2}} \left(\frac{\delta w}{w_0} + i \frac{\delta z}{z_R} \right) \quad (5.3)$$

where δw and δz are the mismatches in waist size and position, respectively.

O'Neil et al [59] wrote down a formalism that explicitly showed the effects of cylindrical telescopes on the full range of Hermite Gauss modes. An arbitrary mode converter is comprised of two cylindrical lenses that can be rotated about the axis of propagation shown in Figure []:

$$\hat{M} = \hat{R}\hat{C} \quad (5.4)$$

where \hat{R} is a rotation operator and \hat{C} is the mode converting operator. Since mode matching primarily couples power into the 02 and 20 modes of the cavity, we can use a 3x3 matrix. For rotations about the axis of propagation, the operator is

$$\hat{R}_{ij} = \begin{pmatrix} 1 & 0 & 0 \\ 0 & \cos(\Delta\theta) & \sin(\Delta\theta) \\ 0 & -\sin(\Delta\theta) & \cos(\Delta\theta) \end{pmatrix} \quad (5.5)$$

For the mode converter, the operator is

$$\hat{C}_{ij} = \begin{pmatrix} 1 & 0 & 0 \\ 0 & e^{-i\Omega_{20}} & 0 \\ 0 & 0 & e^{i\Omega_{02}} \end{pmatrix} \quad (5.6)$$

where $\Omega_{mn} = (m + \frac{1}{2}) \tan^{-1} \left(\frac{d}{z_{R,x}} \right) + (n + \frac{1}{2}) \tan^{-1} \left(\frac{d}{z_{R,y}} \right)$ and d is the distance from one cylindrical lens to the waist. Ω_{mn} is the amount of extra phase that a higher order mode will experience due to the mode converter. It is important to note, the matrices above show that the Gaussian beam is only astigmatic within the region of between the cylindrical lenses and unchanged outside of the telescope. If the beam reflected from the cavity is well mode matched to the cylindrical telescope, then a mode converter will introduce an

astigmatism and vary the separate Rayleigh ranges [6],

$$\frac{z_{R,x}}{z_{R,y}} = \frac{1 + d/f}{1 - d/f} \quad (5.7)$$

Of course, the tuning of θ , d and f is left up to the optical designer's choice. The obvious selection for θ should rotate the output beam such that the pringle mode intensities are centered on the individual quadrant photodiodes. The choice of separation distance d and focal length f are a bit more subtle. In Figure [] from O'Neil [59], the only conversion that transforms the diagonal HG mode into a symmetric donut mode is with $\Delta\Omega = \pi/2$. This implies the converse is true if one desires to transform the donut mode into an HG mode of the same order. Making this choice of phase propagation will automatically constrain the optical setup,

$$\frac{\pi}{2} = 2 \left[\tan^{-1} \left(\frac{d}{z_{R,x}} \right) - \tan^{-1} \left(\frac{d}{z_{R,y}} \right) \right] \quad (5.8)$$

$$\Rightarrow \sqrt{2} - 1 = \frac{d}{z_{R,y}} = \frac{z_{R,x}}{d} \quad (5.9)$$

The equation above only shows a relation between the Rayleigh ranges and the separation. However, by imposing mode matching conditions it is possible also constrain the focal length of the cylindrical lenses as well.

$$f = \left[\frac{1}{R_x(d)} - \frac{1}{R_y(d)} \right]^{-1} = \sqrt{2} d \quad (5.10)$$

Extracting information from mode

Mueller et al [56] showed that the error signal from mode mismatch could be extracted by using an RF detection scheme. Using this formalism, the error signal on a quadrant photodetector from a mismatched cavity after a mode converter is

$$\begin{aligned} S &\propto \sin(\Omega t) \text{Im} \left\{ \epsilon^* \left[\int_{A1,A3} \hat{M}_{00}^\dagger \langle U_{00} | [\hat{M}_{U_{20}}^\dagger |U_{20}\rangle + \hat{M}_{U_{02}}^\dagger |U_{02}\rangle] - \int_{A2,A4} \hat{M}_{00}^\dagger \langle U_{00} | (\hat{M}_{20}^\dagger |U_{20}\rangle + \hat{M}_{02}^\dagger |U_{02}\rangle) \right] \right\} \\ &\propto \sin(\Omega t) \text{Im} \left\{ \epsilon^* \left[\int_{A1,A3} \langle U_{00} | (|U_{20}\rangle - |U_{02}\rangle) - \int_{A2,A4} \langle U_{00} | (|U_{20}\rangle - |U_{02}\rangle) \right] \right\} \end{aligned} \quad (5.11)$$

In the above equation, \hat{C}_{ij} was chosen with $\Delta\Omega = \pi/2$ and \hat{R}_{ij} should rotate the beams such that the intensities in Figure ModeConverter are aligned with the quadrant photodiodes.

5.3.3 DC Mode Matching

The benefit to using the RF sensing scheme for generating an error signal is the automatic reduction of the higher order mode content which can use actuators to adjust the incoming mode of the beam to whatever the cavity requires. This is particularly useful in areas where the laser power density is high and absorption on the high reflectivity surfaces cause thermal distortions in the cavity mode. However, the output mode cleaner remains generally fixed in its eigenbasis such that the nominal input mode is static; in fact, the current alignment scheme uses DC quadrant photodiodes to feed back to the OMC suspensions and the control loop offsets are tuned to minimize the 10/01 modes. If there was a low-noise way to continually measure the beam size at two different Gouy phases prior to entering the output mode cleaner, then there could be an error signal which would be used for thermal actuators directly after the signal recycling cavity. This can be achieved with bullseye sensors that read power ratio relatively quickly. Another interesting way of measuring the mode is using a slowly rotating razer blade with known angular frequency in front of a single photodiode and inferring the error function which will directly give the beam size.

Chapter 6

Mode Matching Cavities at LIGO Hanford

Reference[Dan Hoake, Kognelik and Li, aLOGS]

Modeling: Finesse vs Alamode

Measurements: Mode profiling and Cavity Scanning

Misalignments described in Chapter 3 can be actively suppressed using the modal decomposition technique which leaves reduces the amount of odd order modes present in the cavity. This leaves the even order modes which arise from modal mismatch to be the dominate sources of optical losses assuming mirrors with a small amount of scatter loss(< 100 ppm).

6.1 Mode Matching IFO to OMC: Single Bounce vs DRMI

6.1.1 SR3 Heater

Beckhoff code

6.1.2 SRM Heater

- Mode Profiling: Single Bounce - OMC Scanning

6.2 Mode Matching Squeezer to OMC

- Mode Profiling - OMC Scanning - Astigmatism: expected in LIGO and measured!

6.3 Mode Matching as a Function of DARM Offset

6.4 Modal Contrast Defect

Generally, the contrast defect is defined as the ratio of power between the antisymmetric port and the reflected port when locked on a dark fringe. In other words, it is the amount of junk light that is present in the interferometer when light between the two arms do not perfectly interfere with each other. This junk light can be the symptom of various causes, for example, an imbalance of reflectivity between ITMX and ITMY will cause non-perfect destructive interference at the antisymmetric port and a camera would see a TEM00 beam when locked on length. Another cause of contrast defect could be from misalignment between the ITMs or beamsplitter which will result in seeing a TEM 01/10 mode. However, if both of the aforementioned causes are fixed with a combination of stringent design specifications for the reflectivity and alignment loops closed to minimize angular jitter, then the contrast defect will be dominated by mode mismatch which can be fixed by a combination of ring heaters and CO₂ lasers. The picture gets even more complicated when adding in the absorption for individual optics and introducing multiple Fabry-Perot cavities which will treat the sidebands and carrier fields differently. One of the main goals for the Thermal Compensation System is to correct the cold and hot interferometer differences in radii of curvature. A useful equation that relates the contrast defect to the fields incident on the \hat{x} and \hat{y} side of the beamsplitter,

$$\text{CD} = \frac{P_{AS}}{P_{REFL}} \Big|_{Dark} = \frac{1}{2} \left(1 - \int \psi_X \psi_Y dA \right) \quad (6.1)$$

where the amplitude overlap integral can be directly calculated from equation D.6.

In the modal picture, the contrast defect can be defined using the zeroth eigenmode of each arm and then expanded to project the X-arm's basis onto Y-arm using higher order Laguerre-Gauss modes, $LG_y^{00} \rightarrow LG_x^{00} + \alpha LG_x^{10}$. Where $\alpha = \frac{1}{\sqrt{2}} \left(\frac{\Delta\omega_0}{\omega_0} + i \frac{\Delta z}{z_R} \right)$ is the amount of higher order mode coupling due to mismatch in beam size and location, respectively (see Chapter 3).

$$\begin{aligned} \text{CD} &\equiv \frac{P_{AS}}{P_{REFL}} \\ &= \frac{|LG_x^{00} - LG_y^{00}|^2}{|LG_x^{00} + LG_y^{00}|^2} \\ &= \frac{|LG_x^{00}|^2 + |LG_x^{00} + \alpha LG_x^{10}|^2 - 2 \operatorname{Re}(LG_x^{00}[LG_x^{00*} + \alpha LG_x^{10}])}{|LG_x^{00}|^2 + |LG_x^{00} + \alpha LG_x^{10}|^2 + 2 \operatorname{Re}(LG_x^{00}[LG_x^{00*} + \alpha LG_x^{10}])} \\ &\approx \frac{\alpha^2}{4} \\ &\approx \frac{1}{8} \left[\left(\frac{\Delta\omega_0}{\omega_0} \right)^2 + \left(\frac{\Delta z}{z_R} \right)^2 \right] \end{aligned} \quad (6.2)$$

Mismatch between the arm cavities can stem from a few different sources such as the difference between the test mass' radii of curvature on the high reflectivity surfaces will cause the resonant modes to be different between the X-arm and Y-arm. In addition to modes being different, there exists a static (or cold) substrate lens in each of the compensation plates. This static lens becomes important for two reasons: Firstly, the sidebands in DRMI are promptly rejected by the arm cavities. Secondly, the gravitational wave sidebands which are generated and resonant in the arms will see the substrate lensing as it travels to the beamsplitter.

6.4.1 Simple Michelson Contrast Defect

The simple Michelson can give the first estimate of the contrast defect when starting to commission the interferometer, however, it will not be directly used in nominal low noise since the dual-recycled Michelson is implemented. By propagating the input mode cleaner beam to each of the input test masses and taking a single bounce at the high reflectivity surface, one can approximate the resultant mode overlap. At this point the carrier and sideband fields follow the same ABCD matrix transfer function, so only one calculation is needed to estimate the contrast defect. A keen reader will notice that this model will not take the Schnupp asymmetry into account which allows the \hat{x} -direction beam to travel an extra 8 centimeters further than the \hat{y} , however, this effect will only change the end result by approximately 10%. In fact, for this interferometer configuration, the dominate source of mismatch will be from the prompt reflection off the HR surfaces of the ITMs where most of the phase change occurs.

6.5 Hot vs. Cold Interferometers

In the previous section, the contrast defect calculations did not include the self-heating thermal effects that will be present when the interferometer reaches its nominal state. When fully operational, the arm cavities can have a few hundred kilowatts of laser power resonating while in observing mode.

An approximate but useful description of the total arm power in each arm is

$$P_{ARM} \approx \frac{1}{2}(g_{PRC} * g_{ARM} * P_{IN}) \quad (6.3)$$

where $g_{PRC} \approx 30$ is the power recycling cavity gain and $g_{ARM} \approx 250$ is the single arm cavity gain. For O3, the intended input power, P_{IN} will reach approximately 50 W which means $P_{ARM} \approx 187,500$ W. A fraction of that power, approximately .5 PPM, will be absorbed by the high reflectivity surface, hence, creating an additional thermal lens which changes the radius of curvature. Additionally, the thermo-refactive index will change as a function of absorbed temperature [75]. By changing the curvature of the test masses, the

resonant Gaussian mode will also change its profile. For the substrate lensing, the sideband signals will be most adversely affected because the carrier field will see a cancellation of the distortion from the promptly reflected beam.

6.5.1 Thermal Lensing

[76] As seen in Section 2.0.5, the sideband and carrier frequencies propagate differently in the interferometer, which means their fields will see different lensing from thermal effects. To understand how the fields change quantitatively, the easiest way is to invoke the ABCD transfer matrix approach to see how the phases change as they propagate through the optical system.

Carrier

Consider Figure 6.1, a two-mirror optical system which has an input carrier beam, E_{in}^c , that has a portion promptly reflected off the input mirror to create E_p^c

$$|E_p^c\rangle = \hat{M}_p^c |E_{in}^c\rangle \quad (6.4)$$

The prompt reflection is made up of a beam incident on a converging lens(-) from the substrate and a single reflection from the input coupler's convex(+) surface, therefore, the transfer matrix is

$$\hat{M}_p^c = \begin{bmatrix} 1 & 0 \\ -\frac{1}{f} & 1 \end{bmatrix} \begin{bmatrix} 1 & 0 \\ +\frac{2}{R} & 1 \end{bmatrix} \begin{bmatrix} 1 & 0 \\ -\frac{1}{f} & 1 \end{bmatrix} \quad (6.5)$$

where R is the radius of curvature of the high reflectivity surface and f is the focal length of the mirror substrate. In general, this can be a combination of the static lens and any thermal effects which create additional (intentional or non-intentional) lensing.

$$|E_p^c\rangle = \hat{M}_p^c \begin{bmatrix} 1 \\ \frac{1}{q_{in}} \end{bmatrix} = \begin{bmatrix} 1 \\ \frac{1}{q_{in}} + 2\left(\frac{1}{R} - \frac{1}{f}\right) \end{bmatrix} = \begin{bmatrix} 1 \\ \frac{1}{q_p} \end{bmatrix} \quad (6.6)$$

In addition, there is also a circulating field inside the cavity which leaks out can be denoted by E_ℓ^c which exits with the input coupler's radius of curvature and sees a single pass through the substrate lens,

$$|E_\ell^c\rangle = \begin{bmatrix} 1 & 0 \\ -\frac{1}{f} & 1 \end{bmatrix} \begin{bmatrix} 1 \\ \frac{1}{R} \end{bmatrix} = \begin{bmatrix} 1 \\ \frac{1}{R} - \frac{1}{f} \end{bmatrix} \quad (6.7)$$

The total reflected beam is a summation of the prompt and leaked cavity fields. LIGO uses arms which are highly over-coupled optical cavities so the promptly reflected amplitude is $|E_p^c| \approx |E_{in}|$ and using equation 2.15, the leakage amplitude is $|E_\ell^c| \approx -2|E_{in}|$. Putting all this together, the total reflected field of the carrier is

$$\begin{aligned} E_{REFL}^c &= E_\ell^c + E_p^c \\ &= E_{in} \left[\exp\left(\frac{-ikr^2}{2q_p}\right) - 2\exp\left(\frac{-ikr^2}{2q_\ell}\right) \right] \\ &\approx E_{in} \left[-1 - \frac{ikr^2}{2} \left(\frac{1}{q_p} - \frac{2}{q_\ell} \right) \right] \\ &\approx -E_{in} \exp\left(\frac{ikr^2}{2q_{in}}\right) \end{aligned} \tag{6.8}$$

This shows that the carrier field will be reflected minus the original amplitude and the same absolute curvature, however, now the beam is diverging instead of converging. The amazing part is that the end result is independent of the substrate lensing to first order.

Sidebands

Using the same formalism as the carrier fields, the sidebands will have the same input curvature, however, they do not resonate in the arms and so there is no cavity leakage field. Therefore, the sidebands will see the phase change due to the substrate lens and this has very important consequences on the sideband build up within the power recycling cavity.

GW Signal

As mentioned in Section 2.0.5, LIGO's gravitational wave readout currently employs a DC readout scheme that extracts the signal by beating the carrier field with the audio frequency sidebands created by the gravitational wave. Although the carrier field was shown to be immune to thermal lensing, the gravitational wave sideband field will see a single-passed lensing effect as it propagates out of the cavity and towards the beamsplitter. If there is a differential lensing, the signal recycling cavity will see an effective thermal lens, TL_- , which will be scattered into higher order modes. This reduces the amount of gravitational wave signal at the anti-symmetric port that is directly proportional to the mode mismatch between the arms.

6.6 Wavefront Distortions from Thermal Effects

In the previous section, it was shown that lensing in the substrate affected fields in the interferometer differently. The thermal distortion was modeled as a simple addition of phase or lensing, however, it is useful to understand how the optical path varies from first principles. A lot of work in this field was pioneered by

Hello and Vinet [42] [71] where they implemented the Heat Diffusion equation in order to analytically derive the phase change due to thermal aberrations. In general, there are two effects which occur when a beam interacts with an optic which has a temperature field: thermo-refractive and thermo-elastic.

The first arises from the index of refraction changing as a function of the temperature distribution $T(r, z)$,

$$\Delta n_r(r, z) = \frac{dn}{dT} T(r, z) \quad (6.9)$$

where $\frac{dn}{dT}$ is the temperature index coefficient and is dependent on the optic material. For example, if the heating source comes from a laser beam which imparts onto the optic a Gaussian-like intensity pattern, the temperature profile will be non-uniform and lead to a varying index of refraction that causes wavefront distortions (see Figure 6.2).

To understand how changing the index of refraction changes the optical path length, consider the function $S(r)$ which describes the surfaces which are perpendicular to the rays, therefore, if $S(r)$ is a known function then the rays can be reconstructed using the gradient, $\nabla S(r)$. As an analogy to electrostatics, $S(r)$ is similar to the potential function V such that the electric field is described by $E = -\nabla V$. As an extension of ray optics, Fermat's principle requires that the Eikonal equation be satisfied,

$$|\nabla S|^2 = n^2 \quad (6.10)$$

By integrating along the axis of propagation (\hat{z}) in Figure 6.2 through the substrate, one can find the optical path distortion

$$Z(r) = \frac{dn}{dT} \int_{z_a}^{z_b} T(r, z) dz \quad (6.11)$$

It is clear that the temperature field is key to understanding how the wavefront is distorted. In order to analytically solve for $T(r, z)$, one must use the famous Heat equation,

$$\kappa \nabla^2 T(r, z) = \rho C \frac{\partial T}{\partial t} \quad (6.12)$$

where κ is the thermal conductivity, ρ is the density, and C is the specific heat. A solution for such an equation will be a sum of three parts: $T(r, z, t) = T_s(r, z) + T_t(r, z, t) + T_0$ where the first term is the steady-state solution, the second term is the transient time-dependent solution, and the last term is the ambient temperature. For the LIGO test masses which are approximately cylindrical, the heat equation for a steady-state field becomes

$$\kappa \left[\frac{1}{r} \frac{\partial}{\partial r} \left(r \frac{\partial}{\partial r} \right) + \frac{\partial^2}{\partial z^2} \right] T_s(r, z) = 0 \quad (6.13)$$

The next step is to understand the boundary conditions using Figure 1 and the balance of heat fluxes at each of the surfaces,

$$\mathbf{n} \cdot [\mathbf{F} + \kappa \nabla T]_{\text{surf}} = 0 \quad (6.14)$$

Assuming that the outward flux is from radiation which follows the Stefan-Boltzmann law,

$$\begin{aligned} \mathbf{n} \cdot \mathbf{F}_{t_{\text{surf}}} &= \sigma_B [T^4 - T_0^4] = \sigma_B [(T(r, z) + T_0)^4 - T_0^4] \\ &\approx 4\sigma_B T_0^3 T(r, z) \end{aligned} \quad (6.15)$$

where σ_B is the Stefan-Bolzmann's constant, although depending on the material this value may vary by a scalar amount. The last part of the equation assumes that the temperature field is only a small perturbation from the ambient surroundings, $T(r, z) \ll T_0$, which allows the radiation term to become linear.

At the surface where $z = h/2$ the total flux is radiative,

$$-\kappa \frac{\partial T(r, h/2)}{\partial z} = 4\sigma_B T_0^3 T(r, h/2) \quad (6.16)$$

At the barrel of the cylinder where $r = a$, total flux is also radiative,

$$-\kappa \frac{\partial T(a, z)}{\partial r} = 4\sigma_B T_0^3 T(a, z) \quad (6.17)$$

At the surface where $z = -h/2$ there are two components of flux, one is radiative and the second is the input power from the laser beam striking the optic surface,

$$-\kappa \frac{\partial T(r, -h/2)}{\partial z} = -4\sigma_B T_0^3 T(r, -h/2) + \epsilon_a I(r) \quad (6.18)$$

where $I(r) = \frac{2P}{\pi w^2} \exp\{-2r^2/w^2\}$ is the laser beam intensity and ϵ_a is the absorption coefficient. Here, the radiative term has a negative sign to represent the flux direction. Once boundary conditions are established, most introductory textbooks that deal with partial differential equations will apply an educated guess for the solution. In this case, the resulting temperature field will be a harmonic function,

$$T_s(r, \phi, z) = (Ae^{+kz} + Be^{-kz})J_0(kr) \quad (6.19)$$

where J_0 is the spherical Bessel function of the first kind and k is a constant. Although this particular temperature distribution can be even more general by allowing all the orders of J_n , this form is sufficient.

Using the boundary condition from 6.17 and the property $\frac{\partial J_0(x)}{\partial x} = -J_1(x)$,

$$-\kappa k \frac{\partial J_0(kr)}{\partial r} \Big|_{r=a} = 4\sigma_B T_0^3 J_0(ka) \quad (6.20)$$

$$kaJ_1(ka) - \chi J_0(ka) = 0 \quad (6.21)$$

where $\chi = 4\sigma_B T_0^3 a / \kappa$ is the reduced time constant. There exists an infinite number of discrete solutions which can solve 6.21 using various values of $k_n a = \rho_n$. The temperature field then becomes,

$$T_s(r, z) = \sum_{n=0}^{\infty} (A_n e^{+k_n z} + B_n e^{-k_n z}) J_0(k_n r) \quad (6.22)$$

In order to solve the conditions from equations 6.16 and 6.18, the strategy is use the orthogonality of the spherical Bessel functions in order to expand the equations into a solvable algebraic form. This will include expanding the intensity profile $I(r)$ in this basis as well. Consider the boundary from $r = 0$ to $r = a$, the functions $J_0(k_n r)$ form a complete basis set and the normalization constant is given by the Sturm-Louisville problem,

$$\int_0^a J_0(k_n r) J_0(k_m r) r dr = \delta_{mn} \frac{[\chi^2 + (k_n a)^2]}{2k_n^2} J_0^2(k_n a) = \delta_{mn} \frac{1}{N_n} \quad (6.23)$$

Then expanding the intensity profile in terms of the Bessel function: $I(r) = \sum_n p_n J_0(k_n r)$ and inverting to solve for p_n leads to,

$$\begin{aligned} p_n &= N_n \int_0^a I(r) J_0(k_n a) r dr \\ &= N_n \int_0^a \left[\frac{2P}{\pi w^2} \right] J_0(k_n a) \exp\{-2r^2/w^2\} r dr \\ &\approx N_n \frac{P}{2\pi a^2} \exp\left\{-\frac{(k_n w)^2}{8}\right\} \end{aligned} \quad (6.24)$$

The approximation came from integrating to infinity instead of a which is reasonable if diffraction losses are small on the substrate. Plugging in the equation 6.22 and $I(r)$ into the remaining boundary conditions,

$$\left[k_n - \frac{4\sigma_B T_0^3}{\kappa} \right] e^{-k_n h} A_n - \left[k_n + \frac{4\sigma_B T_0^3}{\kappa} \right] B_n = \frac{\epsilon p_n}{\kappa} e^{-k_n h/2} \quad (6.25a)$$

$$\left[k_n + \frac{4\sigma_B T_0^3}{\kappa} \right] A_n - \left[k_n - \frac{4\sigma_B T_0^3}{\kappa} \right] B_n e^{-k_n h} = 0 \quad (6.25b)$$

Solving for A_n and B_n ,

$$A_n = \frac{\epsilon a p_n}{\kappa} e^{-3k_n h/2} \frac{\eta_+}{\eta_+ - \eta_- e^{-2k_n h}} \quad (6.26a)$$

$$B_n = \frac{\epsilon a p_n}{\kappa} e^{-k_n h/2} \frac{\eta_-}{\eta_+ - \eta_- e^{-2k_n h}} \quad (6.26b)$$

where $\eta_{\pm} = k_n \pm \frac{4\sigma_B T_0^3}{\kappa}$ is used for brevity. Now it is possible to write down the entire steady-state temperature field for a cylindrical test mass with a laser beam impinging on the surface,

$$T_s(r, z) = \sum_{n=0}^{\infty} \frac{\epsilon_a p_n}{\kappa} \frac{\eta_- e^{-k_n(3h/2-z)} + \eta_+ e^{-k_n(h/2-z)}}{\eta_+ - \eta_- e^{-2k_n h}} J_0(k_n r) \quad (6.27)$$

Once the temperature profile is solved, the path length distortion from the thermo-refractive effect can be found by solving by equation ,

$$Z_{\text{TR}}(r) = \frac{dn}{dt} \frac{\epsilon_a}{\kappa} \sum_{n=0}^{\infty} \frac{p_n}{k_n} \frac{1 - e^{-k_n h}}{[\eta_+ - \eta_- e^{-k_n h}]} J_0(k_n r) \quad (6.28)$$

where p_n contains information about the heating profile so it is possible to directly plug in equation 6.24 to represent the distortion from a Gaussian beam,

$$Z_{\text{TR}}^G(r) = \frac{dn}{dt} \frac{\epsilon_a P}{2\pi a^2 \kappa} \sum_{n=0}^{\infty} \frac{N_n}{k_n} e^{-(k_n w)^2/8} \frac{1 - e^{-k_n h}}{[\eta_+ - \eta_- e^{-k_n h}]} J_0(k_n r) \quad (6.29)$$

The thermo-refractive effect due to coating and substrate absorption is only one type, there is also an effect which elastically curves the surface from thermal expansion [71]. This thermo-elastic effect deals with the internal stresses of the material and employs the stress-strain relations in order to derive the wavefront curvature. For the LIGO test masses, this effect is smaller than the thermo-refractive wavefront distortion by about an order of magnitude.

6.7 Tuning Thermal Compensation for LIGO

Goals: Lock help with preloading [50] [12] [75] [69] As mentioned in Section 6.5.1, the amount of circulating power in each of the arms can be hundreds of kilowatts and even with absorption amounts between 0.2 – 0.5 parts per million, the induced curvature change can be significant. The Thermal Compensation System (TCS) was developed to correct the radii of curvature by applying heat to compensate the interferometer's main beam. The strategy has two main components, lock acquisition and gravitational-wave optimization.

To aid in the acquisition sequence, TCS is required to thermally lens the substrate between the beam-splitter and the high-reflectivity surfaces of the test masses such that the optical path difference is the same as a fully resonant interferometer.

First it is required to estimate the amount of absorption on the test masses by using the Hartmann wavefront sensors (see Section 6.7.1) to measure the optical path distortion induced by the interferometer during a power up. Then pre-load the ring heaters with the nominal settings which would cancel carrier

beam's thermal absorption. However, turning on the ring heaters will change the radius of curvature and induce a substrate lens (see Section 6.7.2). The overall lens now has to be canceled out by the CO₂ (Carbon Dioxide) lasers which create a lens on the compensation plate of the quadruple pendulum.

6.7.1 Hartmann Wavefront Sensors

All estimates of steady-state curvature changes due to heating by the main interferometer beam depend linearly on the absorption and this can be quite difficult to detect when the coating absorption are typically less than one part in a million.

In order to diagnose this effect, the Hartmann Wavefront Sensors (HWS) [9] [70] was a system developed by Adelaide and Caltech [10] [11] which uses a charged coupled imaging device (CCD) to sense the wavefront distortions created by heating from the interferometer beam during power up and a lock loss. After the arm power drops suddenly, the heat decays exponentially depending on the amount of absorption on the high reflective surface of the arm cavity. Using the HWS, it is possible to fit the decay rate to a finite element model of a cylindrical mass. A fitted parameter for absorption is extremely important in pre-determining the amount compensation necessary to prepare the test masses for lock acquisition. Figure 6.4 shows the measured spherical power from interferometer heating for ITMX/ITMY and comparing the two optics shows that the spherical power difference for ITMY is almost a factor of 2 larger than ITMX, the reasoning is not yet fully understood but one of the main differences between the O2 and O3 observing runs was the replacement of ITMX, ETMX, and ETMY test masses. With a fully running Hartmann Sensor system in place which monitors the wavefront curvature across the optic, long-term trends over the observation runs will be able to determine how absorption changes as a function of time and whether test masses have an innate lifetime. This will be particularly important if the next generation of detectors use much higher power levels in order to achieve better high frequency sensitivity [?].

The Hartmann code creates a gradient vector field between two times which have different thermal lensing, then numerically integrates the gradients to fit a wavefront distortion field. The algorithm then uses the Zernike polynomials as a single basis to represent the effect of the thermal lens.

One of the main successes for the Hartmann wavefront sensors have been the ability to find excess absorption due to point absorbers on the high reflectivity surfaces of the test masses. During the second observation run (O2), there was an absorber found on ITMX that made increasing the input power past 30 watts extremely difficult because it was thought to couple intensity noise into the DARM spectrum. Part way into commissioning for O3, another point absorber on ITMY was detected with the Hartmann Sensor which showed similar characteristics. The theoretical nature of these point absorbers are an active area of

research since their spatial frequencies are much higher than the uniform absorption. This affects the HWS's ability to properly evaluate total thermal lens from the interferometer, therefore changing the estimated absorption.

Because the Hartmann sensors provide one of the core estimates for the absorption, they require careful tuning in order to properly sense the wavefront distortion and extract the spherical lensing during a power up.

Picture of the HWS layout, cite Aidan.

Dead pixel removal

Digital Masking

Plane imaging [12]

6.7.2 Ring Heater Commissioning

To counteract the effects of interferometer heating, Advanced LIGO uses a ring heater [61] [72] which has two heating elements mounted on the suspension cage. Each of them are glass formers wrapped by nichrome wire that has current running through it and radiates an annular heating pattern. The ring heaters will have two effects, it will induce a substrate lens and a radius of curvature change. As shown in Section 6.5, the carrier beam will not see the substrate lens but the radius of curvature difference will change the overall modal shape of the cavity. Similar to the distortion derived in section 6.6 where the thermo-refractive effect dominates when dealing with a Gaussian beam, the same is true from the ring heaters. Using equation D.6, one can directly calculate the power overlap between a pre-loaded cavity and the original, as it turns out, the effect varies the overlap by less than 0.1%

6.7.3 CO₂ Commissioning

After using the Hartmann sensors to determine the absorption and pre-loading the ring heaters to compensate the interferometer lensing, the substrate is no longer in the nominal configuration during lock acquisition. Therefore, it is necessary to use CO₂ (Carbon Dioxide) lasers to mimic the interferometer's heating on the compensation plate.

The CO₂ lasers are located on each input test mass chamber and injected through a double zinc selenide viewport, then two steering mirrors direct the heating beam on the compensation plate of the reaction mass. In initial LIGO, the CO₂ beams were injected onto the high reflectivity surfaces of the test masses which created both a radius of curvature on the cavity side and a thermo-refractive change in the substrate. However, in advanced LIGO, the CO₂ lasers will only affect the substrate lensing.

6.7.4 SR3 Thermal Actuator

Round trip gouy phase of the SRC affecting 72 MHz wavefront sensing.

6.7.5 Putting it all together

With the sensors and tests described in the preceding sections, a cohesive plan to pre-load the interferometer must be implemented in order to achieve stable higher power operation in the detectors. Generally, the Thermal Compensation System has two goals: Firstly, the actuators are used to pre-load the test masses with heat in anticipation of the lensing due to the interferometer while operating at full lock and higher power. Secondly, the amount of mode-matching between the coupled cavities must be optimized in order to achieve the best sensitivity. Using the absorptions measured in Figure 6.4, it is possible to estimate the total amount of lensing from self-heating as a function of input power.

Higher Power Operation

The PRCL degree of freedom degrading as a function of differential substrate lensing.

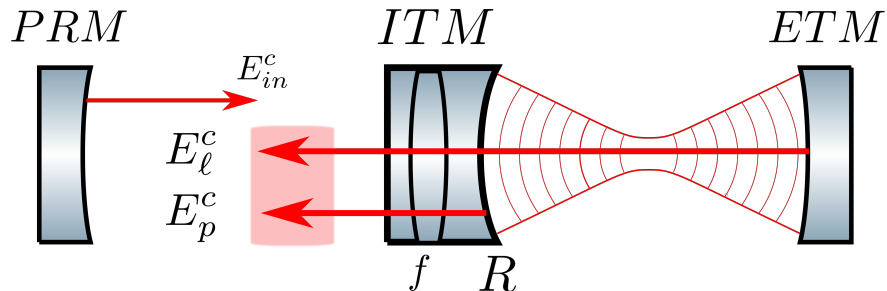


Figure 6.1: **A simplified model for the effect of a substrate thermal lens on the carrier field.** An input beam, E_{in}^c , from the power recycling mirror (PRM) will have a radius of curvature that mode matches to the input test mass (ITM). The promptly reflected beam, E_p^c , is denoted by equation 6.6 and the leakage beam, E_ℓ^c , is expressed by equation 6.7 where the sum of them would make the total reflected beam.

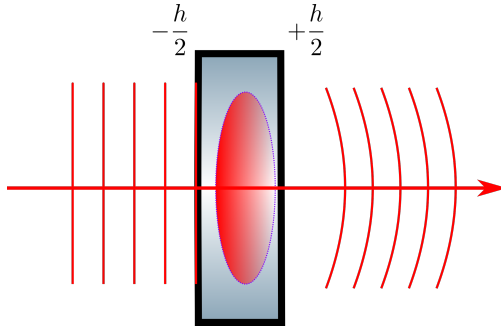


Figure 6.2: **A plane wave passing through a lens with a temperature gradient.** The index of refraction, n , depends on the material and temperature field, when a plane wave moves through such a lens, then a phase lag or lead occurs in the wavefront. Since $\frac{dn}{dT}$ is negative, the thermal distortion will resemble a diverging lens.

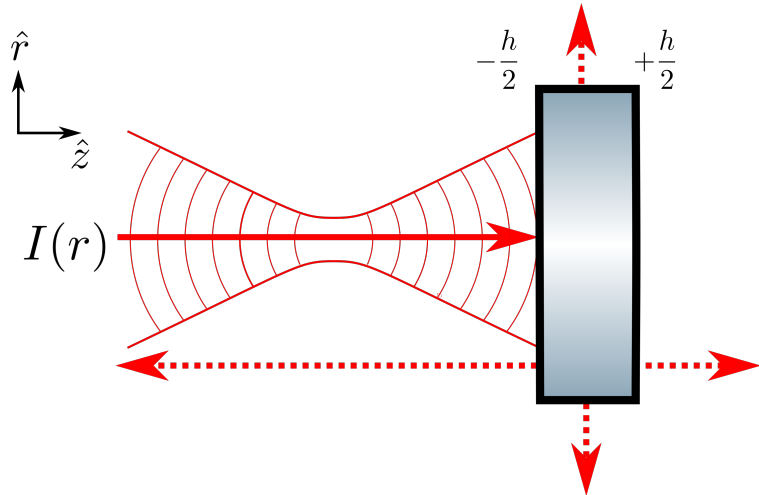


Figure 6.3: **A conceptual model of flux balance for a cylindrical object.** The red dotted lines represent the radiative fluxes escaping the optic while a Gaussian beam with intensity profile $I(r)$ is pumping energy in as denoted by the red solid line.

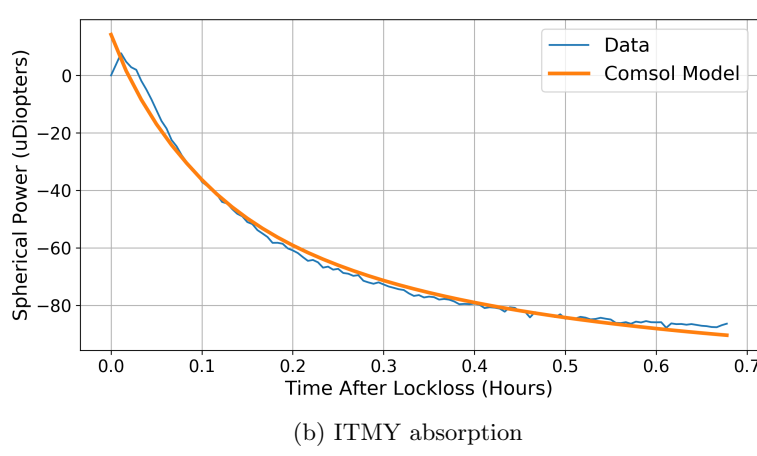
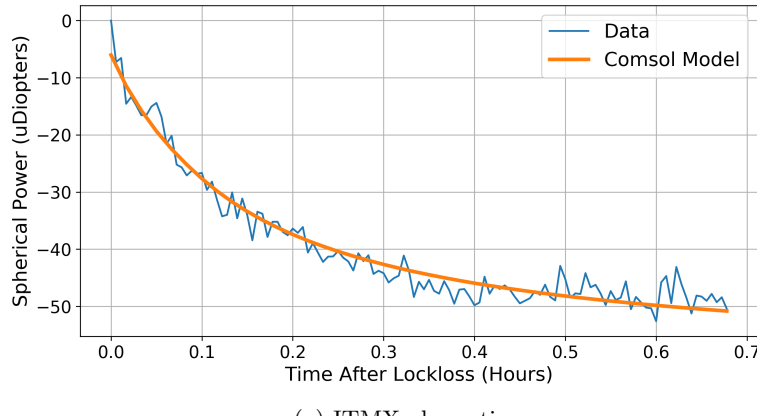


Figure 6.4: **Thermal lensing as seen by the ITM Hartmann Sensors after a lock loss.** The finite element model from COMSOL shows an exponential decay which can be linearized and fitted to the spherical power. Comparing ITMX and ITMY at Hanford shows a huge overall difference between the two optics, mostly due to the fact that ITMY has multiple point absorbers adding to the absorption estimate.

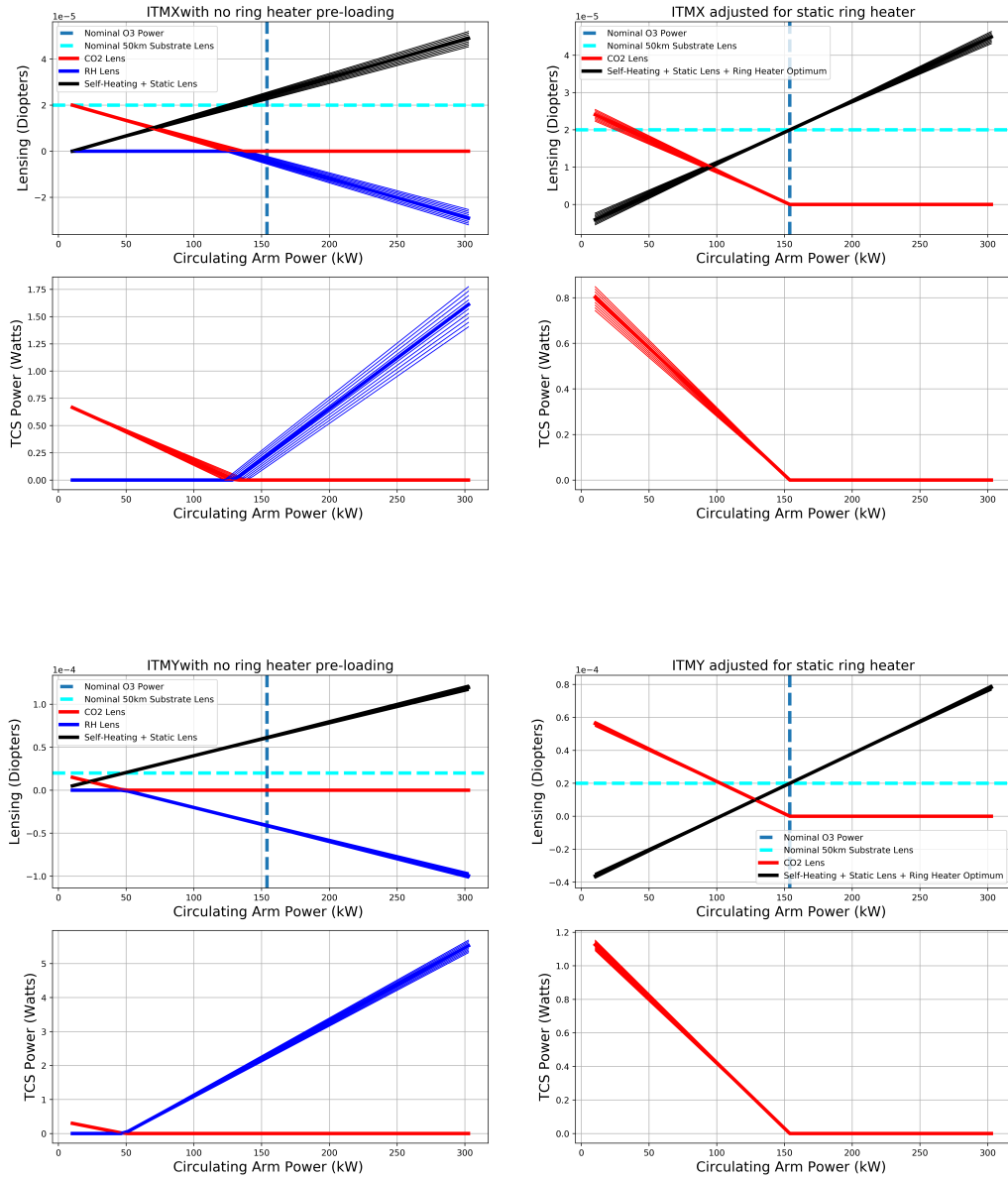


Figure 6.5: **Calculated TCS settings to balance the substrate lens.** The nominal circulating power denoted by the vertical blue line is a function of the input power, the recycling gain, and the arm cavity gain. The nominal input power for O3 will be 50 Watts and the power recycling gain is around 45. The arm cavity gain can be estimated by calibrating the transmitted power from each of the arms and is approximately 228. The horizontal, dashed turquoise line represents the nominal substrate lens with a focal length of 50 km. This value is what the power recycling cavity expects to properly mode match to the arms.

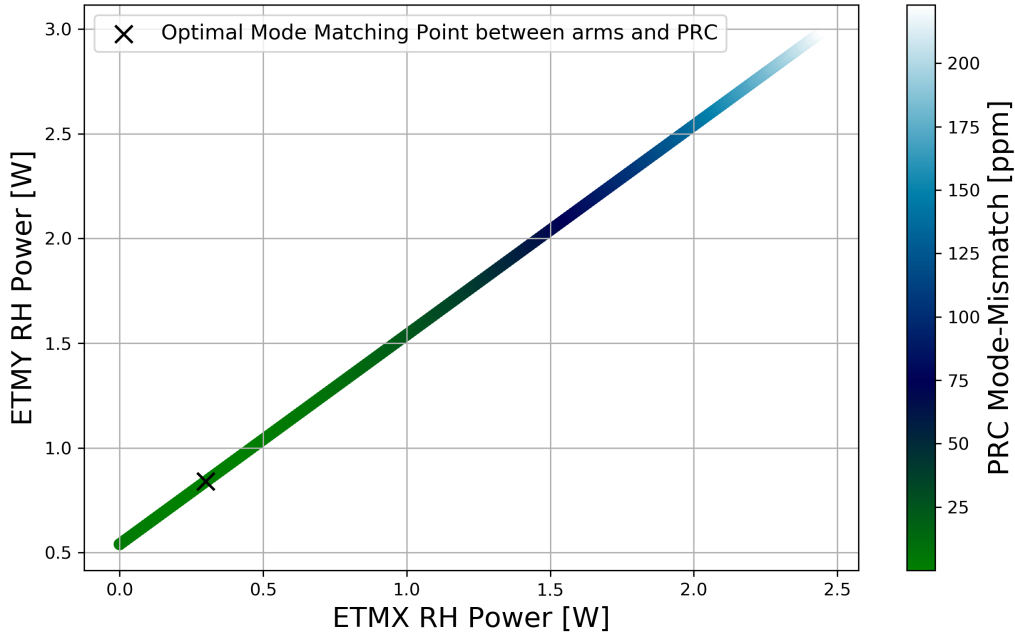


Figure 6.6: **Mode matching the arm cavities to the power recycling cavity.** Determining the ring heater and CO₂ settings still leaves the end test mass ring heaters to be set. The goal is to maintain the mode matching between the arms while simultaneously searching for the optimal overlap with the power recycling cavity. The linear portion of the graph shows a combination of common and differential adjustment of each ring heater that keeps the mode matching between the arms at less than 1 ppb,

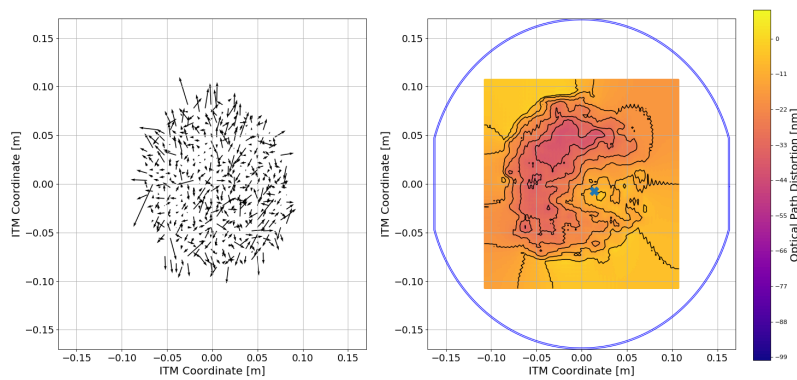


Figure 6.7: **A wavefront map measured by the Hartmann Wavefront Sensor of ITMX.**

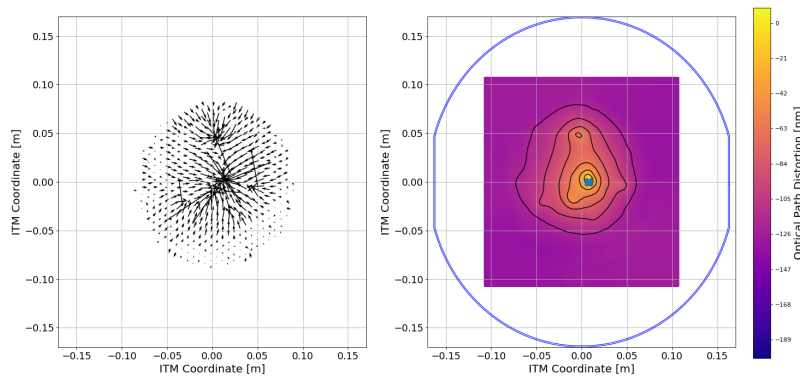


Figure 6.8: **A wavefront map measured by the Hartmann Wavefront Sensor of ITMY.**

Chapter 7

Solutions for Detector Upgrades

A solution to the current mode matching situation will be solved by further expanding active wavefront control described in Section [12]. A full modal picture, sensors and actuator

7.1 Sensors

- * Bullseye photodetectors
- * Operation: range (in terms of watts and percentage mismatch)

7.2 High Sensitivity Telescope

- * Translation stages: General principles, rigging, sensitivity
 - * Mechanical description (Solidworks designs)
 - * Constraints (range, vacuum, alignment, integration)
 - * Electronics
 - * Software
- * Implementation: rigg something better, in situ measurements.

7.3 A Global Active Wavefront Control Scheme

To truly implement a system that solves the mode matching challenges presented in LIGO, an active control scheme that implements both sensors and actuators will be required to span the degrees of freedom that are present in the interferometer.

7.3.1 Hard and Soft Mode Matching

Similar to the wavefront sensors already being used in LIGO at the time of this writing, the active wavefront system should be able to rotate the phase of their actuators and sensors to the common and differential basis. Also, the extra two degrees of freedom required are the hard and soft modes for thermal lensing which curve the ITMs and ETMs in a way which vary the waist size and position orthogonally.

Appendices

Appendix A

Resonator Formulas

Equation 2.23 describes the stability condition for a two mirror Fabry-Perot cavity. It is worthwhile to derive the criterion for geometric stability from the ray matrix tools commonly used in optics.

Consider two plane waves traveling in space shown by figure [], they differ by two quantities: the axial and angular separations, y and θ , respectively. These two quantities can be transformed via these optical matrices:

Lens

$$\hat{F}_i = \begin{pmatrix} 1 & 0 \\ -\frac{1}{f_i} & 1 \end{pmatrix} \quad (\text{A.1})$$

Curved Mirror

$$\hat{M}_i = \begin{pmatrix} 1 & 0 \\ \frac{2}{R_i} & 1 \end{pmatrix} \quad (\text{A.2})$$

Space

$$\hat{D}_i = \begin{pmatrix} 1 & d_i \\ 0 & 1 \end{pmatrix} \quad (\text{A.3})$$

Periodic Fabry-Perot with two mirrors is

$$\begin{pmatrix} y_{m+1} \\ \theta_{m+1} \end{pmatrix} = \hat{M}_{FP} \begin{pmatrix} y_m \\ \theta_m \end{pmatrix} \quad (\text{A.4})$$

where

$$\hat{M}_{FP} = \hat{M}_i \hat{D}_i \hat{M}_i \hat{D}_i \quad (\text{A.5})$$

is the optical transfer matrix. The goal is to find a geometric condition that is dependent on the optical transfer matrix which keeps the axial displacement from diverging.

$$\begin{pmatrix} y_{m+1} \\ \theta_m + 1 \end{pmatrix} = \begin{pmatrix} A & B \\ C & D \end{pmatrix} \begin{pmatrix} y_m \\ \theta_m \end{pmatrix} \quad (\text{A.6})$$

which means

$$\theta_m = \frac{y_{m+1} - A y_m}{B} \quad (\text{A.7a})$$

$$\theta_{m+1} = \frac{y_{m+2} - A y_{m+1}}{B} \quad (\text{A.7b})$$

Solving for y_{m+2}

$$y_{m+2} = (A + D) y_{m+1} - \det(\hat{M}_{FP}) y_m \quad (\text{A.8})$$

Assuming a geometrical solution where $y_m = y_0 h^m$ and plugging into the equation above,

$$h^2 = (A + D) h - \det(\hat{M}_{FP}) \quad (\text{A.9})$$

which is a quadratic equation that has two solutions and can be further simplified if the index of refraction for the entire system remains constant such that $\det(\hat{M}_{FP}) = 1$. Plugging back into y_m and doing some algebra

$$y_m \propto \sin(m\phi) \quad (\text{A.10})$$

where $\phi = \cos^{-1}(\frac{A+D}{2})$, which is also referred to as the round trip Gouy phase of the cavity. In order for y_m to be harmonic instead of hyperbolic and hence confined, this condition must be met

$$\frac{|A + D|}{2} \leq 1 \quad (\text{A.11})$$

By actually calculating the terms of \hat{M}_{FP} and doing even more algebra, it is clear that

$$0 \leq \left(1 - \frac{L}{R_1}\right) \left(1 - \frac{L}{R_2}\right) \leq 1 \quad (\text{A.12})$$

which is what was stated in equation 2.23.

There is a simpler and less algebraic way to reach the same conclusion by looking at the Rayleigh range

of a finite Gaussian beam for a simple cavity. In Table II of Kogelnik and Li [49], there is an expression for the Rayleigh range

$$\begin{aligned} z_R^2 &= \frac{L(R_1 - L)(R_2 - L)(R_1 + R_2 - L)}{(R_1 + R_2 - 2L)^2} \\ &= \frac{g_1 g_2 (1 - g_1 g_2)}{(g_1 - g_2 - 2g_1 g_2)^2} \end{aligned} \quad (\text{A.13})$$

If the Rayleigh range is a real number, then once again, equation 2.23 must be true.

Appendix B

Hermite Gauss Normalization

According to equation 3.12, the higher order modes in the Hermite Gauss basis has the intensity profile,

$$I_{mn}(x, y, z) = |A_{mn}|^2 \left[\frac{W_0}{W(z)} \right]^2 \mathbb{G}_n^2 \left(\frac{\sqrt{2}x}{W(z)} \right) \mathbb{G}_n^2 \left(\frac{\sqrt{2}y}{W(z)} \right) \quad (\text{B.1})$$

It is useful to normalize the first few lowest order modes with respect to the total optical power since the Gaussian beam will couple to them the most due either misalignment or mode mismatch as seen in section [].

In one dimension, the total optical power for the first 3 modes are

$$\begin{aligned} P_0(x, y, z) &= \int_{-\infty}^{\infty} |A_0|^2 \left[\frac{W_0}{W(z)} \right] e^{-2x^2/w^2(z)} dx \\ P_1(x, y, z) &= \int_{-\infty}^{\infty} |A_1|^2 \left[\frac{W_0}{W(z)} \right] \frac{8x^2}{w^2(z)} e^{-2x^2/w^2(z)} dx \\ P_2(x, y, z) &= \int_{-\infty}^{\infty} |A_2|^2 \left[\frac{W_0}{W(z)} \right] \left(\frac{8x^2}{w^2(z)} - 2 \right)^2 e^{-2x^2/w^2(z)} dx \end{aligned} \quad (\text{B.2})$$

In two dimensions, the total optical power for the first 3 modes are

$$\begin{aligned} P_{00}(x, y, z) &= \int_{-\infty}^{\infty} \int_{-\infty}^{\infty} |A_{00}|^2 \left[\frac{W_0}{W(z)} \right]^2 e^{-2x^2/w^2(z)} e^{-2y^2/w^2(z)} dx dy \\ P_{10}(x, y, z) &= \int_{-\infty}^{\infty} \int_{-\infty}^{\infty} |A_{10}|^2 \left[\frac{W_0}{W(z)} \right]^2 \frac{8x}{w^2(z)} e^{-2x^2/w^2(z)} e^{-2y^2/w^2(z)} dx dy \\ P_{20}(x, y, z) &= \int_{-\infty}^{\infty} \int_{-\infty}^{\infty} |A_{20}|^2 \left[\frac{W_0}{W(z)} \right]^2 \left(\frac{8x^2}{w^2(z)} - 2 \right)^2 e^{-2x^2/w^2(z)} e^{-2y^2/w^2(z)} dx dy \end{aligned} \quad (\text{B.3})$$

By setting the equations above to unity, the normalization factors become

$$\begin{aligned}
 A_0 &= \left(\frac{2}{\pi w_0^2} \right)^{1/4} \\
 A_1 &= \left(\frac{2}{\pi w_0^2} \right)^{1/4} \frac{1}{\sqrt{2}} \\
 A_2 &= \left(\frac{2}{\pi w_0^2} \right)^{1/4} \frac{1}{\sqrt{8}}
 \end{aligned} \tag{B.4}$$

$$\begin{aligned}
 A_{00} &= \sqrt{\frac{2}{\pi w_0^2}} \\
 A_{10} &= \sqrt{\frac{1}{\pi w_0^2}} \\
 A_{20} &= \sqrt{\frac{1}{4\pi w_0^2}}
 \end{aligned} \tag{B.5}$$

Therefore the normalized modes are

Appendix C

Bullseye and Quadrant Photodiode Characterization

Both RF and DC segmented photodiodes are widely used in LIGO’s sensing schemes, however, the quadrant photodiodes (QPDs) are more readily implemented. Recently, a bullseye photodiode has been installed upstream of the pre-mode cleaner to sense the size and angular jitter noise contribution from the high powered oscillator. It is useful to have angular sensors both upstream and downstream of optical cavities to narrow down where jitter could be coupling into the optical path. That being said, to calibrate the two types of sensors in common units, it is easiest to scale by beam diameters.

C.1 Quadrant Photodiodes (QPD)

Calculating the QPD response to angular jitter is relatively straight forward. Beginning with a Gaussian beam in rectangular coordinates that is displaced along the horizontal axis by a small value Δx and expanding to first order:

$$\begin{aligned} I(x, y) &= \left(\frac{2}{\pi w^2} \right) e^{-2 \frac{(x+\Delta x)^2 + y^2}{w^2}} \\ &\approx \left(\frac{2}{\pi w^2} \right) e^{-2 \frac{x^2 + y^2}{w^2}} \left(1 - \frac{4x\Delta x}{w^2} \right) \end{aligned} \tag{C.1}$$

	Seg 1	Seg 2	Seg 3	Seg 4
Pit	1	1	-2	0
Yaw	-1	1	0	0
Wid	1	1	1	-1
Sum	1	1	1	1

Table C.1: Bullseye photodiode sensing matrix.

Converting to polar coordinates where $x = r \cos \theta$ and $y = r \sin \theta$ then integrating over the individual segments to get the power,

$$\begin{aligned}
P &= \left(\frac{2}{\pi w^2} \right) \int_0^\infty \int_{\theta_1}^{\theta_2} e^{-2\frac{r^2}{\omega^2}} \left(1 - \frac{4r \cos \theta}{w^2} \Delta x \right) r dr d\theta \\
&= \frac{1}{2} - [\cos \theta_2 - \cos \theta_1] \frac{8 \Delta x}{\pi \omega^4} \int_0^\infty e^{-2\frac{r^2}{\omega^2}} r^2 dr \\
&= \frac{1}{2} - [\cos \theta_2 - \cos \theta_1] \frac{\Delta x}{2\pi \omega^2} \left(\sqrt{2\pi} \omega \operatorname{erf}\left(\frac{\sqrt{2}r}{\omega}\right) - 4r e^{-2\frac{r^2}{\omega^2}} \right) \Big|_0^\infty \\
&= \frac{1}{2} - [\cos \theta_2 - \cos \theta_1] \frac{\Delta x}{w} \sqrt{\frac{1}{2\pi}}
\end{aligned} \tag{C.2}$$

where θ_1 and θ_2 are the limits from $\pm\pi/2$ for the right half and $\mp\pi/2$ for the left half. Denoting the right and left segment as P_2 and P_1 , respectively, it is possible to subtract the halves and obtain a calibrated DC signal in units of beam diameter.

$$S = P_2 - P_1 = 2 \sqrt{\frac{2}{\pi}} \frac{\Delta x}{\omega} \tag{C.3}$$

It is trivial to repeat the calculation for vertical displacements so it is left for the reader to complete.

C.2 Bullseye Photodiodes

Similar to the QPD calibration above, it is possible to express pitch and yaw displacements that are normalized to beam diameters. Additionally, the bullseye's geometry will give insight on the beam size jitter. A sensing matrix for these degrees of freedom is realized in Table C.1

C.2.1 Width

The bullseye's calibration is determined in a similar manner to the QPD however, the sensitivity will inherently depend on the beam size. To calculate what beam size is optimal, first consider a power integral for a

cylindrically symmetric Gaussian beam,

$$\begin{aligned} \text{Power} &= \int_A^B |A_{00}|^2 e^{\frac{-2r^2}{\omega^2}} 2\pi r dr \\ &= -|A_{00}|^2 \frac{\pi\omega^2}{2} e^{\frac{-2r^2}{\omega^2}} \Big|_A^B \end{aligned} \quad (\text{C.4})$$

Plugging in limits for the equation where R is the boundary between the inner and outer segments,

$$P_{in} = \text{Power} \Big|_0^R = |A_{00}|^2 \frac{\pi\omega^2}{2} [1 - e^{\frac{-2R^2}{\omega^2}}] \quad (\text{C.5})$$

$$P_{out} = \text{Power} \Big|_R^\infty = |A_{00}|^2 \frac{\pi\omega^2}{2} [e^{\frac{-2R^2}{\omega^2}}] \quad (\text{C.6})$$

The error signal comes from subtracting the inner segment from the outer,

$$S_{WID} = P_{in} - P_{out} \quad (\text{C.7})$$

Minimizing the derivative with respect to the beam size will determine the optimal width which gives the best sensitivity to beam size change,

$$\begin{aligned} \frac{\partial S_{WID}}{\partial \omega} &\approx \frac{8R^2}{\omega^2} \left(1 - \frac{2R^2}{\omega^2} \right) = 0 \\ \Rightarrow \omega &= \sqrt{2}R \end{aligned} \quad (\text{C.8})$$

When determining the beam size, it is possible to measure the beam size directly by fitting the power ratio. For example, if the constraint that $\omega = \sqrt{2}R$ then the power ratio is,

$$\text{DC Power Ratio} = \frac{P_{out}}{P_{in}} = \frac{e^{-2R^2/\omega_0^2}}{1 - e^{-2R^2/\omega_0^2}} \approx 0.582 \quad (\text{C.9})$$

C.2.2 Pitch

To calibrate the pitch signal on a bullseye, first consider a Gaussian that is displaced in the vertical direction,

$$\begin{aligned} I^{\text{Pit}}(x, y) &= \left(\frac{2}{\pi w^2} \right) e^{-2 \frac{x^2 + (y + \Delta y)^2}{w^2}} \\ &\approx \left(\frac{2}{\pi w^2} \right) e^{-2 \frac{x^2 + y^2}{w^2}} \left(1 - \frac{4x\Delta y}{w^2} \right) \end{aligned} \quad (\text{C.10})$$

The integrated power for a given segment is,

$$\begin{aligned} P_{\theta_1 \rightarrow \theta_2}^{\text{Pit}} &= \left(\frac{2}{\pi w^2} \right) \int_R^\infty \int_{\theta_1}^{\theta_2} e^{-2\frac{r^2}{\omega^2}} \left(1 - \frac{4r \sin \theta}{w^2} \Delta y \right) r dr d\theta \\ &= \left(\frac{\theta_2 - \theta_1}{2\pi} \right) e^{-2\frac{R^2}{\omega^2}} + (\cos \theta_2 - \cos \theta_1) \frac{1}{\sqrt{2\pi}} \frac{\Delta y}{\omega} \left[\operatorname{erfc} \left(\frac{\sqrt{2}R}{\omega} \right) \sqrt{\frac{8}{\pi}} \frac{R}{\omega} e^{-2\frac{R^2}{\omega^2}} \right] \end{aligned} \quad (\text{C.11})$$

The error signal from a pitch displacement following Table C.1 is,

$$S^{\text{Pit}} = P_{\text{seg}_1}^{\text{Pit}} + P_{\text{seg}_2}^{\text{Pit}} - 2P_{\text{seg}_3}^{\text{Pit}} = 3 \sqrt{\frac{3}{2\pi}} \frac{\Delta y}{\omega} \left[\operatorname{erfc} \left(\frac{\sqrt{2}R}{\omega} \right) + \sqrt{\frac{8}{\pi}} \frac{R}{\omega} e^{-2\frac{R^2}{\omega^2}} \right] \quad (\text{C.12})$$

C.2.3 Yaw

Using C.1 and repeating the mathematics above, the power for an individual segment is

$$\begin{aligned} P_{\theta_1 \rightarrow \theta_2}^{\text{Yaw}} &= \left(\frac{2}{\pi w^2} \right) \int_R^\infty \int_{\theta_1}^{\theta_2} e^{-2\frac{r^2}{\omega^2}} \left(1 - \frac{4r \cos \theta}{w^2} \Delta x \right) r dr d\theta \\ &= \left(\frac{\theta_2 - \theta_1}{2\pi} \right) e^{-2\frac{R^2}{\omega^2}} + (\cos \theta_2 - \cos \theta_1) \frac{1}{\sqrt{2\pi}} \frac{\Delta x}{\omega} \left[\operatorname{erfc} \left(\frac{\sqrt{2}R}{\omega} \right) \sqrt{\frac{8}{\pi}} \frac{R}{\omega} e^{-2\frac{R^2}{\omega^2}} \right] \end{aligned} \quad (\text{C.13})$$

Plugging in the angles to get the signal response in terms of beam radius,

$$S^{\text{Yaw}} = P_{\text{seg}_1}^{\text{Yaw}} - P_{\text{seg}_2}^{\text{Yaw}} = \frac{3}{\sqrt{2\pi}} \frac{\Delta x}{\omega} \left[\operatorname{erfc} \left(\frac{\sqrt{2}R}{\omega} \right) + \sqrt{\frac{8}{\pi}} \frac{R}{\omega} e^{-2\frac{R^2}{\omega^2}} \right] \quad (\text{C.14})$$

C.2.4 RF

$$\begin{aligned} P_{RF} &= \int_A^B |A_{01}|^2 \left(1 - \frac{2r^2}{\omega_0^2} \right) e^{\frac{-2r^2}{\omega_0^2}} 2\pi r dr \\ &= -|A_{00}|^2 \frac{\pi}{2} \omega_0^2 e^{\frac{-2r^2}{\omega_0^2}} \left(1 + \frac{4r_4}{\omega_0^4} \right) \Big|_A^B \end{aligned} \quad (\text{C.15})$$

$$P_{in} = P_{RF} \Big|_0^{r_0} = -|A_{01}|^2 \frac{\pi}{2} \omega_0^2 \left(e^{\frac{-2r^2}{\omega_0^2}} \left(1 + \frac{4r_4}{\omega_0^4} \right) - 1 \right) \quad (\text{C.16})$$

$$P_{out} = P_{RF} \Big|_{r_0}^{\infty} = -|A_{01}|^2 \frac{\pi}{2} \omega_0^2 e^{\frac{-2r^2}{\omega_0^2}} \left(1 + \frac{4r_4}{\omega_0^4} \right) \quad (\text{C.17})$$

$$\text{RF Power Ratio} = \frac{P_{out}}{P_{in}} = \frac{e^{-2r_0^2/\omega_0^2}}{1 - e^{-2r_0^2/\omega_0^2}} \approx 2.7844 \quad (\text{C.18})$$

Appendix D

Overlap of Gaussian Beams

Referenced in section When a cavity is mode mismatched to an incoming laser field, the amount of power loss from scattering to higher order modes is quantified by the spatial overlap integral between the TEM00 cavity eigenmode and TEM00 of the input beam. An arbitrary Gaussian integral is defined as,

$$\begin{aligned} |A(r)\rangle &= \frac{A_0}{q(z)} e^{\frac{-ikr^2}{2q(z)}} \\ &= \frac{A_0}{q(z)} e^{\frac{-ikr^2(z-iz_0)}{2|q(z)|^2}} \end{aligned} \quad (\text{D.1})$$

where A_0 is a real amplitude, $q(z) = z + iz_0$ is the complex beam parameter, k is the wave number, and r is the radial variable in the transverse direction. Then normalizing to unity,

$$\langle A(r)|A(r)\rangle = \frac{|A_0|^2}{z^2 + z_0^2} \int_0^\infty e^{\frac{-kr^2 z_0}{|q(z)|^2}} 2\pi r dr = 1 \quad (\text{D.2})$$

$$A_0 = \sqrt{\frac{kz_0}{\pi}} \quad (\text{D.3})$$

For a Gaussian beam with arbitrary q-parameters,

$$|A_i\rangle = \frac{A_{0,i}}{q_i} e^{\frac{-ikr^2(z-iz_0)}{2|q_i|^2}} \quad (\text{D.4})$$

where $z_{0,i}$ is the waist size of one particular beam, the overlap integral for the amplitude becomes

$$\langle A_1|A_2\rangle = 2i \frac{z_{0,1}z_{0,2}}{q_1 - q_2^*} \quad (\text{D.5})$$

So the power overlap is:

$$\text{Power Overlap} = |\langle A_1 | A_2 \rangle|^2 = 4 \frac{z_{0,1} z_{0,2}}{|q_1 - q_2^*|^2} \quad (\text{D.6})$$

Essentially, mode matching an optical system only requires the designer to match the q-parameter of the incoming beam to the cavity, so it makes sense that the final power overlap depends only on the waist size and location.

List of Figures

1.1	A ring of free floating particles being stretched and squeezed by a passing gravitational wave.	7
1.2	A Michelson Interferometer.	8
1.3	Detector to radiation frame.	9
1.4	The phase response of an interferometer to a gravitational wave.	11
2.1	A heterodyne detection scheme for interferometers.	17
2.2	Delay Line (top) vs Fabry Perot (bottom)	19
2.3	The reflected, circulating, and transmitted powers for a single Fabry-Perot cavity.	20
2.4	Bode Plots of a linear Fabry-Perot response in reflection.	20
2.5	Control scheme for an optical cavity.	23
2.6	Error signal in reflection	24
2.7	Michelson with Fabry Perot arms	25
2.8	A power recycled Fabry-Perot interferometer.	26
2.9	A dual recycled Fabry-Perot interferometer.	28
2.10	Shot noise limited sensitivity	28
2.11	Quantum limited sensitivity by combining shot noise and radiation pressure	29
2.12	Displacement spectrum for thermal noise.	39
2.13	The amplitude spectral density of gravitational wave strain normalized by the standard quantum limit.	40
2.14	Add a caption	41
3.1	A depiction of the Gaussian beam properties with respect to cylindrical coordinates.	45
3.2	Beam size, radius of curvature, and Gouy phase as a function of distance propagation from the waist.	46
3.3	Intensity	47

3.4 A Finesse model of a longitudinal mode scan comparing the Advanced LIGO power recycling and signal recycling cavities.	48
5.1 MEDM master screen for adaptive mode matching at Syracuse	57
6.1 A simplified model for the effect of a substrate thermal lens on the carrier field.	73
6.2 A plane wave passing through a lens with a temperature gradient.	74
6.3 A conceptual model of flux balance for a cylindrical object.	74
6.4 Thermal lensing as seen by the ITM Hartmann Sensors after a lock loss.	75
6.5 Calculated TCS settings to balance the substrate lens.	76
6.6 Mode matching the arm cavities to the power recycling cavity.	77
6.7 A wavefront map measured by the Hartmann Wavefront Sensor of ITMX.	77
6.8 A wavefront map measured by the Hartmann Wavefront Sensor of ITMY.	78

List of Tables

C.1 Bullseye photodiode sensing matrix.	88
---	----

Bibliography

- [1] J. Abadie et al. Sensitivity Achieved by the LIGO and Virgo Gravitational Wave Detectors during LIGO’s Sixth and Virgo’s Second and Third Science Runs. *arXiv*, 2012. 9
- [2] B. P. e. a. Abbott. Observation of gravitational waves from a binary black hole merger. *Phys. Rev. Lett.*, 116:061102, Feb 2016. doi: 10.1103/PhysRevLett.116.061102. URL <https://link.aps.org/doi/10.1103/PhysRevLett.116.061102>. 5
- [3] R. Abbott, R. Adhikari, G. Allen, S. Cowley, E. Daw, D. DeBra, J. Giaime, G. Hammond, M. Hammond, C. Hardham, J. How, W. Hua, W. Johnson, B. Lantz, K. Mason, R. Mittleman, J. Nichol, S. Richman, J. Rollins, D. Shoemaker, G. Stapfer, and R. Stebbins. Seismic isolation for advanced ligo. *Classical and Quantum Gravity*, 19(7):1591, 2002. URL <http://stacks.iop.org/0264-9381/19/i=7/a=349>. 35
- [4] and and. Ix. a determination of the deflection of light by the sun’s gravitational field, from observations made at the total eclipse of may 29, 1919. *Philosophical Transactions of the Royal Society of London A: Mathematical, Physical and Engineering Sciences*, 220(571-581):291–333, 1920. ISSN 0264-3952. doi: 10.1098/rsta.1920.0009. URL <http://rsta.royalsocietypublishing.org/content/220/571-581/291>. 5
- [5] D. Z. Anderson. Alignment of resonant optical cavities. *Appl. Opt.*, 23(17):2944–2949, Sep 1984. doi: 10.1364/AO.23.002944. URL <http://ao.osa.org/abstract.cfm?URI=ao-23-17-2944>. 48
- [6] M. Beijersbergen, L. Allen, H. van der Veen, and J. Woerdman. Astigmatic laser mode converters and transfer of orbital angular momentum. *Optics Communications*, 96(1):123 – 132, 1993. ISSN 0030-4018. doi: [https://doi.org/10.1016/0030-4018\(93\)90535-D](https://doi.org/10.1016/0030-4018(93)90535-D). URL <http://www.sciencedirect.com/science/article/pii/003040189390535D>. 47, 60
- [7] E. D. Black. An introduction to pound–drever–hall laser frequency stabilization. *American Journal of Physics*, 69(1):79–87, 2001. doi: 10.1119/1.1286663. URL <https://doi.org/10.1119/1.1286663>. 18, 22

- [8] D. G. Blair. *The detection of gravitational waves*. Cambridge University Press, 2005. 35
- [9] A. Brooks, P. Veitch, J. Munch, and T.-L. Kelly. An off-axis hartmann sensor for the measurement of absorption-induced wavefront distortion in advanced gravitational wave interferometers. *General Relativity and Gravitation*, 37(9):1575–1580, Sep 2005. ISSN 1572-9532. doi: 10.1007/s10714-005-0137-5. URL <https://doi.org/10.1007/s10714-005-0137-5>. 71
- [10] A. F. Brooks, T.-L. Kelly, P. J. Veitch, and J. Munch. Ultra-sensitive wavefront measurement using a hartmann sensor. *Opt. Express*, 15(16):10370–10375, Aug 2007. doi: 10.1364/OE.15.010370. URL <http://www.opticsexpress.org/abstract.cfm?URI=oe-15-16-10370>. 71
- [11] A. F. Brooks, D. Hosken, J. Munch, P. J. Veitch, Z. Yan, C. Zhao, Y. Fan, L. Ju, D. Blair, P. Willems, B. Slagmolen, and J. Degallaix. Direct measurement of absorption-induced wavefront distortion in high optical power systems. *Appl. Opt.*, 48(2):355–364, Jan 2009. doi: 10.1364/AO.48.000355. URL <http://ao.osa.org/abstract.cfm?URI=ao-48-2-355>. 71
- [12] A. F. Brooks, B. Abbott, M. A. Arain, G. Ciani, A. Cole, G. Grabeel, E. Gustafson, C. Guido, M. Heintze, A. Heptonstall, M. Jacobson, W. Kim, E. King, A. Lynch, S. O'Connor, D. Ottaway, K. Mailand, G. Mueller, J. Munch, V. Sannibale, Z. Shao, M. Smith, P. Veitch, T. Vo, C. Vorvick, and P. Willems. Overview of advanced ligo adaptive optics. *Appl. Opt.*, 55(29):8256–8265, Oct 2016. doi: 10.1364/AO.55.008256. URL <http://ao.osa.org/abstract.cfm?URI=ao-55-29-8256>. 70, 72, 79
- [13] A. Buonanno and Y. Chen. Quantum noise in second generation, signal-recycled laser interferometric gravitational-wave detectors. *Phys. Rev. D*, 64:042006, Jul 2001. doi: 10.1103/PhysRevD.64.042006. URL <https://link.aps.org/doi/10.1103/PhysRevD.64.042006>. 31
- [14] S. M. Carroll. *Spacetime and geometry: an introduction to general relativity*. Pearson, 2003. 6
- [15] C. M. Caves. Quantum-mechanical noise in an interferometer. *Phys. Rev. D*, 23:1693–1708, Apr 1981. doi: 10.1103/PhysRevD.23.1693. URL <https://link.aps.org/doi/10.1103/PhysRevD.23.1693>. 31
- [16] C. M. Caves and B. L. Schumaker. New formalism for two-photon quantum optics. i. quadrature phases and squeezed states. *Phys. Rev. A*, 31:3068–3092, May 1985. doi: 10.1103/PhysRevA.31.3068. URL <https://link.aps.org/doi/10.1103/PhysRevA.31.3068>. 31, 39
- [17] C. M. Caves, K. S. Thorne, R. W. P. Drever, V. D. Sandberg, and M. Zimmermann. On the measurement of a weak classical force coupled to a quantum-mechanical oscillator. i. issues of principle. *Rev. Mod. Phys.*, 52:341–392, Apr 1980. doi: 10.1103/RevModPhys.52.341. URL <https://link.aps.org/doi/10.1103/RevModPhys.52.341>. 31

- [18] J. L. Cervantes-Cota, S. Galindo-Uribarri, and G. F. Smoot. A brief history of gravitational waves. *Universe*, 2(3), 2016. ISSN 2218-1997. doi: 10.3390/universe2030022. URL <http://www.mdpi.com/2218-1997/2/3/22>. 7
- [19] Y. Chen, S. L. Danilishin, F. Y. Khalili, and H. Müller-Ebhardt. Qnd measurements for future gravitational-wave detectors. *General Relativity and Gravitation*, 43(2):671–694, Feb 2011. ISSN 1572-9532. doi: 10.1007/s10714-010-1060-y. URL <https://doi.org/10.1007/s10714-010-1060-y>. 31
- [20] T. L. S. Collaboration. A gravitational wave observatory operating beyond the quantum shot-noise limit. *Nature Physics*, 7:962, Nov 2009. doi: 10.1038/nphys2083. URL <http://dx.doi.org/10.1038/nphys2083>. 39
- [21] T. L. S. Collaboration. Enhanced sensitivity of the ligo gravitational wave detector by using squeezed states of light. *Nature Physics*, 7:613, Jul 2013. doi: 10.1038/nphoton.2013.177. URL <http://dx.doi.org/10.1038/nphoton.2013.177>. 39
- [22] T. L. S. Collaboration. Advanced ligo. *Classical and Quantum Gravity*, 32(7):074001, 2015. URL <http://stacks.iop.org/0264-9381/32/i=7/a=074001>. 23
- [23] H. Collins. *Gravity's shadow: the search for gravitational waves*. University of Chicago Press, 2004. 7
- [24] R. DeRosa, J. C. Driggers, D. Atkinson, H. Miao, V. Frolov, M. Landry, J. A. Giaime, and R. X. Adhikari. Global feed-forward vibration isolation in a km scale interferometer. *Classical and Quantum Gravity*, 29(21):215008, 2012. URL <http://stacks.iop.org/0264-9381/29/i=21/a=215008>. 35
- [25] J. C. Driggers, J. Harms, and R. X. Adhikari. Subtraction of newtonian noise using optimized sensor arrays. , 86(10):102001, Nov. 2012. doi: 10.1103/PhysRevD.86.102001. 38
- [26] A. Einstein. Die grundlage der allgemeinen relativitätstheorie. *Annalen der Physik*, 354(7):769–822, 1905. doi: 10.1002/andp.19163540702. URL <https://onlinelibrary.wiley.com/doi/abs/10.1002/andp.19163540702>. 5
- [27] A. Einstein. Investigations on the theory of the brownian movement. *Ann. der Physik*, 1905. URL http://www.physik.fu-berlin.de/~{}kleinert/files/eins_brownian.pdf. 35
- [28] A. Einstein. Zur Elektrodynamik bewegter Körper. (German) [On the electrodynamics of moving bodies]. *Annalen der Physik*, 322(10):891–921, 1905. doi: <http://dx.doi.org/10.1002/andp.19053221004>.

- [29] R. W. et al. Ligo document m890001-v3, 1989. URL <https://dcc.ligo.org/LIGO-M890001/public>. 11
- [30] M. Evans, S. Ballmer, M. Fejer, P. Fritschel, G. Harry, and G. Ogin. Thermo-optic noise in coated mirrors for high-precision optical measurements. *Phys. Rev. D*, 78:102003, Nov 2008. doi: 10.1103/PhysRevD.78.102003. URL <https://link.aps.org/doi/10.1103/PhysRevD.78.102003>. 38
- [31] M. Evans, L. Barsotti, P. Kwee, J. Harms, and H. Miao. Realistic filter cavities for advanced gravitational wave detectors. *Phys. Rev. D*, 88:022002, Jul 2013. doi: 10.1103/PhysRevD.88.022002. URL <https://link.aps.org/doi/10.1103/PhysRevD.88.022002>. 40
- [32] L. S. Finn. Binary inspiral, gravitational radiation, and cosmology. *Phys. Rev.*, D53:2878–2894, 1996. doi: 10.1103/PhysRevD.53.2878. 9, 12, 13
- [33] P. Fritschel, D. Shoemaker, and R. Weiss. Demonstration of light recycling in a michelson interferometer with fabry–perot cavities. *Appl. Opt.*, 31(10):1412–1418, Apr 1992. doi: 10.1364/AO.31.001412. URL <http://ao.osa.org/abstract.cfm?URI=ao-31-10-1412>. 26
- [34] P. Fritschel, N. Mavalvala, D. Shoemaker, D. Sigg, M. Zucker, and G. González. Alignment of an interferometric gravitational wave detector. *Appl. Opt.*, 37(28):6734–6747, Oct 1998. doi: 10.1364/AO.37.006734. URL <http://ao.osa.org/abstract.cfm?URI=ao-37-28-6734>. 35
- [35] P. Fritschel, R. Bork, G. González, N. Mavalvala, D. Ouimette, H. Rong, D. Sigg, and M. Zucker. Readout and control of a power-recycled interferometric gravitational-wave antenna. *Appl. Opt.*, 40(28):4988–4998, Oct 2001. doi: 10.1364/AO.40.004988. URL <http://ao.osa.org/abstract.cfm?URI=ao-40-28-4988>. 18, 23
- [36] P. Fritschel, R. Bork, G. González, N. Mavalvala, D. Ouimette, H. Rong, D. Sigg, and M. Zucker. Readout and control of a power-recycled interferometric gravitational-wave antenna. *Appl. Opt.*, 40(28):4988–4998, Oct 2001. doi: 10.1364/AO.40.004988. URL <http://ao.osa.org/abstract.cfm?URI=ao-40-28-4988>. 26
- [37] C. C. Gerry and P. Knight. *Introductory quantum optics*. Cambridge University Press, 2005. 31, 32
- [38] G. I. González and P. R. Saulson. Brownian motion of a mass suspended by an anelastic wire. *The Journal of the Acoustical Society of America*, 96(1):207–212, 1994. doi: 10.1121/1.410467. URL <https://doi.org/10.1121/1.410467>. 38
- [39] D. J. Griffiths. *Introduction to quantum mechanics*. Pearson Prentice Hall, 2005. 31

- [40] G. M. Harry, A. M. Gretarsson, P. R. Saulson, S. E. Kittelberger, S. D. Penn, W. J. Startin, S. Rowan, M. M. Fejer, D. R. M. Crooks, G. Cagnoli, J. Hough, and N. Nakagawa. Thermal noise in interferometric gravitational wave detectors due to dielectric optical coatings. *Classical and Quantum Gravity*, 19(5):897, 2002. URL <http://stacks.iop.org/0264-9381/19/i=5/a=305>. 38
- [41] Y. Hefetz, N. Mavalvala, and D. Sigg. Principles of calculating alignment signals in complex resonant optical interferometers. *J. Opt. Soc. Am. B*, 14(7):1597–1606, Jul 1997. doi: 10.1364/JOSAB.14.001597. URL <http://josab.osa.org/abstract.cfm?URI=josab-14-7-1597>. 51
- [42] P. Hello and J.-Y. Vinet. Analytical models of thermal aberrations in massive mirrors heated by high power laser beams. *Journal de Physique*, 51(12):1267–1282, 1990. doi: 10.1051/jphys:0199000510120126700. 67
- [43] S. Hild, H. Grote, J. Degallaix, S. Chelkowski, K. Danzmann, A. Freise, M. Hewitson, J. Hough, H. Lück, M. Prijatelj, K. A. Strain, J. R. Smith, and B. Willke. Dc-readout of a signal-recycled gravitational wave detector. *Classical and Quantum Gravity*, 26(5):055012, 2009. URL <http://stacks.iop.org/0264-9381/26/i=5/a=055012>. 18
- [44] S. A. Hughes and K. S. Thorne. Seismic gravity-gradient noise in interferometric gravitational-wave detectors. *Phys. Rev. D*, 58:122002, Nov 1998. doi: 10.1103/PhysRevD.58.122002. URL <https://link.aps.org/doi/10.1103/PhysRevD.58.122002>. 38
- [45] I. K. and S. D. Frequency response of the aligo interferometer: part1. Technical report, California Institute of Technology, 2015. URL <https://dcc.ligo.org/LIGO-T1500325>. 30
- [46] I. K., S. D., and K. K. Frequency response of the aligo interferometer: part2. Technical report, California Institute of Technology, 2015. URL <https://dcc.ligo.org/LIGO-T1500461>. 30
- [47] I. K., S. D., and K. K. Frequency response of the aligo interferometer: part3. Technical report, California Institute of Technology, 2015. URL <https://dcc.ligo.org/LIGO-T1500559>. 30
- [48] H. J. Kimble, Y. Levin, A. B. Matsko, K. S. Thorne, and S. P. Vyatchanin. Conversion of conventional gravitational-wave interferometers into quantum nondemolition interferometers by modifying their input and/or output optics. *Phys. Rev. D*, 65:022002, Dec 2001. doi: 10.1103/PhysRevD.65.022002. URL <https://link.aps.org/doi/10.1103/PhysRevD.65.022002>. 31, 39, 40
- [49] H. Kogelnik and T. Li. Laser beams and resonators. *Appl. Opt.*, 5(10):1550–1567, Oct 1966. doi: 10.1364/AO.5.001550. URL <http://ao.osa.org/abstract.cfm?URI=ao-5-10-1550>. 84

- [50] R. Lawrence, M. Zucker, P. Fritschel, P. Marfuta, and D. Shoemaker. Adaptive thermal compensation of test masses in advanced ligo. *Classical and Quantum Gravity*, 19(7):1803, 2002. URL <http://stacks.iop.org/0264-9381/19/i=7/a=377>. 70
- [51] O. D. M Rakhmanov, F Bondu and R. L. S. Jr. Characterization of the ligo 4 km fabry–perot cavities via their high-frequency dynamic responses to length and laser frequency variations. *Classical and Quantum Gravity*, Feb 2004. URL <http://iopscience.iop.org/article/10.1088/0264-9381/21/5/015/meta>. 19
- [52] F. Maticichard, B. Lantz, K. Mason, R. Mittleman, B. Abbott, S. Abbott, E. Allwine, S. Barnum, J. Birch, S. Biscans, D. Clark, D. Coyne, D. DeBra, R. DeRosa, S. Foley, P. Fritschel, J. Giaime, C. Gray, G. Grabeel, J. Hanson, M. Hillard, J. Kissel, C. Kucharczyk, A. L. Roux, V. Lhuillier, M. Macinnis, B. O'Reilly, D. Ottaway, H. Paris, M. Puma, H. Radkins, C. Ramet, M. Robinson, L. Ruet, P. Sareen, D. Shoemaker, A. Stein, J. Thomas, M. Vargas, and J. Warner. Advanced ligo two-stage twelve-axis vibration isolation and positioning platform. part 1: Design and production overview. *Precision Engineering*, 40:273 – 286, 2015. ISSN 0141-6359. doi: <https://doi.org/10.1016/j.precisioneng.2014.09.010>. URL <http://www.sciencedirect.com/science/article/pii/S0141635914001561>. 35
- [53] F. Maticichard, B. Lantz, K. Mason, R. Mittleman, B. Abbott, S. Abbott, E. Allwine, S. Barnum, J. Birch, S. Biscans, D. Clark, D. Coyne, D. DeBra, R. DeRosa, S. Foley, P. Fritschel, J. Giaime, C. Gray, G. Grabeel, J. Hanson, M. Hillard, J. Kissel, C. Kucharczyk, A. L. Roux, V. Lhuillier, M. Macinnis, B. O'Reilly, D. Ottaway, H. Paris, M. Puma, H. Radkins, C. Ramet, M. Robinson, L. Ruet, P. Sareen, D. Shoemaker, A. Stein, J. Thomas, M. Vargas, and J. Warner. Advanced ligo two-stage twelve-axis vibration isolation and positioning platform. part 2: Experimental investigation and tests results. *Precision Engineering*, 40:287 – 297, 2015. ISSN 0141-6359. doi: <https://doi.org/10.1016/j.precisioneng.2014.11.010>. URL <http://www.sciencedirect.com/science/article/pii/S0141635914002098>. 35
- [54] F. Maticichard, B. Lantz, R. Mittleman, K. Mason, J. Kissel, B. Abbott, S. Biscans, J. McIver, R. Abbott, S. Abbott, E. Allwine, S. Barnum, J. Birch, C. Celerier, D. Clark, D. Coyne, D. DeBra, R. DeRosa, M. Evans, S. Foley, P. Fritschel, J. A. Giaime, C. Gray, G. Grabeel, J. Hanson, C. Hardham, M. Hillard, W. Hua, C. Kucharczyk, M. Landry, A. L. Roux, V. Lhuillier, D. Macleod, M. Macinnis, R. Mitchell, B. O'Reilly, D. Ottaway, H. Paris, A. Pele, M. Puma, H. Radkins, C. Ramet, M. Robinson, L. Ruet, P. Sarin, D. Shoemaker, A. Stein, J. Thomas, M. Vargas, K. Venkateswara, J. Warner, and S. Wen. Seismic isolation of advanced ligo: Review of strategy, instrumentation and performance. *Classical*

- and Quantum Gravity*, 32(18):185003, 2015. URL <http://stacks.iop.org/0264-9381/32/i=18/a=185003>. 35
- [55] E. Morrison, B. J. Meers, D. I. Robertson, and H. Ward. Automatic alignment of optical interferometers. *Appl. Opt.*, 33(22):5041–5049, Aug 1994. doi: 10.1364/AO.33.005041. URL <http://ao.osa.org/abstract.cfm?URI=ao-33-22-5041>. 48
- [56] G. Mueller, Q. ze Shu, R. Adhikari, D. B. Tanner, D. Reitze, D. Sigg, N. Mavalvala, and J. Camp. Determination and optimization of mode matching into optical cavities by heterodyne detection. *Opt. Lett.*, 25(4):266–268, Feb 2000. doi: 10.1364/OL.25.000266. URL <http://ol.osa.org/abstract.cfm?URI=ol-25-4-266>. 60
- [57] E. Oelker, T. Isogai, J. Miller, M. Tse, L. Barsotti, N. Mavalvala, and M. Evans. Audio-band frequency-dependent squeezing for gravitational-wave detectors. *Phys. Rev. Lett.*, 116:041102, Jan 2016. doi: 10.1103/PhysRevLett.116.041102. URL <https://link.aps.org/doi/10.1103/PhysRevLett.116.041102>. 40
- [58] U. of Birmingham. *Finesse Manual*, 2014. URL <http://www.gwoptics.org/finesse/>. 54
- [59] A. T. O’Neil and J. Courtial. Mode transformations in terms of the constituent hermite–gaussian or laguerre–gaussian modes and the variable-phase mode converter. *Optics Communications*, 181(1): 35 – 45, 2000. ISSN 0030-4018. doi: [https://doi.org/10.1016/S0030-4018\(00\)00736-7](https://doi.org/10.1016/S0030-4018(00)00736-7). URL <http://www.sciencedirect.com/science/article/pii/S0030401800007367>. 47, 59, 60
- [60] F. A. E. Pirani. Republication of: On the physical significance of the riemann tensor. *General Relativity and Gravitation*, 41(5):1215–1232, May 2009. ISSN 1572-9532. doi: 10.1007/s10714-009-0787-9. URL <https://doi.org/10.1007/s10714-009-0787-9>. 7
- [61] J. Ramette, M. Kasprzack, A. Brooks, C. Blair, H. Wang, and M. Heintze. Analytical model for ring heater thermal compensation in the advanced laser interferometer gravitational-wave observatory. *Appl. Opt.*, 55(10):2619–2625, Apr 2016. doi: 10.1364/AO.55.002619. URL <http://ao.osa.org/abstract.cfm?URI=ao-55-10-2619>. 72
- [62] B. E. A. Saleh and M. C. Teich. *Fundamentals of Photonics*. Wiley-Interscience, 2009. 43, 44
- [63] P. Saulson. *Fundamentals of Gravitational Wave Detectors*. World Scientific, 2016. 10, 19, 37, 38
- [64] P. R. Saulson. Terrestrial gravitational noise on a gravitational wave antenna. *Phys. Rev. D*, 30:732–736, Aug 1984. doi: 10.1103/PhysRevD.30.732. URL <https://link.aps.org/doi/10.1103/PhysRevD.30.732>. 38

- [65] P. R. Saulson. Thermal noise in mechanical experiments. *Phys. Rev. D*, 42:2437–2445, Oct 1990. doi: 10.1103/PhysRevD.42.2437. URL <https://link.aps.org/doi/10.1103/PhysRevD.42.2437>. 38
- [66] P. R. Saulson. If light waves are stretched by gravitational waves, how can we use light as a ruler to detect gravitational waves? *American Journal of Physics*, 65(6):501–505, 1997. doi: 10.1119/1.18578. URL <https://doi.org/10.1119/1.18578>. 7
- [67] B. F. Schutz. *A first course in general relativity*. Cambridge University Press, 2009. 6
- [68] R. Shankar. *Principles of Quantum Mechanics*. Springer Verlag, 2014. 30, 31
- [69] K. Strain, K. Danzmann, J. Mizuno, P. Nelson, A. Rüdiger, R. Schilling, and W. Winkler. Thermal lensing in recycling interferometric gravitational wave detectors. *Physics Letters A*, 194(1):124 – 132, 1994. ISSN 0375-9601. doi: [https://doi.org/10.1016/0375-9601\(94\)00717-4](https://doi.org/10.1016/0375-9601(94)00717-4). URL <http://www.sciencedirect.com/science/article/pii/0375960194007174>. 70
- [70] P. Veitch, A. Brooks, W. Kim, C. Blair, H. Cao, G. Grabeel, T. Hardwick, M. Heintze, A. Hepons-tall, C. Ingram, J. Munch, D. Ottaway, and T. Vo. Hartmann wavefront sensors for advanced ligo. In *Conference on Lasers and Electro-Optics*, page SW3M.5. Optical Society of America, 2018. doi: 10.1364/CLEO_SI.2018.SW3M.5. URL http://www.osapublishing.org/abstract.cfm?URI=CLEO_SI-2018-SW3M.5. 71
- [71] J.-Y. Vinet. On special optical modes and thermal issues in advanced gravitational wave interferometric detectors. *Living Reviews in Relativity*, 12(1):5, Jul 2009. ISSN 1433-8351. doi: 10.12942/lrr-2009-5. URL <https://doi.org/10.12942/lrr-2009-5>. 67, 70
- [72] H. Wang, C. Blair, M. D. Álvarez, A. Brooks, M. F. Kasprzack, J. Ramette, P. M. Meyers, S. Kaufer, B. O'Reilly, C. M. Mow-Lowry, and A. Freise. Thermal modelling of advanced ligo test masses. *Classical and Quantum Gravity*, 34(11):115001, 2017. URL <http://stacks.iop.org/0264-9381/34/i=11/a=115001>. 72
- [73] J. Weber. Evidence for discovery of gravitational radiation. *Phys. Rev. Lett.*, 22:1320–1324, Jun 1969. doi: 10.1103/PhysRevLett.22.1320. URL <https://link.aps.org/doi/10.1103/PhysRevLett.22.1320>. 8
- [74] J. M. Weisberg, J. H. Taylor, and L. A. Fowler. Gravitational waves from an orbiting pulsar. *Scientific American*, 245(4):74–83, 1981. ISSN 00368733, 19467087. URL <http://www.jstor.org/stable/24964580>. 5

- [75] W. Winkler, K. Danzmann, A. Rüdiger, and R. Schilling. Heating by optical absorption and the performance of interferometric gravitational-wave detectors. *Phys. Rev. A*, 44:7022–7036, Dec 1991. doi: 10.1103/PhysRevA.44.7022. URL <https://link.aps.org/doi/10.1103/PhysRevA.44.7022>. 64, 70
- [76] H. Yamamoto. Effect of itm thermal lens in beam reflection, Jan 2009. URL
- [77] H. Yu, D. Martynov, S. Vitale, M. Evans, D. Shoemaker, B. Barr, G. Hammond, S. Hild, J. Hough, S. Huttner, S. Rowan, B. Sorazu, L. Carbone, A. Freise, C. Mow-Lowry, K. L. Dooley, P. Fulda, H. Grote, and D. Sigg. Prospects for detecting gravitational waves at 5 hz with ground-based detectors. *Phys. Rev. Lett.*, 120:141102, Apr 2018. doi: 10.1103/PhysRevLett.120.141102. URL <https://link.aps.org/doi/10.1103/PhysRevLett.120.141102>. 35